THE EFFECT OF TUMOUR GEOMETRY ON THE QUANTIFICATION ACCURACY OF ^{99m}Tc AND ^{123}I IN PLANAR PHANTOM IMAGES

KEAMOGETSWE RAMONAHENG

THE EFFECT OF TUMOUR GEOMETRY ON THE QUANTIFICATION ACCURACY OF ^{99m}Tc AND ^{123}I IN PLANAR PHANTOM IMAGES.

by

Keamogetswe Ramonaheng

This dissertation is being submitted in fulfilment of the requirements for the M.Med.Sc Medical Physics qualification in the Faculty Health Sciences, at the University of the Free State.

August 2014

Promoter: Dr. J.A. van Staden

Co-promoter: Dr. H. du Raan

I certify that the dissertation hereby submitted by me for the M.Med.Sc Medical Physics qualification at the University of the Free State is my independent effort and had not previously been submitted for a qualification at another university/faculty. I furthermore waive copyright of the dissertation in favour of the University of the Free State.

Bloemfontein

August 2014

Keamogetswe Ramonaheng

THE EFFECT OF TUMOUR GEOMETRY ON THE QUANTIFICATION ACCURACY OF ^{99m}Tc AND ^{123}I IN PLANAR PHANTOM IMAGES.

INDEX

1. INTRODUCTION TO QUANTITATIVE NUCLEAR MEDICINE.

1.1 Quantitative nuclear medicine imaging.

Radionuclide imaging is based on detecting photons emitted from inside the body after administration of a radiopharmaceutical into the body. The radiopharmaceutical is distributed to specific organs in the body and emits photons. The photons emitted from the body are detected externally using a gamma camera and generate images which portray the in vivo distribution of the radiopharmaceutical. These images are used to detect a specific physiological function (disease or abnormality). Nuclear medicine is successful because it uses minute amounts of the radiopharmaceutical which does not have any effect on the process, or the organ function being studied.

Nuclear medicine images provide a measure of the uptake and retention of the radiopharmaceutical in the organs of interest. This measure is achieved because ideally the intensity observed within a particular region of interest (ROI) of the image should be proportional to the number of photons originating from the corresponding region in the imaged object or patient. However, this is not always the case due to inherent physical factors present in nuclear medicine imaging. These factors include; photon attenuation due to photoelectric absorption (further referred to as "attenuation") and Compton scatter (further referred to as "scatter"), partial volume effects (PVE) due to inadequate sampling and the gamma camera's limited spatial resolution, as well as the influence of background activity. These factors, as well as methods of compensation, are discussed in detail in Chapter 2.

These factors also contribute to the degradation of the nuclear medicine images and may induce artefacts and erroneous results regarding activity quantification and thus in-vivo function. Activity quantification of nuclear medicine images endeavour to provide an accurate measure of radioactivity uptake by attempting to correct for image degradation factors. Furthermore the accuracy of quantitative nuclear medicine is also dependant on factors such as; imaging geometry (source configuration), acquisition protocols, physical properties of the radionuclide used as well as the biokinetics of the pharmaceutical. Accurate activity quantification is important for its application in internal dose calculations for diagnostic or therapeutic purposes (Siegel et al., 1999). Conventionally, the known amount of injected radioactivity, measured using a dose calibrator, serves as a reference for determining the accuracy of the activity quantification.

Subsequent counts obtained from the gamma camera images can be related to radioactivity by means of the gamma camera sensitivity measurement. The gamma camera sensitivity is used to convert the obtained imaged counts to units of radioactivity. The reliability and precision of the accuracy achieved for activity quantification also depends on the integrity of the equipment used during the quantification process i.e. the stability of the counting and imaging equipment. Therefore performance measurements of the equipment used should also be considered.

1.2 Advantages of quantitative nuclear medicine images.

Radionuclide quantification has numerous applications. The most common of which is dose calculations for planning of therapeutic radionuclide doses or assessment of new radiopharmaceuticals. In most cases, whole body quantitative data is needed as it gives a complete picture of the body's response to the radiopharmaceutical. An example of this was shown in a study conducted by Sgouros et al., (2003) which investigated tumour dose response when using iodine-131(^{131}I)-labelled anti-B1 antibody in the treatment of non-Hodgkin's lymphoma. Similarly, the importance of pharmacokinetics when tailoring whole body doses using ^{131}I-labeled anti-B1 antibody has also been shown (Wahl et al., 1998). Whole body dosimetry is also very important for determining hematologic toxicity from radionuclide therapy and determining maximum tolerance levels in critical organs (O'Donoghue et al., 2002). It also allows for predictive diagnostic scans prior to therapeutic administrations, and assessment of bone marrow uptake which is an important factor to consider when administering radionuclide therapy doses. Whole body quantification allows for the assessment of radiopharmaceutical distribution change in the whole body over time. This is important information, particularly when assessing new radiopharmaceuticals in animal models for later use in patients. All the above mentioned radionuclide acquisitions emphasize the importance of whole body absorbed dose calculations as a measure of the body's response to radionuclide therapy. One of the prerequisites for accurate dose calculation is accurate activity quantification. Due to the above mentioned image degradation factors, accurate quantitative data in routine clinical application are not readily available from nuclear medicine images. Additional processing of the acquired planar and single photon emission computed tomography (SPECT) images is required to correct for these image degradation factors in an attempt to obtain accurate activity quantification data.

Some applications for quantitative images involve relative quantification whereby the physical effects of scatter and attenuation are assumed to cancel out. Relative quantification differs from absolute activity quantification as the former does not entail calibration of image counts into units of radioactivity. Relative quantification is based on the comparison of counts from a series of gamma camera images or different locations in the same image. Examples of relative quantification performed in nuclear medicine images includes; lung, renal, brain and cardiac perfusion studies. In so doing, conclusions may be made concerning the comparative function of the organs or different regions of the organ. Therefore calibration of image counts in terms of units of activity is not necessary. Another example of relative quantification is the determination of the fractional percentage uptake of an organ relative to the whole body radioactivity using the geometric mean (GM) method (also known as the conjugate view method). This can be achieved as the whole body radioactivity would represent 100 % of the injected activity at the time of injection (Zaidi and Koral, 2005). This method was reported to give reasonably accurate results in an indium-111 (^{111}In) platelet study of baboons (Van Reenen et al., 1982). In this study the baboons were sacrificed to validate the quantification accuracy of the method, using the total injected activity as reference. It was reported in a patient study using ^{131}I by Delpon et al., (2003) that whole body quantification using the GM with scatter and attenuation correction led to smaller errors in comparison to quantification done excluding these corrections. The authors also emphasized the importance of considering other factors such as organ superimposition and gamma camera collimator septal penetration.

Despite the application of relative quantification to provide information regarding in vivo function, the assumption that the contributions from scatter and attenuation in relative quantification cancel out, does not hold true. The impact of these factors is spatially varying and geometry (includes acquisition and imaging geometry) specific. Attempting to correct for these factors will decrease the geometric dependence, and the proportionality between the image counts and intensity can be maintained. This is advantageous when standard reference values for radionuclide uptake are used for diseases prognosis. In addition, quantitative images result in qualitative improvement (increased contrast) of both planar and SPECT images (King et al., 1992; Kojima et al., 1992). Therefore visual interpretation of the images is improved, increasing the physician's reporter confidence, and making delineation of organs of interest, for quantification purposes, easier (Khalil et al., 2004).

1.3 Planar versus SPECT quantification.

Planar images are acquired data from a particular view, angle or projection, and project the actual 3D activity distribution into a 2D data image without depth information. For this reason SPECT acquisitions were introduced and allow the representation of organ activity information in 3D by using reconstruction algorithms. Advantages of SPECT acquisitions include; determination of activity concentration and improved image contrast due to the elimination of overlying and underlying activity (superimposition of activity). However, planar acquisitions are advantageous over SPECT acquisitions because they require less time for acquisition and processing (an important consideration in healthcare) and allow for easy whole body quantification. Routine SPECT acquisitions are not convenient for whole body imaging due to impractical long acquisition and processing times. SPECT acquisitions would have to be performed over segments and added afterwards to obtain whole body images.

Numerous publications compared quantitative planar and SPECT imaging (Zaidi, (1996); Fleming et al., (2003); King and Farncombe, (2003); Zaidi and Koral (2005)). The limitations of quantitative imaging for both SPECT and planar imaging have been evaluated in a comprehensive phantom study by Pereira et al., (2010). In this study, quantification accuracy for planar and SPECT images was evaluated for various radionuclides (^{99m}Tc , ^{131}I and ^{111}In) in simple (homogenous cylindrical phantoms) and complex (torso phantom) geometries for inserts of varying sizes with different levels of activity concentration and background activity. It was reported that SPECT quantification produced consistent results in complex tumour geometries that involved high background activity levels, decreased object size (small volumes) and radioisotopes with more complex spectra such as ^{111}In. Inconsistent quantitative information obtained for planar studies was attributed to the superimposition of activity as well as methods used for background correction.

A method has been proposed to compensate for both superimposed and background activity in planar quantitative images (Sjögreen et al., 2005; Sjögreen et al., 2002). In both studies thicknesses that correspond to particular ROI were determined using attenuation maps either acquired with transmission sources or computed tomography (CT). Although there have been attempts to correct the problem of superimposed activity in planar images, it was solved by SPECT imaging.

1.4 Planar and SPECT quantification accuracies.

Different methods for correction of the previously mentioned degradation factors, for both planar and SPECT images, are available and have been reviewed in the literature (Erdi et al., 1996; King and Farncombe, 2003; Siegel et al., 1999; Zaidi and Koral, 2005). The accuracy achieved for quantification depends on the type of corrections applied (the principle upon which the corrections are based) and whether all factors affecting quantification have been corrected for, i.e. the degradation factors and problems that may be encountered due to complex tumour geometry.

The two most significant factors that influence activity quantification accuracy are attenuation and scatter. The GM method is the most commonly used method to correct for attenuation in planar studies. The GM concept was applied together with attenuation correction factors (ACF), acquired using transmission sources, in the phantom studies mentioned below to correct for attenuation. The use of the GM method, in conjunction with corrections for attenuation and background, has been reported to deliver accurate results in abdominal phantom studies using ^{99m}Tc, ^{123}I and ^{111}In for dosimetry purposes (Macey et al., 1999). In this study the dependence of quantification accuracy on imaging geometry (size of organ being quantified) was demonstrated and poorer accuracy was obtained for smaller organs such as the spleen, due to an inaccurate ACF. In a similar study, using an anthropomorphic phantom, activity quantification of heart, kidney and lung provided underestimations between 21 % and 26 % (Norrgren et al., 2003). The poor accuracy found in this study was attributed to the method used for background correction. It has been reported that planar quantification may be achieved with an accuracy of better than 10 % for simple geometries that do not involve organ overlap and background activity (King and Farncombe, 2003).

Scatter corrections such as the dual energy window (DEW) and triple energy window (TEW) scatter correction techniques, have been applied in many planar quantitative studies (King and Farncombe, 2003; Siegel et al., 1999). Application of GM with DEW and TEW scatter corrections has been conducted in patient studies using ^{131}I (Delpon et al., 2003). In this study activity underestimations of 40 % were reported for whole body quantitative data using both scatter correction methods.

Hybrid SPECT/CT systems were developed for the reliable transmission information obtained from the CT images to complement the emission data obtained from SPECT data. The use of these systems has gained much acceptance and proved useful in many clinical applications. CT images in nuclear medicine studies are used to provide anatomical localisation as well as an attenuation map to correct emission data for attenuation. The introduction of the hybrid systems in nuclear medicine has improved the overall sensitivity and specificity for diagnostic studies in nuclear medicine. From a literature survey by Ritt et al., (2011), it was shown that different accuracies have been reported for SPECT quantification depending on the type of corrections (scatter, attenuation and PVE) applied to the SPECT data. It was however concluded that in general SPECT quantification can be achieved with errors of less than 10 % in both phantom and clinical studies when appropriate corrections are implemented. A review article by Bailey and Willowson, (2013) confirmed that an accuracy of less than 10 % can be achieved in quantitative SPECT imaging with ^{99m}Tc, when CT-based corrections are implemented. The quantification accuracy was improved when SPECT data were used in conjunction with an iterative reconstruction algorithm that included resolution recovery, scatter correction, and CT-based attenuation correction (Zeintl et al., 2010). In a study conducted by Dewaraja et al., (2005) it was shown that more iterations were needed for the iterative reconstruction algorithm to improve the absorbed dose accuracy for small structures.

The low dose CT-scout view obtained with a SPECT/CT system was used by Minarik et al., (2005) to perform attenuation correction for whole body planar quantification. A quantification accuracy of ±4 % for the whole body of the Alderson RANDO phantom was obtained using this novel method along with the TEW scatter correction technique. Improved planar quantification accuracy has been achieved in ^{111}In phantom experiment and Monte Carlo simulation studies using 3D volume of interest definitions and maximum likelihood activity estimates (He and Frey, 2006). The authors reported planar accuracy to be comparable to that of SPECT, with less acquisition and computational time, when corrections for degradation factors were performed.

Various accuracies are reported for SPECT and planar quantitative images. It is important to note that the accuracy achieved during activity quantification is affected by many variables and the methods used to correct them. These include methods used to correct for the following factors: scatter, attenuation, PVE, stability of the gamma camera, septal penetration

and accuracy of the reference standard used for measurement, all discussed further in Chapter 2. The accuracy is also affected by complex imaging geometries. From the above reports SPECT quantification gives more accurate and stable results particularly for complex geometries in comparison to planar quantification. According to the literature there are numerous studies which attempt to correct for image degradation effects especially those of attenuation and scatter. Image quantification has various applications and the attempt to obtain accurate quantitative data is important for the clinical environment. Therefore the quantification process should not only serve to improve quantification accuracy, but should also be practical to implement in routine clinical application. From the above literature reports, it seems imperative for each clinic to evaluate the clinical available software, implement it correctly, and to validate its quantification accuracy.

1.5 Clinical motivation.

Examples of relative planar quantification studies performed in the Department of Nuclear Medicine at Universitas hospital include studies using ^{99m}Tc to investigate the following: renal uptake, lung quantification, skeletal studies for sacroiliac joints and thyroid uptake. Relative quantification is also performed with iodine-123-meta-iodobenzylguanidine ([^{123}I]-MIBG) images for investigations of neuroendocrine tumours such as pheochromocytoma and neuroblastoma prior to therapeutic treatment using iodine-131-meta-iodobenzylguanidine ([^{131}I]-MIBG). The bio-distribution of activity in these studies is mostly in the abdominal region and physical degrading factors include scatter, attenuation, PVE background activity and close proximity of organs (or organ overlap). This study will focus on the geometry encountered with investigations of neuroendocrine tumours conducted with [^{123}I]-MIBG.

The [^{123}I]-MIBG diagnostic acquisition is used as a predictive measure prior to therapeutic treatment with [^{131}I]-MIBG. The main determining factors for administration of therapeutic dose are; uptake in the tumour, negative bone marrow uptake and that none of the critical organs tolerance dose levels will be exceeded. Bone marrow uptake also serves as an important measure to determine whether therapeutic dose will be administered or not. Whole body anterior and posterior planar images are obtained at different time intervals, as a measure of the bio-distribution, uptake and excretion over a 48 hour period. Relative quantification is obtained by drawing ROI over organs of interest which mainly include; liver, tumour, heart and kidneys, obtaining counts and applying the GM method. The fractional uptake for each organ of interest relative to whole body uptake is calculated

according to clinical protocols established in the department based on clinical guidelines and literature (Bombardieri et al., 2003; Fielding et al., 1991; Olivier et al., 2003). Time activity curves of the organs of interest are generated. The cumulated dose to each organ is then calculated using the Medical Internal Radiation Dose (MIRD) formalism in order to determine the dose level at which tolerance levels for the critical organs would be exceeded (Siegel et al., 1999)

Examples of the anterior view of whole body scans obtained using [^{123}I]-MIBG are shown in Figure 1-1. As can be seen from these images, the tumours (indicated by arrows) are mainly in the abdominal region. The geometry of the tumours varies between patients with regard to size, proximity to the liver and depth in the abdomen. Some of these tumours are embedded in the liver. Thus, increased counts (intensity) may be detected in the tumour due to surrounding scatter from the liver or inclusion of primary counts from the liver in tumour ROI definition, therefore giving a false indication of radioactivity uptake. Background activity, organ overlap (tumour with liver) and various tumour-background ratios should also be considered.

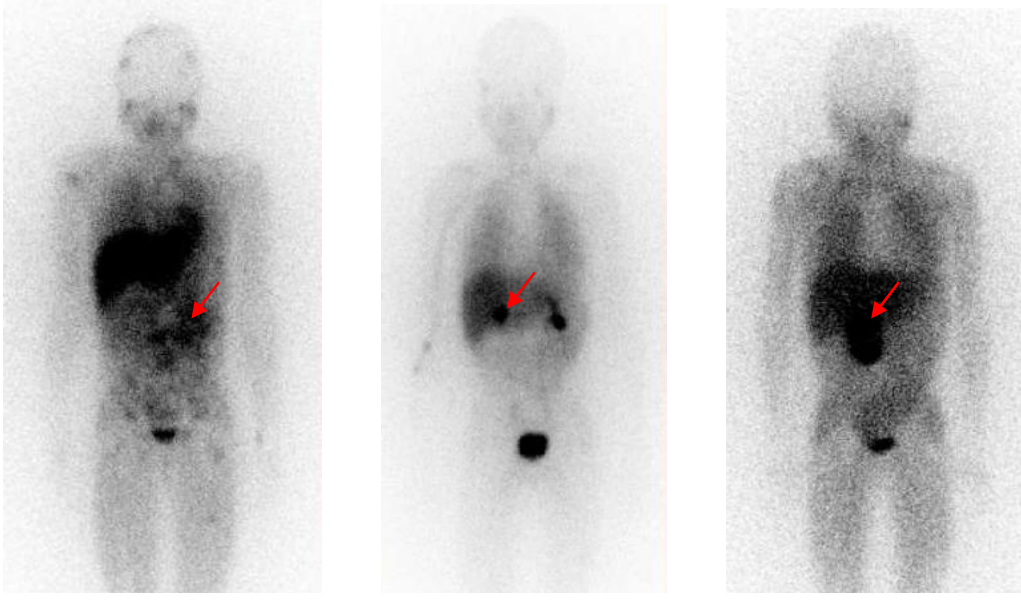

Figure 1-1: *Clinical examples of [^{123}I]-MIBG whole body anterior images for three patients, acquired on the Symbia T SPECT/CT (Siemens Medical Solutions USA, Inc.) in the Department of Nuclear Medicine at Universitas Hospital, for quantification of neuroendocrine tumours. These images illustrate the variability in tumour geometry (indicated by the arrows), with regard to size and distance from the liver.*

Due to the above described tumour geometry encountered in patients with neuroendocrine tumours, it was important that an attempt be made to correct for these degrading physical factors of attenuation and scatter for quantification purposes. The impact of imaging geometry such as tumour size and distance from the liver, on quantification accuracy should be evaluated. Although the relative quantification of [^{123}I]-MIBG described above is indicative of factors determining therapeutic administration and dose calculations, it does not take degradation factors into account. Studies mentioned above have shown the necessity of applying, amongst others, attenuation and scatter corrections in an attempt to obtain improved activity quantification accuracy for application in internal dose calculations. Therefore a technique for quantification of planar images was established.

The technique was first developed with the less expensive and more readily available ^{99m}Tc (Chapter 3) and later applied to the more costly ^{123}I (Chapter 4) with the necessary adjustments being made to account for the difference in physical properties between the two radionuclides. Clinical protocols as recommended by the Symbia T manufacturer (Syngo MI Applications 2007A; Siemens Healthcare) were used for the quantification process as the intent was not optimisation, but rather to reflect the accuracy that can be achieved with routine protocols. Scatter correction was performed using the modified and conventional TEW scatter correction techniques for ^{99m}Tc and ^{123}I respectively (discussed in Chapter 2, Section 2.3.2.1.2(e)). Attenuation correction was performed by means of ACFs measured using an uncollimated ^{99m}Tc printed transmission source. The quantified results were compared to the dose calibrator radioactivity measurements, and the quantification accuracy was established as the percentage difference between the two values.

The aim of this study was to evaluate the effect of tumour geometry on the quantification accuracy of ^{99m}Tc and ^{123}I in planar phantom images, by applying scatter and attenuation corrections, with the focus on neuroendocrine tumours.

Activity quantification was performed using an in-house manufactured abdominal phantom. The phantom was developed to simulate the tumour geometry encountered for patients with neuroendocrine tumours imaged using [^{123}I]-MIBG, as shown in Figure 1-1. The effect of the above mentioned corrections on activity quantification accuracy depends on the complexity of the imaging geometry.

The abdominal phantom geometry was designed to allow for assessment of the following variables:

1) Varying axial distance between the tumour and the liver
2) Varying tumour sizes as a function of axial distance from the liver
3) Influence of two tumour-background ratios

Quantification of activity distribution in planar images has received much attention in the past. This is due to the abovementioned advantages that quantitative information offer. The accuracy with which activity quantification is achieved depends on the corrections applied in the quantification process to compensate for the degradation factors inherent in nuclear medicine imaging. According to literature numerous methods are available for correction of these degradation factors. The principle that governs these correction factors is an important consideration for their implementations in routine clinical practice. Therefore a clear understanding of these correction methods is important in order to ensure their appropriate incorporation in a quantification technique. These corrections, together with their application and practicality, are discussed in detail in Chapter 2.

References

Bailey, D.L., Willowson, K.P., 2013. An evidence-based review of quantitative SPECT imaging and potential clinical applications. J. Nucl. Med. 54, 83–89.

Bombardieri, E., Aktolun, C., Baum, R.P., Bishof-Delaloye, A., Buscombe, J., Chatal, J.F., Maffioli, L., Moncayo, R., Mortelmans, L., Reske, S.N., 2003. ^{131}I/^{123}I-Metaiodobenzylguanidine (MIBG) scintigraphy: procedure guidelines for tumour imaging. Eur. J. Nucl. Med. Mol. Imaging 30, B132–B139.

Delpon, G., Ferrer, L., Lisbona, A., Bardiès, M., 2003. Impact of scatter and attenuation corrections for iodine-131 two-dimensional quantitative imaging in patients. Cancer Biother. Radiopharm. 18, 191–199.

Dewaraja, Y.K., Wilderman, S.J., Ljungberg, M., Koral, K.F., Zasadny, K., Kaminiski, M.S., 2005. Accurate dosimetry in ^{131}I radionuclide therapy using patient-specific, 3-dimensional methods for SPECT reconstruction and absorbed dose calculation. J. Nucl. Med. 46, 840–849.

Erdi, A.K., Erdi, Y.E., Yorke, E.D., Wessels, B.W., 1996. Treatment planning for radio-immunotherapy. Phys. Med. Biol. 41, 2009–2026.

Fielding, S.L., Flower, M.A., Ackery, D., Kemshead, J.T., Lashford, L.S., Lewis, I., 1991. Dosimetry of iodine 131 metaiodobenzylguanidine for treatment of resistant neuroblastoma: results of a UK study. Eur. J. Nucl. Med. 18, 308–316.

Fleming, J.S., Conway, J.H., Bolt, L., Holgate, S.T., 2003. A comparison of planar scintigraphy and SPECT measurement of total lung deposition of inhaled aerosol. J. Aerosol Med. 16, 9–19.

He, B., Frey, E.C., 2006. Comparison of conventional, model-based quantitative planar, and quantitative SPECT image processing methods for organ activity estimation using In-111 agents. Phys. Med. Biol. 51, 3967.

Khalil, M., Brown, E., Heller, E., 2004. Does scatter correction of cardiac spect improve image quality in the presence of high extracardiac activity? J. Nucl. Cardiol. 11, 424–432.

King, M., Farncombe, T., 2003. An overview of attenuation and scatter correction of planar and SPECT data for dosimetry studies. Cancer Biother. Radiopharm. 18, 181–190.

King, M.A., Hademenos, G.J., Glick, S.J., 1992. A dual-photopeak window method for scatter correction. J. Nucl. Med. 33, 605–612.

Kojima, A., Tsuji, A., Takaki, Y., Tomiguchi, S., Hara, M., Matsumoto, M., Takahashi, M., 1992. Correction of scattered photons in Tc-99m imaging by means of a photopeak dual-energy window acquisition. Ann. Nucl. Med. 6, 153–158.

Macey, D.J., DeNardo, G.L., DeNardo, S.J., 1999. Planar gamma camera quantitation of ^{123}I, ^{99m}Tc or ^{111}In in the liver and spleen of an abdominal phantom. Cancer Biother. Radiopharm. 14, 299–306.

Minarik, D., Sjögreen, K., Ljungberg, M., 2005. A new method to obtain transmission images for planar whole-body activity quantification. Cancer Biother. Radiopharm. 20, 72–76.

Norrgren, K., Svegborn, S.L., Areberg, J., Mattsson, S., 2003. Accuracy of the quantification of organ activity from planar gamma camera images. Cancer Biother. Radiopharm. 18, 125–131.

O'Donoghue, J.A., Baidoo, N., Deland, D., Welt, S., Divgi, C.R., Sgouros, G., 2002. Hematologic toxicity in radioimmunotherapy: dose-response relationships for I-131 labeled antibody therapy. Cancer Biother. Radiopharm. 17, 435–443.

Olivier, P., Colarinha, P., Fettich, J., Fischer, S., Frökier, J., Giammarile, F., Gordon, I., Hahn, K., Kabasakal, L., Mann, M., Mitjavila, M., Piepsz, A., Porn, U., Sixt, R., van

Velzen, J., 2003. Guidelines for radioiodinated MIBG scintigraphy in children. Eur. J. Nucl. Med. Mol. Imaging 30, B45–50.

Pereira, J.M., Stabin, M.G., Lima, F.R.A., Guimarães, M.I.C.C., Forrester, J.W., 2010. Image quantification for radiation dose calculations--limitations and uncertainties. Health Phys. 99, 688–701.

Ritt, P., Vija, H., Hornegger, J., Kuwert, T., 2011. Absolute quantification in SPECT. Eur. J. Nucl. Med. Mol. Imaging 38 Suppl. 1, S69–77.

Sgouros, G., Squeri, S., Ballangrud, A.M., Kolbert, K.S., Teitcher, J.B., Panageas, K.S., Finn, R.D., Divgi, C.R., Larson, S.M., Zelenetz, A.D., 2003. Patient-specific, 3-dimensional dosimetry in non-Hodgkin's lymphoma patients treated with ^{131}I-anti-B1 antibody: assessment of tumor dose-response. J. Nucl. Med. 44, 260–268.

Siegel, J.A., Thomas, S.R., Stubbs, J.B., Stabin, M.G., Hays, M.T., Koral, K.F., Robertson, J.S., Howell, R.W., Wessels, B.W., Fisher, D.R., Weber, D.A., Brill, A.B., 1999. MIRD pamphlet no. 16: Techniques for quantitative radiopharmaceutical biodistribution data acquisition and analysis for use in human radiation dose estimates. J. Nucl. Med. 40, 37S–61S.

Sjögreen, K., Ljungberg, M., Strand, S.E., 2002. An activity quantification method based on registration of CT and whole-body scintillation camera images, with application to ^{131}I. J. Nucl. Med. 43, 972–982.

Sjögreen, K., Ljungberg, M., Wingårdh, K., Minarik, D., Strand, S.E., 2005. The LundADose method for planar image activity quantification and absorbed-dose assessment in radionuclide therapy. Cancer Biother. Radiopharm. 20, 92–97.

Van Reenen, O., Lötter, M.G., Heyns, A.D., de Kock, F., Herbst, C., Kotzé, H., Pieters, H., Minnaar, P.C., Badenhorst, P.N., 1982. Quantification of the distribution of ^{111}In-labelled platelets in organs. Eur. J. Nucl. Med. 7, 80–84.

Wahl, R.L., Kroll, S., Zasadny, K.R., 1998. Patient-specific whole-body dosimetry: principles and a simplified method for clinical implementation. J. Nucl. Med. 39, 14S–20S.

Zaidi, H., 1996. Comparative methods for quantifying thyroid volume using planar imaging and SPECT. J. Nucl. Med. 37, 1421–1426.

Zaidi, H., Koral, KF., 2005. SCATTER CORRECTION STRATEGIES IN EMISSION TOMOGRAPHY. In: "*Quantitative analysis in nuclear medicine imaging"*. New York: Kluwer Academic/Plenum Publishers, USA 414–431.

Zeintl, J., Vija, A.H., Yahil, A., Hornegger, J., Kuwert, T., 2010. Quantitative accuracy of clinical ^{99m}Tc SPECT/CT using ordered-subset expectation maximization with 3-dimensional resolution recovery, attenuation, and scatter correction. J. Nucl. Med. 51, 921–928.

2. FACTORS AFFECTING ACTIVITY QUANTIFICATION IN PLANAR IMAGES.

2.1 Introduction.

As mentioned in Chapter 1 (Section 1.1), there are inherent limitations encountered in nuclear medicine imaging which affect radionuclide activity quantification. These include the physical aspects of imaging such as: scatter and attenuation of photons, as well as partial volume effects (PVE) due to inadequate sampling and the gamma camera's limited spatial resolution. These image degradation effects, and thus their corrections, are further complicated by the imaging geometry which includes: superimposition of structures (organ overlap), the presence of background activity and region of interest (ROI) definition to delineate the organ of interest from adjacent structures (Sjögreen et al., 2005). In an attempt to obtain reliable quantitative results these factors (including their impact on quantification accuracy) and their proposed methods of compensation will be discussed in the subsequent sections.

The performance of the correction techniques, and their precision, is dependent upon the gamma camera stability with regard to performance characteristics such as, flood field uniformity, sensitivity and septal penetration, as well as spatial resolution. The integrity of the dose calibrator with regard to accuracy and reproducibility should also be of consideration as activity quantification is made with reference to measurements in the dose calibrator. Accuracy and precision of the equipment involved in the quantification process should be considered and will be discussed briefly.

2.2 Equipment stability.

Nuclear medicine produces clinical quantitative information from radionuclide uptake with the use of imaging (gamma cameras) and counting (well counter, thyroid uptake probe and dose calibrators) devices. Variations in the response of these devices (instability and drift), must be considered, as these changes will affect the consistency and accuracy of the quantitative results. The quality control (QC) of this equipment is important to ensure reliable quantitative results. A QC programme ensures that the equipment performs within acceptable ranges set by international guidelines and manufacturer specifications. Therefore, a measure of the performance characteristics for the gamma camera and dose calibrator used in the image quantification process should be established and adhered to prior to acquisition of quantitative data. In so doing, any deviations in the precision or accuracy of the quantification results, due to equipment instability, can be noted.

2.2.1 Dose calibrator accuracy and reproducibility.

The dose calibrator plays an important role in image activity quantification accuracy. Image activity quantification is done with reference to activity measured in a dose calibrator. Therefore the accuracy of the dose calibrator should be a consideration in the quantification process. The accuracy of the dose calibrator is determined using a calibrated source with traceability to a National Standards Laboratory. Protocols for QC tests and their limits of acceptability are described in detail in the International Atomic Energy Agency (IAEA) document; IAEA Quality Assurance for Radioactivity Measurement in Nuclear Medicine (IAEA, 2006). The limits of acceptability for the tests relevant for this research project i.e. accuracy and reproducibility tests, are 10 % and 5 % respectively. These limits set the percentage differences acceptable, between the delivered and the prescribed dose, for diagnostic and therapeutic purposes. However the effect of these errors, accepted for dose calibrators, will propagate in accordance with Equation 2.1 to the quantification values, thus resulting ultimately in larger errors (Cherry et al., 2003a).

$$\sigma\left(M_1 \pm M_2 \pm M_3 \pm ...\right) = \sqrt{\sigma\left(M_1\right)^2 + \sigma\left(M_2\right)^2 + \sigma\left(M_3\right)^2} \qquad \textbf{2. 1}$$

where: $\sigma(M_1)^2$, $\sigma(M_2)^2$ $\sigma(M_3)^2$... represents the variances of the individual measurements M_1, M_2, M_3… that constitute the quantification process.

Therefore, in order to obtain acceptable quantitative results all errors should be kept as minimum as possible. It should be considered that quantification accuracies of less than 10 % have been reported for planar quantification of images (King and Farncombe, 2003; Macey et al., 1999). Therefore accuracies of 10 % for the dose calibrator will have a larger effect on the final quantification accuracy achieved, due to error propagation. However, the accuracy of the dose calibrator may be incorporated into the quantification process with the use of the gamma camera's sensitivity (discussed in Section 2.7). In so doing, the inaccuracy of the dose calibrator will have minimal influence on the accuracy with which image activity quantification can be achieved, as long as it is stable for the duration of the measurements. However, it is an important factor to take into account when performing patient radioactivity administrations, as the prescribed doses are ascertained by measurements on the dose calibrator.

Comparison of accuracies for radioactivity measurements carried out using dose calibrators, has been carried out in several countries (Kim et al., 2005; Kossert and Thieme, 2007; Oropesa et al., 2005). From the discrepancies found in some of the results, these studies showed the importance of such measurements, as well as comparisons to National Standards Laboratories with traceability. Attempts were made to understand the reasons for the discrepancies and follow up actions were implemented (Kim et al., 2005). Discrepancies found in these studies included: insufficient training of technologists with regard to precision calculations for repeated measurements, wrong choices of switch selectors for the specific radionuclide in question and failure to provide sufficient time for the dose calibrator to stabilize after it had been switched on. Differences between the activity measurements of the various manufactures were attributed to the following: different materials that were used during radionuclide calibration, extra shielding, as well as the different primary standards used by the various manufacturers. Recommendations included: proper training of staff and frequent liaison with a medical physicist, recalibration of dose calibrators and most importantly frequent stability checks using a long lived source. These projects demonstrate reasonable attempts to improve quality and reliability of the dose calibrators. For the purpose of radionuclide administrations, correction factors may be determined to account for the inaccuracies found with the dose calibrator when the error is a consistent bias.

An important test to consider when doing quantification is the day to day reproducibility of the dose calibrator measurements. It is suggested by the IAEA Quality Assurance for Radioactivity Measurement in Nuclear Medicine that this daily QC be carried out using a long lived sealed medium energy radionuclide such as cesium-137. This test ensures long term stability of the accuracy of the radioactivity measurements performed using the dose calibrator.

2.2.2 Gamma camera quality control.

Owing to non-uniformities of the Thallium doped Sodium Iodide NaI(Tl) crystal and statistical variation in the photomultiplier tubes (PMTs) output, there is a variation in the pulse height recorded for different positions on the detector system of the gamma camera (Saha, 2012). For this reason the energy spectrum varies with spatial location on the detector system. The methods applied to correct for the image degradation factors, such as scatter and attenuation, are sensitive to the non-uniform response of the detector system due to the change of the energy spectrum with location. It was demonstrated in a scatter correction

review article by Buvat et al., (1994) that Compton scatter (discussed in Section 2.3.2) varied spatially and was a function of imaging geometry (this includes collimator object distance and the object geometry). In this regard, the effectiveness of the corrections applied for quantification, will be affected by non-uniformities obtained in the components of the gamma camera. It is therefore necessary to test the stability of the non-uniform response of the detector system.

Prior to imaging with the gamma camera it is important to ensure that the correct photopeak energy window settings are used for the particular radionuclide. Peaking of the spectrum is important as it ensures that the photopeak is centred within the respective pulse height analyzer (PHA) window set for the radionuclide used. This is important, as it will influence the amount of scatter contribution recorded in the PHA, which will affect characteristics of the gamma camera such as, uniformity and sensitivity. Scatter and sensitivity influence quantification and for this reason peaking of the gamma camera is essential. It is recommended that the photopeak energy window settings should be checked on a daily basis and with any radionuclide change (Zanzonico, 2008). Incorrect energy window settings may result in image artefacts, as either hot or cold regions on uniformity tests, depending on which side of the PHA the photopeak is misplaced, as was demonstrated in the IAEA Quality Assurance Atlas for Scintillation Camera Systems (IAEA, 2003). Off-peak effects will present in clinical images as similar patterns of abnormalities in a series of independent images. This effect was shown in a study by Shih et al., (2003) where the same abnormal myocardial perfusion defect was observed in two consecutive patients. The off-peak effects were then confirmed from a planar whole body image with degraded image quality. Degraded image quality reduces visual interpretation of images, making it difficult to delineate ROIs for quantification purposes.

(a) Intrinsic flood field uniformity.

One of the most commonly performed tests on the gamma camera is the intrinsic flood field uniformity test. This test is important as it ensures the stability of the gamma camera's response to a uniform flux of photons. This may vary due to PMT drifts and slight variations in the high voltage. There are several factors that can degrade the intrinsic uniformity of the gamma camera, therefore the uniformity check serves as a good indication of proper functioning of the gamma camera. This test will serve as an indication for the deviations that may be encountered in measurements of quantitative data. Therefore a strict QC programme,

following the National Manufacturer Electrical Association (NEMA), should be followed (NEMA, 2007). Routine QC should include an intrinsic uniformity test (Zanzonico, 2008).

(b) System resolution.

The system resolution is determined by the intrinsic resolution and the collimator resolution, where the latter is the main determining factor. Collimator resolution is expected to remain constant, unless the collimator was damaged. Therefore, intrinsic resolution is the variable factor for system resolution. This owes from the fact that intrinsic resolution is susceptible to statistical variations with regard to photon interaction position in the crystal as well as crystal deterioration. System resolution has a direct effect on PVE (discussed in Section 2.5) and as a result, ROI definition for organ delineation.

(c) Intrinsic count rate performance test.

For quantification purposes, it is also important to evaluate the intrinsic count rate performance, which is a measure of the gamma camera's response to increased (high) count rates. This is mainly a concern when large amounts of radioactivity are used, such as in first pass cardiac studies (Murphy, 1987) and post radionuclide therapy imaging (Eary et al., 1994) for dose calculations. The main concern is count losses that may be experienced at high count rates, which can lead to inaccuracies in the observed count rate and thus erroneous quantitative data. Therefore, the gamma camera's intrinsic count rate performance according to the NEMA recommendations should be measured. In an attempt to obtain accurate quantification results, it is recommended that significant count losses due to high count rates be taken into consideration and corrected for.

(d) Gamma camera sensitivity.

The gamma camera sensitivity is defined as the number of counts per unit time detected for each unit of activity present in a radioactive source, and is normally expressed in counts per second per Becquerel (cps/Bq) (NEMA, 2007). Sensitivity of the gamma camera depends on the geometric efficiency of the collimator, the intrinsic photopeak efficiency of the detector, PHA discriminator settings, and the dead time of the system. Of these four factors, collimator efficiency affects the sensitivity of the gamma camera the most. Although sensitivity does not form part of the routine gamma camera quality assurance it forms an integral part of the image quantification process and is thus discussed in Section 2.7.

2.3 Gamma ray interaction with matter.

Attenuation refers to the reduction in the intensity of the detected radiation, due to interaction between the γ-ray and the medium through which it travels (Cherry et al., 2003b). The interaction that takes place can either be due to the photoelectric effect, Compton scatter or pair production. Compton scatter predominates in the energy range of 26 keV to 30 MeV while the photoelectric effect is dominant below 26 keV (Bushberg et al., 2011). Pair production occurs for γ-rays with energies above 1.02 MeV, whereby the end result of interaction mechanism is the simultaneous emission of two photons of energy 511 keV in the opposite direction. However the focus of this study will be on acquisitions of radionuclides emitting single photons, in the energy range up to 364 keV. The intensity reduction of the detected γ-rays, in this energy range, is due to Compton scatter and the photoelectric effect. The reduction in intensity of γ-rays passing through an object, as detected by the gamma camera, is described by Equation 2.2. This equation accounts for attenuation of a narrow beam geometry (discussed below) for a mono-energetic beam.

$$I(x) = I(0)e^{-\mu x} \qquad \textbf{2. 2}$$

where: *I(x)* is intensity of the γ-rays transmitted through the object (attenuated γ-rays), *I(0)* is the intensity recorded with no object present (unattenuated γ-rays), μ is the linear attenuation coefficient (cm^{-1}) and x is the thickness of the object (cm). The linear attenuation coefficient is a measure of the probability that γ-rays of certain energy will undergo attenuation, for every unit distance travelled in a specific medium. Equation 2.2 describes the relationship between attenuated and unattenuated γ-rays, as a single exponential curve which depends on the linear attenuation coefficient and thickness of the object. These parameters in turn are a function of object composition and γ-ray energy. Increased density and thickness of the object result in a decreased transmission probability of the γ-rays. The magnitude with which the intensity of the imaged γ-rays is decreased is higher for lower energies.

As mentioned in Chapter 1, there should ideally be a linear relationship between the intensity observed within a particular ROI in an image and the amount of γ-rays (proportional to radionuclide activity) emitted from the corresponding region in the object. For this reason, γ-rays that travel perpendicular to the detector plane and pass parallel through the collimator holes depositing their energy through the photoelectric effect are desired. In so doing, correspondence of spatial information (emission position) of the interaction occurrence in the

object and increased intensity on the image, will be maintained. These γ-rays retain correct spatial information, and thus do not result in distorted image information due to scattered γ-rays. The linear relationship described above, results in meaningful qualitative and quantitative images for both single photon computed tomography (SPECT) and planar images. However, due to degradation factors of attenuation and scatter, which are an integral part of nuclear medicine imaging, the relationship is not attainable. For this reason additional processing (applying scatter and attenuation corrections) of images is performed in order to compensate for these degradation factors. This processing may include simultaneous image acquisitions in multiple energy windows for scatter correction purposes, and the addition of a computed tomography (CT) examination or transmission scan for attenuation correction. A technique that has recently become commonly performed in myocardial perfusion images (Dvorak et al., 2011).

SPECT myocardial perfusion studies have become one of the most popular examinations performed in nuclear medicine, and so has the effect of attenuation correction in these studies. It has been hypothesized that attenuation corrected myocardial perfusion images may alter patient diagnosis and thus management (Bateman and Cullom, 2005). Attenuation correction has been reported to reduce false positive diagnosis of defects in the myocardium for studies using Thallium-201 (^{201}Tl) (Velidaki et al., 2007). Nowadays myocardial perfusion imaging using technetium-99m-sestamibi ([^{99m}Tc]-MIBI) has gained popularity compared to imaging using ^{201}Tl, which was predominantly used in the past. In [^{99m}Tc]-MIBI studies, attenuation correction has been reported to improve image quality and aid in the interpretation of images regarding normal and abnormal perfusion (Heller et al., 2004; Roelants et al., 2006). Attenuation correction has been shown to increase the sensitivity and specificity for detection of coronary artery disease, thereby improving the diagnostic accuracy of myocardial perfusion studies (Dvorak et al., 2011).

An example of a [^{99m}Tc]-MIBI myocardial perfusion SPECT exercise study, acquired with the Symbia T SPECT/CT gamma camera (Siemens Medical Solutions USA, Inc.) in the Department of Nuclear Medicine at Universitas Hospital, is shown in Figure 2-1. The reconstructed short axis slices from the SPECT data obtained without attenuation and scatter correction demonstrated a perfusion defect in the antero-septal wall of the myocardium (indicated by the red arrow in Figure 2-1 (b)). After applying scatter and attenuation corrections, using the dual energy window (DEW) scatter correction technique and a CT-

derived patient-specific attenuation map respectively, the myocardium showed normal perfusion (indicated by the green arrow in Figure 2-1 (a)). This indicated that the initial decreased intensity was due to an attenuation defect.

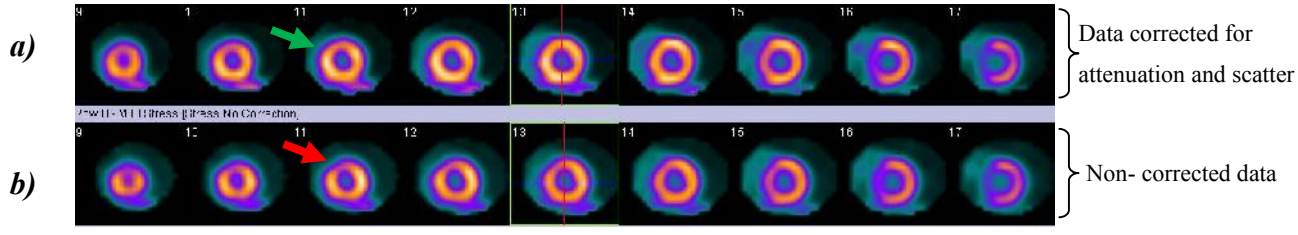

Figure 2-1: *Reconstructed stress myocardial perfusion images of a male patient who underwent exercise imaging. (a) Attenuation and scatter corrected images demonstrating a homogeneous distribution of the radiopharmaceutical throughout the myocardium. (b) Uncorrected images demonstrating a moderately decreased tracer distribution in the antero-septal wall.*

In a study conducted by Lee et al., (2001), investigating the effects of scatter and attenuation corrections in planar lung studies, the necessity of attenuation corrections in quantification of aerosol depositions was explicitly stated. Different attenuation methods investigated all indicated that uncorrected attenuation resulted in quantification errors, even in relative quantification. Attenuation correction using Chang's algorithm was reported to improve image quality (sharpness) and thus reader confidence in lung perfusion/ventilation SPECT studies when a mean linear attenuation coefficient of 0.09 cm^{-1} was used (Izadyar et al., 2011). This study indicated the advantage of the Chang algorithm for attenuation correction, which is readily available on most SPECT systems, as an alternative to CT attenuation correction. Although there was qualitative improvement of the lung perfusion/ventilation SPECT studies, the information might not be quantitatively correct.

It is evident from the above published research that scatter and attenuation correction results improved planar and SPECT quantification. In an attempt to achieve improved quantitative and qualitative images, post processing and modification to acquisition protocols may have to be made. Therefore an understanding of the effects of attenuation and scatter and their attempted corrections is important.

2.3.1 Attenuation due to photoeletric absorption.

Attenuation in this context refers to absorption due to the photoelectric process between γ-rays and the medium through which they travel. The effects of attenuation are more severe for structures (organs) of interest positioned deeper within an object (patient). Therefore, the image intensity will be higher for superficial organs in comparison to deeper lying organs with the same radionuclide concentration. The intensity, as seen from opposed views, may vary depending on the position of the organ being studied. It can result in an increased intensity from one view and a decreased intensity from the opposite view. There can also be variation in spatial resolution, as seen from opposed views, due to differences in detector source distance. In order to reduce this effect, the geometric mean (GM) method, also commonly known as conjugate counting, was introduced and is shown in Equation 2.3 (Cherry et al., 2003c; Thomas et al., 1976).

$$GM = \sqrt{I_A \times I_P} \qquad \textbf{2. 3}$$

where: I_A and I_P are the attenuated γ-rays from anterior and posterior views respectively. The GM is commonly used in nuclear medicine for quantification purposes particularly in planar images to reduce the attenuation effects (Zaidi and Koral, 2005). However, the GM is not without shortcomings. The limitations of the GM include: the fact that attenuation effects are reduced but are not eliminated, the GM assumes a uniform attenuation of γ-rays and has disregarded scatter contribution. The principle of the GM assumes that a single point source of activity is considered (Tothill, 1974), and organ overlap is not taken into consideration. Attempts to correct for these shortcomings are discussed below. The GM, for quantification purposes, is based on the γ-ray attenuation function shown in Equation 2.4, as seen from two opposed views, and illustrated in Figure 2-2.

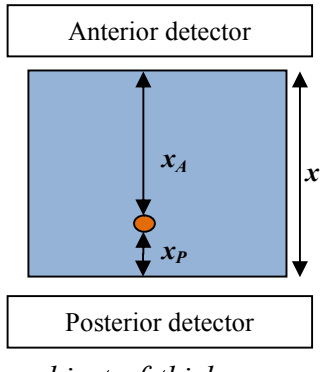

Figure 2-2: *Point source within an object of thickness x, as viewed by opposing detectors where attenuation correction may be compensated using the geometric mean.*

$$\sqrt{I_A(x)\times I_P(x)} = \sqrt{I_A(0)e^{-\mu x_A}\times I_P(0)e^{-\mu x_P}} = \sqrt{I(0)^2 e^{-\mu(x_A+x_P)}} = I(0)e^{-\mu x/2} \qquad \textbf{2. 4}$$

where: $I_A(0)$ and $I_P(0)$ are the unattenuated γ-rays from anterior and posterior views respectively, x_A and x_P are the source depths from anterior and posterior views respectively, and x is the patient or object thickness. In the practical application, $I_A(x)$ and $I_P(x)$ are the counts obtained in ROI defining the object of interest in the anterior and posterior views respectively. It can be seen from Equation 2.4, that the GM is a function of the unattenuated counts, object thickness and the linear attenuation coefficient. The advantage of using this method is that the GM of any 180° opposed datasets results in a quantification value that is independent of the source depth (Zaidi and Koral, 2005).

The GM concept (Equation 2.4) has been extensively used in the literature to obtain planar quantitative information and has resulted in reasonable accuracies. Several studies which have applied this concept, for quantification purposes, are reported. Accuracies of better than 10 % were achieved for indium-111 (^{111}I) and iodine-131 (^{131}I) phantom studies, while rabbit studies using technetium-99m-macroaggregated albumin and ^{99m}Tc sulphur colloid resulted in accuracies of 3.3 % and 3.7 % in the lungs and liver of the rabbits respectively (Graham and Neil, 1974). Several studies have successfully applied the GM in ^{131}I activity quantification of tumours and livers for the following studies; phantoms (Hammond et al., 1984), dogs (Eary et al., 1989) and patients (Leichner et al., 1981).

Attempts to improve the accuracy of planar activity quantification to date, still include the use of the GM principle. These attempts include: the use of 3D volumes of interest and iterative reconstruction (using the Maximum-likelihood Expectation-maximization Algorithm) to improve planar activity quantification accuracy (He and Frey, 2006). Minarik et al., (2005) used the transmission data from CT-scout images obtained from SPECT/CT systems to try and improve planar whole body quantification. In an anthropomorphic phantom study, CT data was used for ROI definition for organs of interest, as well as background activity and organ overlap compensation, resulting in improved ^{131}I planar activity quantification (Sjögreen et al., 2002). This work was also extended to improve activity quantification accuracy for yttrium-90 bremsstrahlung imaging (Minarik et al., 2009). The study consisted of an experimental investigation using a radiology support devices (RSD) torso phantom and Monte Carlo simulation studies of an anthropomorphic phantom.

As mentioned above, the GM does not fully account for the effects of attenuation (including scatter), the residual effects are presented in the exponential function shown in Equation 2.4. Therefore successful implementation of this method for quantification should take this factor into account.

2.3.1.1 Attenuation correction using transmission data.

Tissue attenuation information can be more accurately determined from transmission data rather than assuming a uniform linear attenuation coefficient. This may be achieved with the use of an external radionuclide source by acquiring transmission and blank images measured with and without the object in the field of view respectively. For quantification purposes, the ratio of the blank and transmission image counts is calculated to determine an object specific attenuation correction factor (ACF) (Equation 2.5). The counts are obtained from a ROI defining the emission source position.

$$ACF = \sqrt{\frac{I(0)}{I(x)}} = e^{\mu x/2} \qquad \textbf{2. 5}$$

where: *I(0)* and *I(x)* represents the counts in the blank and transmission images respectively. The ACF is a measure of the exponential function shown in Equation 2.4, from the principle given in Equation 2.2. External radionuclide sources used may be collimated or uncollimated, moving (used for whole body quantification) or stationery sources (King and Farncombe, 2003). The energies of the emission and transmission images may be the same or differ from one another, where the latter allows for simultaneous acquisitions in separate energy windows. In so doing, the registration problem is eliminated and the exact attenuation for a particular object thickness can be obtained. Simultaneous emission-transmission acquisitions using a lower energy transmission radionuclide (gadolinium-153) and a higher energy emission radionuclide (^{99m}Tc), yielded activity quantification accuracy of 5 % in SPECT phantom studies (Bailey et al., 1987). The valuable use of a dual head gamma camera was shown for simultaneous emission and transmission imaging using ^{99m}Tc and a cerium-139 line source respectively (Du Raan et al., 2000). This study demonstrated that accurate attenuation coefficients maps may be obtained for SPECT studies. Some gamma camera systems make use of high count rate radionuclides, for attenuation correction purposes. These may induce dead time for blank scan images which should be corrected for in attempt to obtain accurate quantitative information.

When the emission and transmission energies are equivalent, transmission images may be acquired before or after patient injection. Acquisition of transmission data prior to injection has the advantage that down-scatter, between the emission and transmission energies, is eliminated. However, the long time intervals between the emission and transmission scans may lead to patient movement and thus misregistration of images. This will result in erroneous attenuation correction. The use of fiducial markers may overcome this problem to a certain extent (Hutton et al., 2002). Transmission data acquisitions after patient injection results in controlled patient movement. This is owing to shorter time intervals between scans, and thus less probability of misregistration. Contamination of transmission data with emission data may however be present. Registration, of emission and transmission images (this includes hybrid imaging), is important as it affects the accuracy with which attenuation correction can be achieved. Several automated methods have been proposed to improve image registration (Maes et al., 1997; Studholme et al., 1996; Wells et al., 1996). It has been reported to improve diagnostic quality of nuclear medicine images (Hutton et al., 2002). However it is a separate research topic and not discussed herein.

Radionuclides used for emission and transmission images preferably have different energy emissions to avoid cross-talk between transmission and emission data. Several studies have used a cobalt-57 (^{57}Co) standard flood source, for practical reasons, to measure blank and transmission data for planar image quantification (Minarik et al., 2005; Norrgren et al., 2003; Sjögreen et al., 2005). An energy scaling factor must be applied to the ACF to account for the energy difference between the transmission and emission radionuclides, as shown in Equation 2.6 (Minarik et al., 2005)

$$ACF = \sqrt{\frac{I(0)}{I(x)}} \times \frac{\mu_{EM}}{\mu_{TR}} \qquad \textbf{2. 6}$$

where: μ_{EM} and μ_{TR} are the effective linear attenuation coefficients for the emission and transmission radionuclide energies respectively. In most instances of planar quantification, the emission data is explicitly corrected for scatter prior to the GM calculation. This implies that the ACF used for attenuation correction should be for narrow beam geometry. This concept is similar to the instance where narrow beam linear attenuation coefficients are used for attenuation correction of scatter corrected SPECT data (Bailey, 1998). Attenuation correction using narrow beam data may be achieved through scatter correction of the transmission data. This was carried out in a study conducted by Kojima et al., (2004) where

a ^{99m}Tc uncollimated line array source was used for attenuation correction. It was found in this study that the triple energy window (TEW) scatter correction technique estimated true scatter counts in the transmission source when optimized using a scatter factor of 1.0, as opposed to the conventional 0.5 (Discussed in Section 2.3.2.1.2(e)). This resulted in an accurate linear attenuation coefficient of 0.153cm^{-1} (close to ideal 0.154 cm^{-1}) for water, as opposed to the 0.127 cm^{-1} obtained with a scatter factor of 0.5. Alternatively a scaling factor may also be introduced to rescale the ACF data to narrow beam measurements. This can be obtained by measuring system linear attenuation coefficients for narrow beam and broad beam conditions and rescaling the ACF data to narrow beam geometry (following the above mentioned energy difference scaling factor), as shown in Equation 2.7.

$$ACF = \sqrt{\frac{I(0)}{I(x)}} \times \frac{\mu_{EM}}{\mu_{TR}} \times \frac{\mu_{NB}}{\mu_{BB}} \qquad \textbf{2. 7}$$

where: μ_{NB} and μ_{BB} are the effective linear attenuation coefficients measured under narrow and broad beam geometries respectively.

A practical and cost efficient method, in comparison to commercial flood sources, is the production of an uncollimated printed transmission source using a standard inkjet printer, for attenuation correction purposes (Van Staden et al., 2011). This transmission source is easily prepared using ^{99m}Tc, which is readily available for routine clinical investigations, and thus cheaper in comparison to the commercial ^{57}Co flood sources. Production of phantoms and flood sources in this manner has been validated and was found to perform favourably to the more commonly used ^{57}Co standard flood source (Van Staden et al., 2007). The use of an uncollimated ^{99m}Tc printed transmission source can easily be implemented for simultaneous emission transmission images of iodine-131-meta-iodobenzylguanidine quantification studies. However, when ^{99m}Tc is used as the emission radionuclide, subtraction of emission data from simultaneous acquired emission-transmission data, results in a transmission image with poor count statistics. The transmission data obtained in this manner are susceptible to noise, resulting in unreliable results (Du Raan et al., 2000).

Recent developments in attenuation correction for planar images involves the use of CT-scout images from hybrid SPECT/CT gamma cameras (Gleisner and Ljungberg, 2012; Minarik et al., 2005; Sjögreen et al., 2005). The use of this method involves rescaling the effective energy (70 keV) of the planar CT-scout image to that of the radionuclide used for the

emission data. Problems encountered with this method include the divergence of the CT beam and the difference in resolution between the CT scan and the gamma camera. This method is susceptible to attenuation correction artefacts due to misregistration (particularly for small objects) (Minarik et al., 2005). The application of this method has proved to yield accuracies of 4 %, with necessary corrections for degradation factors such as scatter, in a heterogeneous Alderson phantom (Minarik et al., 2005). The use of the scout view in hybrid gamma cameras has not yet been commercialized and application of the scout view in this manner entails necessity of files which are not readily provided by the manufacturer. However, this method is potentially superior to the commonly used transmission source method due to the following: a CT-scout view has a high photon flux and is therefore less susceptible to noise, no cross-talk occurs between the energy of the emission and transmission data (the average transmission energy is lower than that used for emission data and the datasets are acquired sequentially) and decay of transmission source is no longer problematic.

2.3.2 Compton scatter interaction of gamma rays.

Compton scattered photons are detected within the photopeak energy window due to the relatively poor energy resolution of the gamma camera. Wider photopeak energy window settings result in inclusion of more counts from primary photons, but also more counts from Compton scattered photons. The presence of γ-ray Compton scatter in nuclear medicine images affects both image quality and activity quantification accuracy. It has been reported, from an investigation using Monte Carlo simulation, that scatter can account for a third of the γ-rays detected by the gamma camera (Ogawa et al., 1991). The effects of attenuation, on quantitative accuracy, are more dominant in comparison to those of scatter particularly for large objects (Frey et al., 2012). However scatter still plays a significant part in the image quantification process. In order to obtain improved quantitative and qualitative nuclear medicine images, scatter must be considered and compensated for.

Scatter results in erroneous spatial information regarding the origin of a γ-ray in the patient. Erroneous spatial information results in increased intensity away from the site of disintegration. For this reason, background intensity is increased and image contrast is reduced. A reduction in contrast makes it more difficult to visually interpret the images and define borders for quantification of organs or tumours. From the definition of contrast; *"differences in intensity in parts of the image corresponding to different levels of radioactive*

uptake in the patient" (Cherry et al., 2003d), the impact of scatter on image contrast is shown in Equation 2.8.

$$C_T = \frac{(I_1 + S) - (I_2 + S)}{I_1 + S} = \frac{I_1 - I_2}{I_1 + S} \qquad \textbf{2. 8}$$

where: C_T is the tumour contrast, I_1 and I_2 are the count rates over the tumour and surrounding tissue respectively, and S is the scattered count rate, which is assumed to contribute equally to both tumour and background. It can be seen from Equation 2.8, that scatter reduces contrast due to the additional factor *S,* in the denominator. Therefore, scatter correction will result in improved image quality (contrast) by removal of the *S* factor. This will result in improved tumour or organ of interest detection. Scatter correction also results in the removal of γ-ray contributions that have occurred away from the site of disintegration. This results in improved activity quantification accuracy for tissue that is at close proximity to surrounding radioactive organs.

Coherent scattered events where no energy loss occurs cannot be distinguished from primary photons and therefore are not correctable. Coherent scattering is only significant for low γ-ray energies of ≤ 50 keV in tissue (Bushberg et al., 2011). Therefore its occurrence is less likely for radionuclides used in nuclear medicine imaging. The probability of Compton scatter occurrence is much higher. Compton scatter entails directional change of a γ-ray with energy loss to a recoil electron resulting in poor spatial and energy information. It is for these reasons that most of the scatter correction methods address Compton scatter. The amount of energy loss by the γ-ray during Compton scatter depends on, the scattering angle relative to its initial direction and γ-ray energy. This relationship is shown in Equation 2.9 (Zaidi and Koral, 2004).

$$E_s = 1 + \frac{E}{m_0 c^2}(1 - \cos\theta) \qquad \textbf{2. 9}$$

where: E_s is the energy of the scattered γ-ray, E is the energy of the incident photon, m_0 is the rest mass energy of the electron and c is the speed of light. The maximum energy lost by the scattered γ-ray occurs when it is back-scattered through 180° from its initial direction (Equation 2.9). Also, E_s increases with increasing energy of the incident γ-ray. Even for large scatter angles of 180° low energy photons, such as those of ^{99m}Tc, result in relatively

small energy changes. However, the maximum energy lost by the incident γ-ray increases for higher energy radionuclides, such as ^{131}I.

The use of the PHA to distinguish between scattered and un-scattered photons (primary photons), based on their energy difference, is not entirely effective due to the limited energy resolution of the gamma camera. It has been reported that γ-rays that might have been scattered once or twice may still be included in a 20 % PHA energy window for ^{99m}Tc, constituting approximately 30 % of the γ-rays recorded in the photopeak (Buvat et al., 1995). Gamma γ-rays that have scattered through angles of 90° may also be recorded in a 20 % PHA window, for gamma cameras with an energy resolution of approximately 10 % (Hutton et al., 2011). The use of a wider energy window results in the inclusion of more primary photons, but also more scattered photons in the PHA window. Owing to improved energy resolution, modern gamma cameras can now mostly employ a 15 % PHA window, without compromising detection of primary photons to a large extent.

It can be deduced from the above that the probability of the inclusion of scatter in the primary window depends upon the gamma camera energy resolution, PHA energy window settings and γ-ray energy. This probability is further affected by the acquisition (distance from detector) and imaging geometries (object shape and size) (Buvat et al., 1995). Gamma rays may be scattered within any of the following components of the imaging process; imaging table, object (patient), collimator or detector. The main concern here is object scatter because it forms a large part of detected events in clinical images (Cherry et al., 2003e). In object-scatter the γ-ray is scattered in the object, but is able to pass parallel through the collimator holes with enough energy to be accepted in the PHA. Large organs have increased probability of object-scatter within the organ itself and can also contribute to detection of scatter in tissue within close proximity. This results in erroneous information regarding radioactive uptake. All the above mentioned characteristics make application of scatter correction techniques important, but also complex and a challenge to implement, in routine clinical practice for quantification purposes.

2.3.2.1 Compton scatter correction techniques.

Compton scatter will further be referred to as scatter. The choice of a scatter correction technique for routine clinical application depends on the following: the ease of its implementation, its practicality and robustness. Most of these factors also determine its use

in commercially available systems. It is important to consider the ultimate application for which a scatter correction technique will be used. Applications may include; improved image quality, absolute activity quantification or verification of scatter models. The activity quantification accuracy achieved by a scatter correction technique is governed by its underlying hypothesis. For this research project scatter correction will be applied in order to obtain quantitative tumour data in a phantom study. Ultimately this may be implemented clinically in an attempt to obtain accurate patient dose calculations.

An overview of scatter correction techniques will be discussed below with a focus on scatter correction techniques that can be applied to planar images. Emphasis will be on techniques that are viable to implement clinically and are commercially available. Scatter compensation techniques will be divided into two broad categories namely: those based on multiple energy acquisitions and those based on modelling the scatter distribution.

2.3.2.1.1 Effective attenuation coefficient for scatter compensation.

In practice attenuation correction is performed by multiplying the GM of counts by the exponential function shown in Equation 2.4. This function can be calculated from measurements of the effective linear attenuation coefficient and object thickness. The object thickness through the organ of interest may be determined by assuming a standard body size (Cherry et al., 2003c), physical measurements or from using transmission data obtained through radionuclide transmission data or CT images (Pereira et al., 2010; Sjögreen et al., 2002).

The measured linear attenuation coefficient is influenced by the amount of scatter included in the measurement, and is termed the effective linear attenuation coefficient. Lower linear attenuation values imply increased scatter contribution and vice versa. Linear attenuation coefficients are termed narrow beam and broad beam coefficients for the exclusion and inclusion of scatter respectively. Examples of these theoretical values for ^{99m}Tc in tissue are 0.155 cm^{-1} and 0.120 cm^{-1} for narrow beam and broad beam measurements respectively (Cherry et al., 2003c). Attenuation, in accordance with Equation 2.4, is described for narrow beam conditions. However, in the clinical environment imaging is performed under broad beam geometry and thus scatter contribution must be taken into consideration. Scatter and attenuation arise from the same phenomenon. For this reason, if the inclusion of scatter is not

taken into consideration in the linear attenuation coefficient value, overcorrection of activity distribution may result.

The application of an effective linear attenuation coefficient with the GM, in planar images, was performed for the following studies: In a phantom study by Pereira et al., (2010) where reasonable activity quantification accuracies in the range of -10 % to 2 % were achieved for ^{99m}Tc and ^{131}I in a uniform cylinder with sphere inserts. This method yielded poorer results in a torso phantom where sphere activity underestimations were up to 33 %. In a phantom simulation study conducted by Jönsson et al., (2005), it was shown that the use of an effective linear attenuation coefficient of 0.13cm^{-1}, for ^{99m}Tc in water, resulted in large activity quantification errors (-24 % to 40 %). Both the abovementioned studies demonstrate that the use of an effective linear attenuation coefficient does not take into account that scatter distribution depends on the attenuation at the point of interaction. The governing hypothesis that attenuation is uniform, is incorrect as it assumes that attenuation is the same for all media representing the object. The method works for uniform activity distribution in a uniform attenuating medium, however it fails in heterogeneous media, such as those encountered in a torso phantom and the torso of a patient. The poor performance of an effective linear attenuation coefficient in heterogeneous media should be considered in the attempt to reduce quantification errors. Attenuation depends on source geometry (configuration and composition), the radionuclide used and gamma camera performance characteristics. Therefore the choice of the value for the effective linear attenuation coefficient is important and should be measured for a particular gamma camera system and source geometry. It has been shown in a phantom study, that a deviation of 0.01 cm^{-1} in the effective linear attenuation coefficient value results in a 15 % change in the activity quantification accuracy of planar images using ^{99m}Tc (Norrgren et al., 2003).

The Chang algorithm multiplies a reconstructed SPECT image by an ACF, which is a function of the attenuator thickness and effective linear attenuation coefficient, on a pixel-by-pixel basis for attenuation correction (Chang, 1978). This method's goal was to achieve a uniform activity distribution in a uniform SPECT image, rather than quantitative accurate values. The method yields reasonable results for brain (Rajeevan et al., 1998) studies, but fails in areas of heterogeneous media, such as that encountered in the thorax i.e. myocardial perfusion studies.

Another factor to describe the extent by which measured attenuation may be increased under broad beam condition compared to the narrow beam geometry, is the buildup factor (Wu and Siegel, 1984). The buildup factor is a constant by which the exponential function shown in Equation 2.4 is multiplied, to account for scatter in an attempt to obtain accurate quantitative data. The buildup factor can be measured as the ratio between count rates measured in air and that measured in the attenuator for various depths. In so doing, the influence of factors such as; source geometry (source depth and configuration) and gamma camera parameters (collimator used) on quantification is taken into consideration. Application of this method to an anthropomorphic phantom, in activity quantification of the spleen using ^{111}In, showed accuracies in the range of 1.4 % to 1.8 % (Van Rensburg et al., 1988).

2.3.2.1.2 Multiple energy window scatter correction.

The methods in this category use energy distributions acquired in different energy windows to estimate scatter in the photopeak. Therefore, these methods are susceptible to changes in detector non-uniformity response. It has been reported that non-uniform response of PMTs may result in counts (from scatter images) acquired with the multiple windows, for scatter correction purposes, being noisy and unstable (Ichihara et al., 1993). Therefore when using these scatter correction methods, it is imperative to ensure the stability of the gamma camera detector. Routine QC tests such as the intrinsic uniformity and energy peaking may be conducted to determine the stability of the gamma camera.

a) Dual photopeak window method.

The dual photopeak window method hypothesized that the photopeak scatter fraction (scatter to primary events) can be obtained by dividing the photopeak window into two non-overlapping energy windows. The scatter fraction is obtained using the analytical relationship between the count ratios of these windows. The method has been demonstrated to qualitatively (improved contrast) and quantitatively (improved activity quantification) improve planar and SPECT phantom images (King et al., 1992; Kojima et al., 1992). This method showed close agreement to true scatter estimates generated with Monte Carlo methods (Hademenos et al., 1993; Ljungberg et al., 1990). However, the method is not viable to implement due to the following shortcomings: The hypothesis assumes that scatter does not vary with spatial location on the detector i.e. spatially invariant. This is not true, since scatter distribution will change with interaction position in the detector and will be

subject to drifts in the detector response. The relationship between the count ratios must be found using Monte Carlo simulations or by experiment, and this will vary with acquisition geometry. Thus, the method cannot be optimised for all clinical conditions making it less favourable to implement in a clinical environment. The stability and the accuracy of the method will be determined by the mathematical function used to represent the relationship between the count ratios. Maintenance of the accuracy achieved with the method implies reproducible positioning of the energy windows in the same manner as was done during optimization. Repositioning of the photopeak window will be difficult, as this is susceptible to drift in detector response (Ljungberg et al., 1994). It has been reported by Buvat et al., (1995), employing Monte Carlo simulation, that this method results in biased errors with regard to extreme low or high values of primary counts. This poses a problem due to the fact that quantification is mainly done for areas of abnormal uptake.

b) Channel ratio method.

Another method that employs the division of the photopeak into two symmetrical windows, as motioned above, is the channel ratio method developed by Pretorius et al., (1993). The assumption made in this method is that the ratio of the scatter events in these two windows is constant. However, this assumption does not hold true, as it implies that scatter is spatially invariant. It was shown in a Monte Carlo simulation study conducted by Naudé et al., (1996) that the use of an average ratio yielded accurate quantitative results. However, this does not account for the fact that scatter distribution changes with acquisition geometry. Also the constants used to relate the counts in the two windows need to be optimised making the method less favourable for routine clinical applications.

c) Asymmetric window method.

Alternatively, the asymmetric window method employed scatter rejection by means of slight shift of the spectral window towards the higher energies of the photopeak (Beck et al., 1968). Despite its qualitative improvement of images the detection efficiency achieved with this method was low due to exclusion of many primary counts (Collier et al., 1984; Graham et al., 1986). Other challenges experienced with this method include optimisation of the spectral window shift which depends on the acquisition and imaging geometry. This method is also affected by electronic instability and energy window settings, making it difficult to optimise for routine clinical use (Buvat et al., 1994).

d) The dual energy window.

The dual energy window (DEW) scatter correction technique was developed by Jaszczak et al., (1984) in an attempt to quantitatively and qualitatively improve SPECT images. The method is based on acquisitions using two energy windows namely: the photopeak window ($W_{photopeak}$) and a lower wide sub-window (W_{lower}) located below the photopeak energy window, as shown in Figure 2-3. It was assumed that scatter in the photopeak can be represented by a fraction, denoted by a scatter factor constant *k*, of the events detected in the sub-window. This assumption does not represent the true nature of the scatter characteristics. The lower energy window contains more second order scatter events (scatter from larger angles) in comparison to events detected in the photopeak window, which consists of more first order scatter (Ichihara et al., 1993). The probability of multiple scatter is higher for photons in the lower sub-window in comparison to those in the photopeak window. This was confirmed in a comprehensive study conducted by Buvat et al., (1995) investigating scatter correction techniques using Monte Carlo simulation. It was found in this study that the probability of higher orders of scatter was larger (55 %) in the sub-window compared to the photopeak window (18 %). Although the scatter estimate in this method is not a true representation of the scatter distribution, scatter correction improves qualitative and quantitative results in Monte Carlo simulation studies of the brain (Ljungberg et al., 1994). The qualitative improvement of the images is attributed to the over correction far from the source and an under correction near the source, which results in improved image contrast (Hutton et al., 2011).

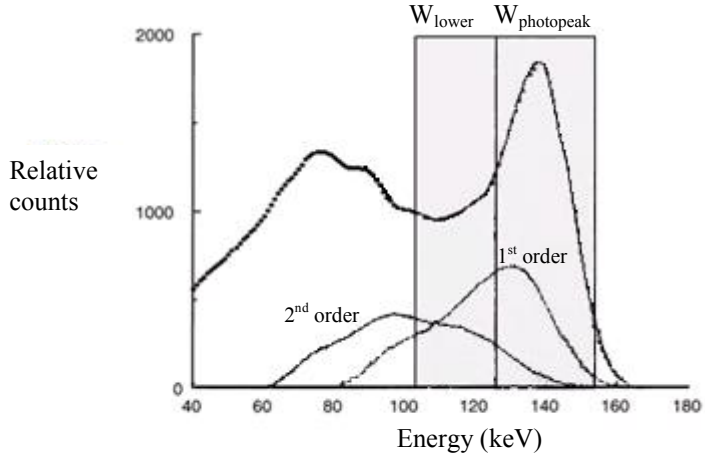

Figure 2-3: *Diagrammatic sketch showing dual energy windows superimposed on an energy spectrum from Monte Carlo simulation of ^{99m}Tc line source in a water cylinder, showing contribution of different order scatter in the photopeak (Zaidi and Koral, 2004).*

Buvat et al., (1995) found that the mean value of the scatter factor *k,* that makes scatter in the lower sub-window equivalent to scatter in the photopeak, was 0.53. The method was found to visually improve interpretation of planar mammographic phantom images and increased reporter confidence for detection of small tumour inserts (Buvat et al., 1998). The choice of the scatter factor is crucial and makes this method sensitive to variables, which include: energy window settings (width of sub-window), energy resolution of the gamma camera and the imaging geometry (source size and depth). The criterion chosen to determine the scatter factor, including parameters such as the width of the lower sub-window, will also determine the accuracy achieved with this method.

The scatter factor value obtained for ^{99m}Tc from experiments and Monte Carlo simulations was 0.50 and 0.57 respectively (Zaidi and Koral, 2004). Although there has been much acceptance in literature that the scatter factor to be used is 0.50, the dependence on the above mentioned variables makes it necessary to optimise the method for a specific system. Variation of scatter distribution with source depth was demonstrated in a SPECT study conducted by Ljungberg et al., (1990) using Monte Carlo simulations. It was reported in this study that the scatter factor deviated from the commonly used value of 0.50 at shallow depths. In a phantom study by Koral et al., (1990), it was demonstrated how the scatter factor varied with source size, with the trend of a lower *k* value for increased source size. Luo et al., (1995) further investigated the variation of *k* in SPECT studies using Monte Carlo

simulations. This study demonstrated that the *k* value decreased with increased background activity for a constant volume of interest definition.

e) The triple energy window.

The triple energy window (TEW) scatter correction is a position dependant scatter correction method developed by Ogawa et al., (1991). It utilises the count distribution in the three energy windows used to acquire the energy spectrum for each pixel. In this method scatter in the photopeak is approximated using the photopeak energy window and two narrow energy sub-windows placed below and above the photopeak (Figure 2-4). As opposed to the DEW method proposed by Jaszczak et al., (1984), scatter contribution in the photopeak is estimated by the area under a trapezoid. The area of the trapezoid is calculated by the height of the counts in the narrow energy sub-windows above and below the photopeak as well as by the width of the photopeak window, as shown in Equation 2.10. The true shape of the scatter contribution is a complex function of many variables, however, the assumption of a trapezoidal shaped scatter estimate seems a practical and reasonable approximation (Ogawa et al., 1991).

$$C_{TEW} = \left(\frac{C_{lower}}{W_{lower}} + \frac{C_{higher}}{W_{higher}} \right) \times \frac{W_{photooeak}}{2} \qquad \textbf{2. 10}$$

where: C_{TEW} is the scatter count estimate within the photopeak window calculated using the TEW scatter correction technique, C_{lower} and C_{higher} are the counts in the sub-windows below and above the photopeak window respectively, W_{lower} and W_{higher} are the widths of the sub-windows below and above the photopeak respectively and $W_{photopeak}$ is the width of the photopeak window. It can be seen from Equation 2.10 that the widths of the energy windows are taken into consideration in the calculation of the scatter estimate, should there be changes in their placements on the energy spectrum.

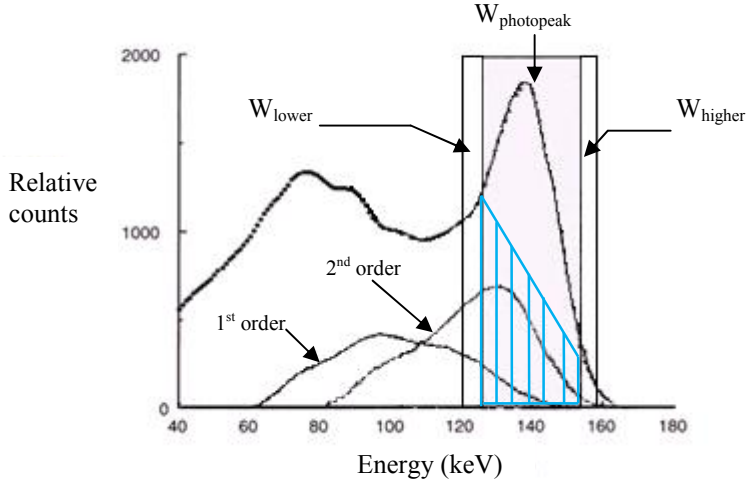

Figure 2-4: *Diagrammatic sketch showing the triple energy windows, superimposed on an energy spectrum from Monte Carlo simulation of ^{99m}Tc line source in a water cylinder, illustrating estimation of scatter in the photopeak by the triple energy scatter correction technique as an area under the trapezoid (Zaidi and Koral, 2004).*

Scatter in the photopeak window is numerically compensated for by subtracting the scatter events, obtained using the TEW method, from the photopeak events on a pixel-by-pixel basis, in order to obtain primary events, as shown in Equation 2.11.

$$C_{primary} = C_{photopeak} - C_{TEW} \qquad \textbf{2. 11}$$

TEW scatter estimate adapts well to downscatter from radionuclides with multi energy emissions such as iodine-123 (^{123}I), with primary energy emissions at 159 keV and higher energy emissions with an average energy of 507 keV. Comparison of scatter ratios between different radionuclides indicated that proportion of scattered photons in ^{123}I to be higher than ^{99m}Tc due to down-scatter from the higher γ-ray energy emissions with this method (Buvat et al., 1995). The method proved to improve quantitative accuracy and improve image contrast in a Monte Carlo simulation of a SPECT phantom study using ^{201}Tl and ^{99m}Tc (Ogawa, 1994). The performance of the TEW scatter correction technique was also investigated in clinical cardiac perfusion SPECT studies for simultaneous acquisitions of ^{201}Tl and ^{123}I , where it was found to improve specificity for detection of abnormal myocardium defects (Yang et al., 1997). It has been reported, in a Monte Carlo simulation of a SPECT study using gallium-67, that the TEW estimated true scatter data well for noise free projections (Ljungberg and Strand, 1989). The method was reported to improve the contrast and

sharpness of clinical cardiac images acquired using ^{201}Tl, resulting in increased reporter confidence with respect to normal and abnormal defects (Changizi et al., 2008).

For single γ-ray emission radionuclides, such as ^{99m}Tc, it has been reported that the narrow sub-window above the photopeak window may be set to zero (Buvat et al., 1994; Ichihara et al., 1993; Ljungberg et al., 1994). This is attributed to the low counts obtained in this window, making the method susceptible to noise and statistical fluctuation. The TEW method then approximates the DEW method, as shown in Equation 2.12, when the window widths of the photopeak and the sub-window below the photopeak are equal, and will be termed the modified TEW scatter correction technique.

$$C_{TEW\_2} = \left(\frac{C_{lower}}{W_{lower}} \right) \times \frac{W_{photopeak}}{2} \qquad \textbf{2. 12}$$

where: C_{TEW_2} is the scatter count estimate within the photopeak window calculated using the modified TEW scatter correction technique, implemented for single emission radionuclides such as ^{99m}Tc. This method differs from the above mentioned DEW (Section 2.3.2.1.2(d)), as it takes the energy window widths into consideration. The advantage of this method over the DEW is that there is no need for any system dependant calibration and the energy window widths are incorporated in the scatter factor calculation. This makes the modified TEW scatter correction method more practical to implement for various and complex scatter geometries imaged with single emission radionuclides.

Initially the TEW method used a wide photopeak window (~ 24 keV) with two narrow sub-windows of 2 keV (Ogawa et al., 1991). The use of narrow sub-windows made the method susceptible to noise and statistical fluctuations which were partly overcome by filtering and thereby improving image quality (King et al., 1997). The TEW method has been shown to successfully employ wider energy sub-windows (7 % of photopeak energy) in brain studies, which resulted in improved quantitative data with less noise (Iida et al., 1998; Shidahara et al., 2005). Kojima et al., (2004) employed a 7 % sub-window for scatter correction of transmission data, where the scatter factor was optimised from 0.5 to 1.0. Activity accuracies within 5 % of the truth for lung quantification have been reported for SPECT phantom studies using ^{131}I when 6 % sub-window energy widths were used (Dewaraja et al., 1998). It seems from empiric experience that the use of 7 % sub-windows results in accurate quantitative data. Further investigations regarding the scatter factor may be necessary in order to optimise the TEW method for a specific imaging protocol.

Most of the above mentioned scatter correction techniques, hypothesised that scatter is spatially invariant, which introduces inaccuracies. These methods are also very sensitive to non-uniform response on the detector system. Dependence on the non-uniformity response of the detector could be overcome by application of energy correction maps. However, this is dependent on the spectral range over which the energy correction map is applied. This would imply that the correction map be available for each energy window, which is not the case with gamma cameras. Most gamma cameras need some form of calibration factor optimisation which depends on the acquisition and imaging geometries. This makes these methods less robust and unfavourable for routine clinical applications. For these reasons most of the above mentioned methods are not used clinically.

From the above, it is evident that there is no simple solution to optimise these methods for all imaging environments. Of the methods discussed above, only the TEW and DEW have withstood the test of time. Implementation of these methods is mostly performed post processing where either the image acquired using the sub-window may be multiplied by *k* and subtracted from the photopeak image, or the counts obtained from the region of interest (ROI) sub-window image are multiplied by *k* and subtracted, on a pixel-by-pixel basis, from the ROI counts in the photopeak. The application of this method in SPECT images is similar, either involves reconstruction of the images acquired in the sub-window and photopeak window and application of the TEW or DEW thereafter or compensation during reconstruction.

2.3.2.1.3 Model based scatter correction.

Model based scatter correction methods result in improved activity quantification. This is attributed to the fact that these methods model the scatter function more accurately and thus better resemble the true scatter distribution. These methods are more complex to implement routinely however, they are advantageous as a means of validation for the above described multiple window methods. The latest improved modelling scatter techniques are mainly applied to SPECT acquisitions and are incorporated in the reconstruction process.

a) Effective source scatter estimation.

The effective source scatter estimation (ESSE) incorporates modelling of non-homogenous media and Compton interactions along the entire ray-path to the face of the detector (Frey and Tsui, 1996). The advantage of this method is that it results in qualitative improvement of

images (images are less noisy) in comparison to window based subtraction methods mentioned above. The downfall of this method with regard to this research project is that it is not applicable to planar imaging.

b) Monte Carlo simulation.

Monte Carlo simulation allows the study of the distribution properties of scattered and un-scattered photons. This makes it a useful tool for the following: the development of scatter models, evaluation and validation of scatter correction techniques, as well as their comparative assessment conducted in many literature studies, some mentioned above (Section 2.3.2.1.2). There is wide access to Monte Carlo programs used in nuclear medicine, such as the SIMIND (Ljungberg and Strand, 1989), SimSET (Harrison et al., 1993; Ljungberg et al., 1998) and GATE (Jan et al., 2004) programs. Significant reduction in computation time has been reported when scatter in projections of SPECT images is modelled using Monte Carlo simulation (Beekman et al., 1999). However, at this time Monte Carlo simulation of scatter response functions has not been commercialized for routine clinical use. The dependence of the scatter distribution on object variables has been demonstrated in a Monte Carlo study (Ljungberg and Strand, 1991). Although improved computer hardware capabilities have reduced computational time needed to perform the simulations, it is still very time-consuming in comparison to normal routine acquisition and processing times. For this reason Monte Carlo simulations are not incorporated into routine clinical practice.

c) Analytical models.

Analytical models were developed in order to simplify and speed up the modelling of scatter distributions. They are based on the Klein-Nishina equations that are used to describe the probability of scatter with an electron through a given angle (Section 2.3.2) (Zaidi and Koral, 2004). Techniques based on these models have advanced to 3D scatter and attenuation correction in SPECT data, which involves ray-tracing in 3D, resulting in improved accuracy (Laurette et al., 2000). However they are computer intensive and demand long computational times and thus have practical disadvantages.

d) Convolution based models.

Convolution scatter compensation is based on the assumption that scatter in the photopeak can be estimated by the convolution of the photopeak data with a mono-exponential function used to represent the scatter distribution (Axelsson et al., 1984; Msaki et al., 1987). The mono-exponential function was optimised using experiments or Monte Carlo simulations. Disadvantages of this method include; that both scattered and primary photons in the photopeak was used to estimate the scatter, a constant scatter fraction was employed to scale the scatter estimate and the convolution was done with a spatially invariant function (Buvat et al., 1994). Variations have been proposed to improve the method's accuracy, and include the following: application of the mono-exponential function to opposing views applied in a successive approximation of the iterative process (Bailey et al., 1987), the use of combined mono-exponential and Gaussian functions to model the scatter distribution (Narita et al., 1996) and the transmission-dependent convolution subtraction which incorporates the use of transmission data to scale the estimated scatter on a pixel-by-pixel basis (Meikle et al., 1994).

Convolution based scatter estimates were scaled by applying the Chang attenuation correction to brain studies. Improved quantitative data found in these studies was comparable to the results found using the TEW technique (Shidahara et al., 2005). It was also shown in the variations discussed above that the use of the iterating process during SPECT to estimate scatter resulted in improved accuracy. Currently, the scatter fraction can be scaled more accurately using a transmission map obtained from CT data. Extension of the method by Meikle et al (1994), gave reasonable activity distributions in clinical SPECT lung ventilation/perfusion studies when combined with CT data, with accuracies in the range of -7 % to 4 % (Willowson et al., 2008).

Although the accuracy of the convolution based scatter estimation method improved, the assumption that both scatter and unscattered image data in the photopeak can be used during the estimation remains doubtful. Models used to determine the scatter response function must still be improved to represent the true nature of the scatter distribution.

2.4 Region of interest definition and organ overlap.

Another important factor to consider when performing activity quantification is the ROI selection for organ delineation. Planar quantification accuracy is affected by the geometry of the object of interest, with improved accuracy found in isolated objects with no overlying or

underlying background activity (Siegel et al., 1999). A drawn ROI isolates the activity distribution to a particular organ (or object) and distinguishes it from the surrounding background activity or activity from adjacent organs. Gamma camera software packages include ROI applications for automated and semi-automated edge detection and definition of regular (ellipse and circles) and irregular shapes with the necessary statistical analysis information. In most cases tumours are irregularly shaped, contrary to the spherical representation in most phantom studies. Therefore ROI definition heavily depends on the experience of the end user, as delineation is complicated by poor image quality with unclear borders. To overcome these obstacles the user should use and draw the ROI large enough to encompass all, or most of the counts representing the activity distribution of the object of interest. However, this approach is hampered by spill-in of activity from adjacent organs and spill-out of activity from the object of interest due to PVE (discussed in Section 2.5), as well as superimposition of activity when planar imaging is used (Frey et al., 2012).

In most instances software allows defined ROIs to be stored as separate files and may be used repeatedly for the same object of interest. On many occasions tumour or organ delineation in clinical studies is performed by an experienced technologist or physician, as was done in a clinical trial for whole body quantification (Sjögreen et al., 2005). It has been observed, that in many instances in the literature, where the focus of the research is quantification, little, if any, attention is paid to ROI definition (Zaidi and Koral, 2005).

An inexact approach for background activity correction in planar images includes a ROI defined adjacent to the organ of interest with care to exclude activity distribution within other objects. The counts obtained from this ROI are normalized to the object area and subtracted from the organ of interest counts. However, this approach does not take into consideration the superimposed source volume (i.e. the volume of the organ of interest included in the background volume), which should be excluded in background ROI definition. Failure to do so may result in overestimation of background activity, and thus underestimation of the object of interest activity. Norrgren et al., (2003) conducted a phantom study that compared the above mentioned conventional background correction method to a method which considers organ thickness and total body thickness (Buijs et al., 1992). It was found that the conventional method underestimated organ activity by 20 % for the liver and heart inserts and 5 % in the kidney insert in comparison to the organ thickness method (Norrgren et al., 2003). Another background correction method that attempts to correct for underestimation of

activity distribution due to background overestimation, includes source volume in correction of background activity (Kojima et al., 1993). This method, as well as the above mentioned organ thickness method, was included in a comparative phantom study of five different methods for background correction (Buijs et al., 1998). It was found in this study that these two methods resulted in improved activity quantification, compared to the others, where the source volume correction yielded better results at low source-to-background activity levels. Other attempts which include corrections for background (using source volume) and organ overlap in planar quantification have been made. These include ROI definition using CT information and determination of the volume associated with that ROI (Sjögreen et al., 2002). This work was further extended to determine organ thickness using attenuation maps (Sjögreen et al., 2005).

Superimposition of activity present in planar imaging is overcome by SPECT imaging. Volume determination in SPECT studies is more accurate than in planar studies, as volumes in SPECT is derived from 3D information (Zaidi, 1996). SPECT data results in improved contrast due to elimination of superimposed activity, thereby making delineation of object borders easier. There is no universal accepted method for ROI definition in nuclear medicine images as object detection is affected by factors, such as the shape of object, the objects proximity to adjacent organs and image quality (decreased contrast complicates delineation). However, the use of additional transmission information from hybrid imaging, which includes the use of a CT-scout image and volume determination from CT data, seems to be gaining popularity.

The impact of misdefinition (variability in organ delineation) and misregistration (between emission and transmission data) errors, on SPECT and planar quantification accuracy was investigated (He and Frey, 2010). It was found that misdefinition errors had a larger impact on SPECT activity quantification accuracy than planar quantification. One voxel misdefinition was found to result in an 8 % error in quantification accuracy and the errors increased in small organs with low radioactivity uptake. Another important factor to consider when investigating the effects of organ delineation is the sampling, as this affects the variability in ROI definition and thus precision of quantification accuracy. A guideline for the pixel size used in the representation of the object is that it should be less than or equal to one third of the full width at half maximum (FWHM) (See Section 2.5). The effects of matrix size on PET quantification, using standard uptake values (SUVs), was studied by

Adams et al., (2010). It was demonstrated in this study that a matrix shift of less than a voxel, where the object is off-centre within a voxel, resulted in an underestimation of the maximum SUV value. This was attributed to the fact that no voxel represented the true maximum SUV due to the shift. It was also shown that better sampling resulted in less variation in the quantified SUV. This is attributed to the fact that smaller pixels resulted in less variation from matrix shift.

2.5 Partial volume effects.

Partial volume effect (PVE) refers to the phenomenon whereby image intensity or counts do not represent the actual amount of activity contained in the imaged object. This is attributed to the gamma camera's limited spatial resolution, as well as the sampling of the image in an image matrix.

The gamma camera spatial resolution is characterized by the spread of the profile obtained from the image of a point source. Spatial resolution is defined as the FWHM of the point spread function (PSF). Spatial resolution is also represented by the modulation transfer function (MTF) which is the Fourier transform of the PSF. This function describes the extent to which an object can faithfully be represented by its image. Although the MTF is a more complete means of characterizing the gamma camera spatial resolution (it accounts for factors such as septal penetration and scatter), it is an impractical characteristic to routinely use as a performance criterion of the gamma camera's spatial resolution (Saha, 2012). As mentioned in Section 2.2.2 (b), the gamma camera's system spatial resolution is affected by the intrinsic resolution (determined by the detector crystal thickness and influenced by statistical variations) and collimator resolution (depends on the collimator design). There is always a trade-off between spatial resolution and detector efficiency. Improved system spatial resolution can be obtained by using a thinner detector crystal and smaller or longer collimator holes, which will all result in poorer detection efficiency. For this reason, a variety of collimator designs are available with the gamma camera for optimization of either of these performance characteristics, depending on the investigation at hand. The impact of these factors is further complicated by the object geometry (object size) and acquisition geometry (imaging distance and γ-ray energy).

Partial volume results in spill-out of the detected events (counts) i.e. the image counts are not only contained in the respective corresponding pixel, but also smeared out to the

neighbouring pixels. Therefore the true activity distribution is defined by a larger region. The concept of PVE has a larger impact on smaller objects less than three times the size of the FWHM of the gamma camera (Hoffman et al., 1979; Soret et al., 2007). Although the total activity (events) in smaller objects may be preserved by the sum of all pixels attributable to the object intensity, the individual pixels do not represent the actual activity contained in them, but are observed to have lower activity (underestimate actual activity) (Figure 2-5). Therefore activity within the object will also be detected outside the area (ROI) representing the object. Conversely this effect results in spill-in of activity from adjacent objects into the object of interest, which may result in overestimation of the activity in the object of interest. It is obvious that a pixel may contain a mixture of activity distributions (counts) from the object of interest and neighbouring objects, therefore the actual contours of the object are not perfectly represented in the image matrix. This effect is aggravated by inadequate sampling where larger pixels result in increased uncertainty in the border representation of the object by the image. Thus PVE will result in biased quantification results, especially in small objects, if not compensated for (Frey et al., 2012).

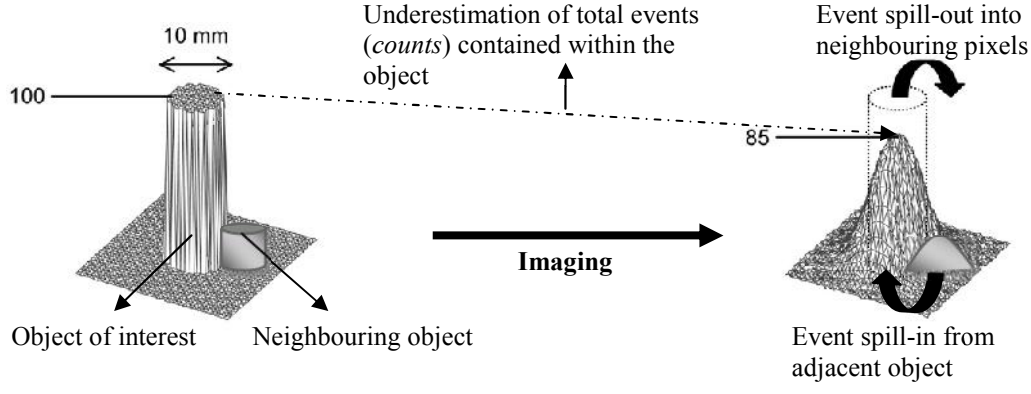

Figure 2-5: *2D illustration of partial volume effects results in spill-out of events from an object of interest into neighbouring pixels (outside actual object), thereby underestimating total activity contained within the object, and spill-in of events from the adjacent object into the object of interest (Soret et al., 2007).*

One of the methods for partial volume correction is the use of the recovery coefficient. This coefficient describes the ratio between the measured and true activity (or concentration) and may be generated as a function of object size for well defined shapes. In so doing, characterization of the gamma cameras PVEs for specific shapes is generated. It is easily

implemented in phantom studies where true activity and object size can be measured (Thomas et al., 2005; Willowson et al., 2008). However, this is problematic in clinical studies where organ and tumour sizes are unknown with irregular geometries. The sizes of the tumours and organs may be determined from CT or MRI studies, but it would be cumbersome to model partial volume from irregular geometries, as each clinical investigation would be unique. On the other hand, due to the above described spill-out effects, ROI definition can be used to recover the activity distributed to neighbouring pixels. This may be achieved by drawing a ROI large enough to include all counts representative of the object activity distribution. This method can be easily implemented in routine clinical investigations. It is however limited due to spill-in of activity distribution from surrounding organs and background activity.

2.6 Collimator choice and septal penetration.

Correspondence of spatial location between the image and object is attempted with the use of the principle of absorptive collimation. This means that only γ-rays travelling in a direction allowed by the collimator holes project an image onto the detector, the rest are absorbed by the collimator septa. One of the main determining characteristics of collimator design based on photon energy i.e. whether it is a high, medium or low energy collimator, is the septa thickness. Usually the septal thickness is chosen to be sufficient to stop γ-rays of the principle γ-ray energy. This principle works well in radionuclides, such as ^{99m}Tc, with only one primary γ-ray energy of 140 keV. However, this concept falls short for radionuclides with higher energy emissions than the principle γ-ray energy, such as ^{123}I (159 keV) and ^{131}I (364 keV), with γ-ray energy emissions of up to 529 keV and 723 keV respectively. The collimator septa cannot be chosen thick enough to stop all γ-ray energy emissions by these radionuclides without compromising resolution. Thus, the γ-rays of higher energy will pass through or scatter in the septa resulting in septal penetration. Septal penetration is constant for a specific collimator and radionuclide. Poor image quality due to septal penetration (increased background resulting in decreased contrast), can affect image quantification and reproducibility of ROI selection (Macey et al., 1995). Septal penetration results in increased sensitivity (discussed below) of the detector system. The convolution method for scatter correction, has the advantage of including the effects of septal penetration in the scatter correction (Msaki et al., 1987).

The collimator choice for a specific radionuclide will affect scatter tails due to septal penetration, longer scatter tails are particularly pronounced for medium and high energy γ-rays (Frey et al., 2012). This phenomenon was demonstrated in a Monte Carlo simulation study by Fleming and Alaamer, (1996) using phantom SPECT acquisitions. In this study acquisitions were performed on two separate gamma camera systems using ^{99m}Tc and ^{123}I where a low energy general purpose collimator was employed for both radionuclides. It was found that the scatter tails were increased for ^{123}I which was attributed to the septal penetration by its higher γ-ray energy emissions. Recommendation for the use of a medium energy collimator was made in order to reduce septal penetration. Other studies have shown the medium energy collimator to be the better choice when imaging with ^{123}I due to improved image contrast and ease of organ delineation for quantification purposes (Bolmsjö et al., 1977; DeNardo et al., 1985; Macey et al., 1986). Collimator choice for imaging with ^{123}I with regard to this research project will be addressed in Chapter 4.

2.7 Gamma camera sensitivity.

An important characteristic of the gamma camera to consider is the sensitivity expressed in units of count rate per unit activity (counts/s/MBq), used to convert image count rate into units of activity for quantification purposes. The gamma camera sensitivity depends on, crystal thickness, the collimator type, radionuclide energy, PHA window width settings, imaging geometry, photon attenuation and scatter, count rate losses, ROI definition and PVE (King and Farncombe, 2003). Conventional sensitivity measurements, for quantification purposes, are measured following the NEMA recommended method using a circular radioactive source imaged at 10 cm from the detector surface (NEMA, 2007). Sensitivity measurements using a parallel hole collimator are independent of source to collimator distance and result in less geometric distortion. It is for these reasons that these collimators are employed for sensitivity measurements (Siegel et al., 1999). However, care should be taken when performing these measurements to use the applicable collimator for the respective radionuclide. It has been shown that sensitivity decreases with increasing source collimator distance for isotopes such as ^{123}I and ^{131}I when low energy collimators were employed (Fleming and Alaamer, 1996). This was attributed to septal penetration which decreased with increasing source to collimator distance, the same way as with no collimator.

Sensitivity measurements using NEMA recommendations entails the use of unattenuated counts rate (measured using a low attenuating medium such as a Petri dish) to convert

attenuated count rates (from patient) to units of activity for quantification purposes. As a consequence of its dependence on the abovementioned variables, it is recommended that the sensitivity should be measured under the same imaging and acquisition geometries as those used for the quantification data. Sensitivity measurements for quantification purposes can be performed in a similar geometry to that of the quantified object (Van Rensburg et al., 1988). In so doing, the same processing techniques as those used for the quantified data are adhered to. This includes using the same criteria for ROI definition as that used for quantified data, as this can alter the sensitivity and have a large impact on quantification accuracy. Quantification accuracies of 3.6 % were reported in a SPECT/CT study where the system volume sensitivity was acquired with a cylindrical phantom where the same acquisition parameters and processing protocols as those used for quantification data were used (Zeintl et al., 2010). Acquisition and processing protocols of sensitivity measurements should be the same as those used for the quantified data. Consistency of these protocols should be maintained to avoid variability in the quantification accuracy.

2.8 Discussion.

Quantification of activity distributions in nuclear medicine imaging has, over the years received, and continues to receive much attention. This is attributed to the quantitative and qualitative advantages offered by these images (Chapter 1, Section 1. 2). A major role of planar activity quantification is in whole body images, where the accuracy achieved is important due to its application in internal dose calculations. From the above literature discussion, it is evident that there are numerous degradation factors that influence quantification accuracy of planar images, with emphasis on attenuation and scatter. Numerous attempts have been made to improve the accuracy of activity quantification, by applying corrections for these degradation factors.

Attenuation and scatter correction have been shown to be necessary in order to improve quantification accuracy. As discussed above, there are many correction techniques available, however the principles that govern these techniques must be taken into consideration. It is evident that attenuation correction can be determined more accurately with the use of transmission data which takes tissue heterogeneity into consideration. This may be achieved with the use of an external radionuclide transmission source or a CT-scout image. Transmission data using an uncollimated ^{99m}Tc printed transmission source will be employed for attenuation correction in this research project.

From the above mentioned scatter correction techniques, the DEW and the TEW have enjoyed wide application due to their efficiency and practical implementation in the routine clinical environment. For these reasons, these methods are available on commercial systems, such as the Symbia T software package (Syngo MI Applications 2007A; Siemens Healthcare). The TEW scatter correction technique will be used in this research project. There has been limited robust application of model based scatter correction techniques in clinics due to increased demand on computation time.

The PVE, owing to the gamma camera's limited spatial resolution, has been shown to influence quantification and delineation of small organs and thus must be considered. The collimator choice influences the gamma cameras resolution and sensitivity. Incorrect collimator choice may result in increased septal penetration, resulting in poor image quality making delineation of organs for image quantification difficult.

Factors such as organ overlap and background activity, further complicate the quantification process. These factors can be corrected using organ thickness obtained from CT data, however this is not routinely done for planar image quantification. The reliability and precision of the quantification process is affected by the integrity of the equipment used during the quantification process making equipment stability an important consideration. Some of the techniques mentioned above are implemented in Chapter 3 for quantification of ^{99m}Tc planar images and in Chapter 4 for ^{123}I quantification.

References

Adams, M.C., Turkington, T.G., Wilson, J.M., Wong, T.Z., 2010. A systematic review of the factors affecting accuracy of SUV measurements. AJR Am. J. Roentgenol. 195, 310–320.

Axelsson, B., Msaki, P., Israelsson, A., 1984. Subtraction of Compton-scattered photons in single-photon emission computerized tomography. J. Nucl. Med. 25, 490–494.

Bailey, D.L., 1998. Transmission scanning in emission tomography. Eur. J. Nucl. Med. 25, 774–787.

Bailey, D.L., Hutton, B.F., Walker, P.J., 1987. Improved SPECT Using Simultaneous Emission and Transmission Tomography. J. Nucl. Med. 28, 844–851.

Bateman, T.M., Cullom, S.J., 2005. Attenuation correction single-photon emission computed tomography myocardial perfusion imaging. Semin. Nucl. Med. 35, 37–51.

Beck, R.N., Cohen, T.D., Lembares, N., Schuh, M.W., 1968. Effects of scattered radiation on scintillation detector response. In: "*Medical radioisotopes scintigraphy*". IAEA, Vienna. 595–616.

Beekman, F.J., de Jong, H.W., Slijpen, E.T., 1999. Efficient SPECT scatter calculation in non-uniform media using correlated Monte Carlo simulation. Phys. Med. Biol. 44, N183–192.

Bolmsjö, M.S., Persson, B.R., Strand, S.E., 1977. Imaging ^{123}I with a scintillation camera. A study of detection performance and quality factor concepts. Phys. Med. Biol. 22, 266–277.

Buijs, W.C., Massuger, L.F., Claessens, R.A., Kenemans, P., Corstens, F.H., 1992. Dosimetric evaluation of immunoscintigraphy using indium-111-labeled monoclonal antibody fragments in patients with ovarian cancer. J. Nucl. Med. 1113–1120.

Buijs, W.C., Siegel, J.A., Boerman, O.C., Corstens, F.H., 1998. Absolute organ activity estimated by five different methods of background correction. J. Nucl. Med. 39, 2167–2172.

Bushberg, J.T., Seibert, J.A., Leidholdt, E.M., Boone, J.M., 2011. INTERACTION OF RADIATION WITH MATTER. In: "*The Essential Physics of Medical Imaging*". 3rd edition, Lippincott Williams & Wilkins, USA. 33–59.

Buvat, I., Benali, H., Todd-Pokropek, A., Paola, R., 1994. Scatter correction in scintigraphy: the state of the art. Eur. J. Nucl. Med. 21, 675–694.

Buvat, I., De Sousa, M.C., Di Paola, M., Ricard, M., Lumbroso, J., Aubert, B., 1998. Impact of scatter correction in planar scintimammography: a phantom study. J. Nucl. Med. 39, 1590–1596.

Buvat, I., Rodriguez-Villafuerte, M., Todd-Pokropek, A., Benali, H., Di Paola, R., 1995. Comparative assessment of nine scatter correction methods based on spectral analysis using Monte Carlo simulations. J. Nucl. Med. 36, 1476–1488.

Chang, L.T., 1978. A Method for Attenuation Correction in Radionuclide Computed Tomography. IEEE Trans. Nucl. Sci. 25, 638–643.

Changizi, V., Takavar, A., Babakhani, A., Sohrabi, M., 2008. Scatter correction for heart SPECT images using TEW method. J. Appl. Clin. Med. Phys. 9, 2767.

Cherry S.R., Sorenson J.A., Phelps M.E., 2003a. NUCLEAR COUTING STATISTICS. In: "*Physics in Nuclear Medicine*". 3rd edition, Saunders, USA. pp131–147.

Cherry S.R., Sorenson J.A., Phelps M.E., 2003b. INTERACTION OF RADIATION WITH MATTER. In: "*Physics in Nuclear Medicine*". 3rd edition, Saunders, USA. 65–88.

Cherry S.R., Sorenson J.A., Phelps M.E., 2003c. SINGLE PHOTON EMISSION COMPUTED TOMOGRAPGY. In: "*Physics in Nuclear Medicine*". 3rd edition, Saunders, USA. pp299–324.

Cherry S.R., Sorenson J.A., Phelps M.E., 2003d. IMAGE QUALITY IN NUCLEAR MEDICINE. In: "*Physics in Nuclear Medicine*". 3rd edition, Saunders, USA. pp253–272.

Cherry S.R., Sorenson J.A., Phelps M.E., 2003e. THE GAMMA CAMERA BASIC PRINCIPLES. In: "*Physics in Nuclear Medicine*". 3rd edition, Saunders, USA. pp211–226.

Collier, B.D., Palmer, D.W., Knobel, J., Isitman, A.T., Hellman, R.S., Zielonka, J.S., 1984. Gamma camera energy windows for Tc-99m bone scintigraphy: effect of asymmetry on contrast resolution. Work in progress. Radiology 151, 495–497.

DeNardo, G.L., Raventos, A., Hines, H.H., Scheibe, P.O., Macey, D.J., Hays, M.T., DeNardo, S.J., 1985. Requirements for a treatment planning system for radioimmunotherapy. Int. J. Radiat. Oncol. Biol. Phys. 11, 335–348.

Dewaraja, Y., Li, J., Koral, K., 1998. Quantitative ^{131}I SPECT with triple energy window Compton scatter correction. IEEE Trans. Nucl. Sci. 45, 3109–3114.

Du Raan, H., du Toit, P.D., van Aswegen, A., Lötter, M.G., Herbst, C.P., van der Walt, T.N., Otto, A.C., 2000. Implementation of a Tc-99m and Ce-139 scanning line source for attenuation correction in SPECT using a dual opposing detector scintillation camera. Med. Phys. 27, 1523–1534.

Dvorak, R.A., Brown, R.K.J., Corbett, J.R., 2011. Interpretation of SPECT/CT Myocardial Perfusion Images: Common Artifacts and Quality Control Techniques. RadioGraphics 31, 2041–2057.

Eary, J.F., Appelbaum, F.L., Durack, L., Brown, P., 1989. Preliminary validation of the opposing view method for quantitative gamma camera imaging. Med. Phys. 16, 382–387.

Eary, J.F., Pollard, K.R., Durack, L.D., Bice, A.N., Lewellen, T.K., Matthews, D., Press,O.W., Nelp, W.B., Appelbaum, FR., Bernstein, I.,1994. Post therapy imaging in high dose I-131 radioimmunotherapy patients. Med. Phys. 21, 1157–62.

Fleming, J.S., Alaamer, A.S., 1996. Influence of collimator characteristics on quantification in SPECT. J. Nucl. Med. 37, 1832–1836.

Frey, E.C., Humm, J.L., Ljungberg, M., 2012. Accuracy and Precision of Radioactivity Quantification in Nuclear Medicine Images. Semin. Nucl. Med. 42, 208–218.

Frey, E.C., Tsui, B.M.W., 1996. A new method for modeling the spatially-variant, object-dependent scatter response function in SPECT. IEEE Nucl. Sci. Symp. Med. Imaging Conf. Rec. 2, pp.1082–1086.

Gleisner, K.S., Ljungberg, M., 2012. Patient-specific whole-body attenuation correction maps from a CT system for conjugate-view-based activity quantification: method development and evaluation. Cancer Biother. Radiopharm. 27, 652–664

Graham, L.S., LaFontaine, R.L., Stein, M.A., 1986. Effects of asymmetric photopeak windows on flood field uniformity and spatial resolution of scintillation cameras. J. Nucl. Med. 27, 706–713.

Graham, L.S., Neil, R., 1974. In vivo quantitation of radioactivity using the Anger camera. Radiology 112, 441–442.

Hademenos, G.J., Ljungberg, M., King, M.A., Glick, S.J., 1993. A Monte Carlo investigation of the dual photopeak window scatter correction method (SPECT). IEEE Trans. Nucl. Sci. 40, 179–185.

Hammond, N.D., Moldofsky, P.J., Beardsley, M.R., Mulhern, C.B., Jr, 1984. External imaging techniques for quantitation of distribution of I-131 F(ab')2 fragments of monoclonal antibody in humans. Med. Phys. 11, 778–783.

Harrison, R.L., Vannoy, S.D., Haynor, D.R., Gillispie, S.B., Kaplan, M.S., Lewellen, T.K., 1993. Preliminary Experience With The Photon History Generator Module Of A

Public-domain Simulation System For Emission Tomography. Nucl. Sci. Symp. Med. Imaging Conf. Rec. 2 pp. 1154–1158.
He, B., Frey, E.C., 2006. Comparison of conventional, model-based quantitative planar, and quantitative SPECT image processing methods for organ activity estimation using In-111 agents. Phys. Med. Biol. 51, 3967.
He, B., Frey, E.C., 2010. The impact of 3D volume of interest definition on accuracy and precision of activity estimation in quantitative SPECT and planar processing methods. Phys. Med. Biol. 55, 3535–3544.
Heller, G.V., Bateman, T.M., Johnson, L.L., Cullom, S.J., Case, J.A., Galt, J.R., Garcia, E.V., Haddock, K., Moutray, K.L., Poston, C., Botvinick, E.H., Fish, M.B., Follansbee, W.P., Hayes, S., Iskandrian, A.E., Mahmarian, J.J., Vandecker, W., 2004. Clinical value of attenuation correction in stress-only Tc-99m sestamibi SPECT imaging. J. Nucl. Cardiol. 11, 273–281.
Hoffman, E.J., Huang, S.C., Phelps, M.E., 1979. Quantitation in positron emission computed tomography: 1. Effect of object size. J. Comput. Assist. Tomogr. 3, 299–308.
Hutton, B.F., Braun, M., Thurfjell, L., Lau, D.Y.H., 2002. Image registration: an essential tool for nuclear medicine. Eur. J. Nucl. Med. Mol. Imaging 29, 559–577.
Hutton, B.F., Buvat, I., Beekman, F.J., 2011. Review and current status of SPECT scatter correction. Phys. Med. Biol. 56, R85–112.
Ichihara, T., Ogawa, K., Motomura, N., Kubo, A., Hashimoto, S., 1993. Compton scatter compensation using the triple-energy window method for single- and dual-isotope SPECT. J. Nucl. Med. 34, 2216–2221.
Iida, H., Narita, Y., Kado, H., Kashikura, A., Sugawara, S., Shoji, Y., Kinoshita, T., Ogawa, T., Eberl, S., 1998. Effects of scatter and attenuation correction on quantitative assessment of regional cerebral blood flow with SPECT. J. Nucl. Med. 39, 181–189.
International Atomic Energy Agency, 2006. IAEA Quality Assurance for Radioactivity Measurements in Nuclear Medicine, Technical Report Series No. 454. IAEA, Vienna. 63–79.
International Atomic Energy Agency, 2003. IAEA Quality Assurance Atlas for Scintillation Camera Systems. IAEA, Vienna. 12–156.
Izadyar, S., Saber, S., Gholamrezanezhad, A., 2011. Assessment of clinical impact in the application of Chang attenuation correction to lung ventilation/perfusion SPECT. J. Nucl. Med. Technol. 39, 290–294.
Jan, S., Santin, G., Strul, D., Staelens, S., Assié, K., Autret, D., Avner, S., Barbier, R., Bardiès, M., Bloomfield, P.M., Brasse, D., Breton, V., Bruyndonckx, P., Buvat, I., Chatziioannou, A.F., Choi, Y., Chung, Y.H., Comtat, C., Donnarieix, D., Ferrer, L., Glick, S.J., Groiselle, C.J., Guez, D., Honore, P.-F., Kerhoas-Cavata, S., Kirov, A.S., Kohli, V., Koole, M., Krieguer, M., Laan, D.J. van der, Lamare, F., Largeron, G., Lartizien, C., Lazaro, D., Maas, M.C., Maigne, L., Mayet, F., Melot, F., Merheb, C., Pennacchio, E., Perez, J., Pietrzyk, U., Rannou, F.R., Rey, M., Schaart, D.R., Schmidtlein, C.R., Simon, L., Song, T.Y., Vieira, J.-M., Visvikis, D., Walle, R.V. de, Wieërs, E., Morel, C., 2004. GATE: a simulation toolkit for PET and SPECT. Phys. Med. Biol. 49, 4543.
Jaszczak, R.J., Greer, K.L., Floyd, C.E., Jr, Harris, C.C., Coleman, R.E., 1984. Improved SPECT quantification using compensation for scattered photons. J. Nucl. Med. 25, 893–900.
Jönsson, L., Ljungberg, M., Strand, S.-E., 2005. Evaluation of accuracy in activity calculations for the conjugate view method from Monte Carlo simulated scintillation camera images using experimental data in an anthropomorphic phantom. J. Nucl. Med. 46, 1679–1686.

Kim, G.-Y., Lee, H.-K., Jeong, H.K., Woods, M.J., 2005. Comparison of radioactivity measurements with radionuclide calibrators in the Republic of Korea. Appl. Radiat. Isot. 63, 201–205.

King, M., Farncombe, T., 2003. An overview of attenuation and scatter correction of planar and SPECT data for dosimetry studies. Cancer Biother. Radiopharm. 18, 181–190.

King, M.A., DeVries, D.J., Pan, T.-S., Pretorius, P.H., Case, J.A., 1997. An investigation of the filtering of TEW scatter estimates used to compensate for scatter with ordered subset reconstructions. IEEE Trans. Nucl. Sci. 44, 1140–1145.

King, M.A., Hademenos, G.J., Glick, S.J., 1992. A dual-photopeak window method for scatter correction. J. Nucl. Med. 33, 605–612.

Kojima, A., Matsumoto, M., Tomiguchi, S., Katsuda, N., Yamashita, Y., Motomura, N., 2004. Accurate scatter correction for transmission computed tomography using an uncollimated line array source. Ann. Nucl. Med. 18, 45–50.

Kojima, A., Takaki, Y., Matsumoto, M., Tomiguchi, S., Hara, M., Shimomura, O., Koga, Y., Takahashi, M., 1993. A preliminary phantom study on a proposed model for quantification of renal planar scintigraphy. Med. Phys. 20, 33–37.

Kojima, A., Tsuji, A., Takaki, Y., Tomiguchi, S., Hara, M., Matsumoto, M., Takahashi, M., 1992. Correction of scattered photons in Tc-99m imaging by means of a photopeak dual-energy window acquisition. Ann. Nucl. Med. 6, 153–158.

Koral, K.F., Swailem, F.M., Buchbinder, S., Clinthorne, N.H., Rogers, W.L., Tsui, B.M., 1990. SPECT dual-energy-window Compton correction: scatter multiplier required for quantification. J. Nucl. Med. 31, 90–98.

Kossert, K., Thieme, K., 2007. Comparison for quality assurance of ^{99m}Tc activity measurements with radionuclide calibrators. Appl. Radiat. Isot. 65, 866–871.

Laurette, I., Zeng, G.L., Welch, A., Christian, P.E., Gullberg, G.T., 2000. A three-dimensional ray-driven attenuation, scatter and geometric response correction technique for SPECT in inhomogeneous media. Phys. Med. Biol. 45, 3459.

Lee, Z., Berridge, M.S., Nelson, A.D., Heald, D.L., 2001. The Effect of Scatter and Attenuation on Aerosol Deposition as Determined by Gamma Scintigraphy. J. Aerosol Med. 14, 167–183.

Leichner, P.K., Klein, J.L., Garrison, J.B., Jenkins, R.E., Nickoloff, E.L., Ettinger, D.S., Order, S.E., 1981. Dosimetry of ^{131}I-labeled anti-ferritin in hepatoma: a model for radioimmunoglobulin dosimetry. Int. J. Radiat. Oncol. Biol. Phys. 7, 323–333.

Ljungberg, M., King, M.A., Hademenos, G.J., Strand, S.E., 1994. Comparison of four scatter correction methods using Monte Carlo simulated source distributions. J. Nucl. Med. 35, 143–151.

Ljungberg, M., Msaki, P., Strand, S.E., 1990. Comparison of dual-window and convolution scatter correction techniques using the Monte Carlo method. Phys. Med. Biol. 35, 1099.

Ljungberg, M., Strand, S.E., 1991. Attenuation and scatter correction in SPECT for sources in a nonhomogeneous object: a monte Carlo study. J. Nucl. Med. 32, 1278–1284.

Ljungberg, M., Strand, S.E., 1989. A Monte Carlo program for the simulation of scintillation camera characteristics. Comput. Methods Programs Biomed. 29, 257–272.

Ljungberg, M., Strand, S.E., King, M.A., 1998. THE SIMSET PROGRAME. In: "*Monte Carlo Calculations in Nuclear Medicine: Applications in diagnostic imaging*". 2nd edition, CRC Press, USA. pp87–110

Luo, J.Q., Koral, K.F., Ljungberg, M., Floyd, C.E., Jr, Jaszczak, R.J., 1995. A Monte Carlo investigation of dual-energy-window scatter correction for volume-of-interest quantification in ^{99m}Tc SPECT. Phys. Med. Biol. 40, 181–199.

Macey, D.J., DeNardo, G.L., DeNardo, S.J., 1999. Planar gamma camera quantitation of ^{123}I, ^{99m}Tc or ^{111}In in the liver and spleen of an abdominal phantom. Cancer Biother. Radiopharm. 14, 299–306.

Macey, D.J., DeNardo, G.L., DeNardo, S.J., Hines, H.H., 1986. Comparison of low- and medium-energy collimators for SPECT imaging with iodine-123-labeled antibodies. J. Nucl. Med. 27, 1467–1474.

Macey, D.J., Grant, E.J., Bayouth, J.E., Giap, H.B., Danna, S.J., Sirisriro, R., Podoloff, D.A., 1995. Improved conjugate view quantitation of I-131 by subtraction of scatter and septal penetration events with a triple energy window method. Med. Phys. 22, 1637–1643.

Maes, F., Collignon, A., Vandermeulen, D., Marchal, G., Suetens, P., 1997. Multimodality image registration by maximization of mutual information. IEEE Trans. Med. Imaging 16, 187–198.

Meikle, S.R., Hutton, B.F., Bailey, D.L., 1994. A transmission-dependent method for scatter correction in SPECT. J. Nucl. Med. 35, 360–367.

Minarik, D., Ljungberg, M., Segars, P., Gleisner, K.S., 2009. Evaluation of quantitative planar ^{90}Y bremsstrahlung whole-body imaging. Phys. Med. Biol. 54, 5873–5883.

Minarik, D., Sjögreen, K., Ljungberg, M., 2005. A new method to obtain transmission images for planar whole-body activity quantification. Cancer Biother. Radiopharm. 20, 72–76.

Msaki, P., Axelsson, B., Dahl, C.M., Larsson, S.A., 1987. Generalized scatter correction method in SPECT using point scatter distribution functions. J. Nucl. Med. 28, 1861–1869.

Murphy, P.H., 1987. Acceptance testing and quality control of gamma cameras, including SPECT. J. Nucl. Med. 28, 1221–1227.

Narita, Y., Eberl, S., Iida, H., Hutton, B.F., Braun, M., Nakamura, T., Bautovich, G., 1996. Monte Carlo and experimental evaluation of accuracy and noise properties of two scatter correction methods for SPECT. Phys. Med. Biol. 41, 2481.

National Electrical Manufacturers Association, 2007. NEMA NU 1 Perfomance Measurements of Gamma Cameras.

Naudé, H., van Aswegen, A., Herbst, C.P., Lötter, M.G., Pretorius, P.H., 1996. A Monte Carlo evaluation of the channel ratio scatter correction method. Phys. Med. Biol. 41, 1059–1066.

Norrgren, K., Svegborn, S.L., Areberg, J., Mattsson, S., 2003. Accuracy of the quantification of organ activity from planar gamma camera images. Cancer Biother. Radiopharm. 18, 125–131.

Ogawa, K., 1994. Simulation study of triple-energy-window scatter correction in combined Tl-201, Tc-99m SPECT. Ann. Nucl. Med. 8, 277–281.

Ogawa, K., Harata, Y., Ichihara, T., Kubo, A., Hashimoto, S., 1991. A practical method for position-dependent Compton-scatter correction in single photon emission CT. IEEE Trans. Med. Imaging 10, 408–412.

Oropesa, P., Hernández, A.T., Serra, R., Varela, C., 2005. Comparisons of activity measurements with radionuclide calibrators—A tool for quality assessment and improvement in nuclear medicine. Appl. Radiat. Isot. 63, 493–503.

Pereira, J.M., Stabin, M.G., Lima, F.R.A., Guimarães, M.I.C.C., Forrester, J.W., 2010. Image quantification for radiation dose calculations--limitations and uncertainties. Health Phys. 99, 688–701.

Pretorius, P.H., van Rensburg, A.J., van Aswegen, A., Lötter, M.G., Serfontein, D.E., Herbst, C.P., 1993. The channel ratio method of scatter correction for radionuclide image quantitation. J. Nucl. Med. 34, 330–335.

Rajeevan, N., Zubal, I.G., Ramsby, S.Q., Zoghbi, S.S., Seibyl, J., Innis, R.B., 1998. Significance of nonuniform attenuation correction in quantitative brain SPECT imaging. J. Nucl. Med. 39, 1719–1726.

Roelants, V., Bernard, X., Walrand, S., Bol, A., Coppens, A., Jamart, J., Melin, J., Vanoverschelde, J.L., 2006. Attenuation-corrected ^{99m}Tc-MIBI SPECT in overweight patients with chronic ischaemic dysfunction: a comparison to NH3 PET and implications for the diagnosis of myocardial viability. Nucl. Med. Commun. 27, 815–821.

Saha, G.B., 2012. PERFORMANCE PARAMETERS OF GAMMA CAMERAS. In: "*Physics and Radiobiology of Nuclear Medicine*". 4th edition, Springer, USA. pp139–150

Shidahara, M., Watabe, H., Kim, K.M., Kato, T., Kawatsu, S., Kato, R., Yoshimura, K., Iida, H., Ito, K., 2005. Development of a practical image-based scatter correction method for brain perfusion SPECT: comparison with the TEW method. Eur. J. Nucl. Med. Mol. Imaging 32, 1193–1198.

Shih, W.J., Schoenstra, T., Gross, K., Wierzbinski, B., Kiefer, V., Collins, J., 2003. Electronic Off-Peak Status of One Head of a Dual-Head Gamma Camera Resulted in Bone Scintigraphy Artifacts and Faulty Findings on Gated Myocardial SPECT. J. Nucl. Med. Technol. 31, 165–169.

Siegel, J.A., Thomas, S.R., Stubbs, J.B., Stabin, M.G., Hays, M.T., Koral, K.F., Robertson, J.S., Howell, R.W., Wessels, B.W., Fisher, D.R., Weber, D.A., Brill, A.B., 1999. MIRD pamphlet no. 16: Techniques for quantitative radiopharmaceutical biodistribution data acquisition and analysis for use in human radiation dose estimates. J. Nucl. Med. 40, 37S–61S.

Sjögreen, K., Ljungberg, M., Strand, S.E., 2002. An activity quantification method based on registration of CT and whole-body scintillation camera images, with application to ^{131}I. J. Nucl. Med. 43, 972–982.

Sjögreen, K., Ljungberg, M., Wingårdh, K., Minarik, D., Strand, S.E., 2005. The LundADose method for planar image activity quantification and absorbed-dose assessment in radionuclide therapy. Cancer Biother. Radiopharm. 20, 92–97.

Soret, M., Bacharach, S.L., Buvat, I., 2007. Partial-volume effect in PET tumor imaging. J. Nucl. Med. 48, 932–945.

Studholme, C., Hill, D.L., Hawkes, D.J., 1996. Automated 3-D registration of MR and CT images of the head. Med. Image Anal. 1, 163–175.

Thomas, M.D.R., Bailey, D.L., Livieratos, L., 2005. A dual modality approach to quantitative quality control in emission tomography. Phys. Med. Biol. 50, N187–N194.

Thomas, S.R., Maxon, H.R., Kereiakes, J.G., 1976. In vivo quantitation of lesion radioactivity using external counting methods. Med. Phys. 3, 253–255.

Tothill, P., 1974. Limitations of the use of the geometric mean to obtain depth independence in scanning and whole body counting. Phys. Med. Biol. 19, 382.

Van Rensburg, A.J., Lötter, M.G., Heyns, A.P., Minnaar, P.C., 1988. An evaluation of four methods of ^{111}In planar image quantification. Med. Phys. 15, 853–861.

Van Staden, J.A., du Raan, H., Lötter, M.G., Herbst, C.P., van Aswegen, A., Rae, W.I.D., 2011. Evaluation of an uncollimated printed paper transmission source used under scatter limiting conditions. Phys. Medica PM Int. J. Devoted Appl. Phys. Med. Biol. 27, 11–20.

Van Staden, J.A., du Raan, H., Lötter, M.G., van Aswegen, A., Herbst, C.P., 2007. Production of radioactive quality assurance phantoms using a standard inkjet printer. Phys. Med. Biol. 52, N329–337.

Velidaki, A., Perisinakis, K., Koukouraki, S., Koutsikos, J., Vardas, P., Karkavitsas, N., 2007. Clinical usefulness of attenuation and scatter correction in Tl-201 SPECT studies using coronary angiography as a reference. Hell. J. Cardiol. 48, 211–217.

Wells, W.M., Viola, P., Atsumi, H., Nakajima, S., Kikinis, R., 1996. Multi-modal volume registration by maximization of mutual information. Med. Image Anal. 1, 35–51.

Willowson, K., Bailey, D.L., Baldock, C., 2008. Quantitative SPECT reconstruction using CT-derived corrections. Phys. Med. Biol. 53, 3099–3112.

Wu, R.K., Siegel, J.A., 1984. Absolute quantitation of radioactivity using the buildup factor. Med. Phys. 11, 189–192.

Yang, J.T., Yamamoto, K., Sadato, N., Tsuchida, T., Takahashi, N., Hayashi, N., Yonekura, Y., Ishii, Y., 1997. Clinical value of triple-energy window scatter correction in simultaneous dual-isotope single-photon emission tomography with ^{123}I-BMIPP and ^{201}Tl. Eur. J. Nucl. Med. 24, 1099–1106.

Zaidi, H., 1996. Comparative methods for quantifying thyroid volume using planar imaging and SPECT. J. Nucl. Med. 37, 1421–1426.

Zaidi, H., Koral, KF., 2005. METHODS FOR PLANAR IMAGE QUANTIFICATION. In: "*Quantitative analysis in nuclear medicine imaging"*. New York: Kluwer Academic/Plenum Publishers, USA. pp 414–431.

Zaidi, H., Koral, K.F., 2004. Scatter modelling and compensation in emission tomography. Eur. J. Nucl. Med. Mol. Imaging. 31, 761–782.

Zanzonico, P., 2008. Routine Quality Control of Clinical Nuclear Medicine Instrumentation: A Brief Review. J. Nucl. Med. 49, 1114–1131.

Zeintl, J., Vija, A.H., Yahil, A., Hornegger, J., Kuwert, T., 2010. Quantitative accuracy of clinical 99mTc SPECT/CT using ordered-subset expectation maximization with 3-dimensional resolution recovery, attenuation, and scatter correction. J. Nucl. Med. 51, 921–928.

3. TECHNETIUM-99m ACTIVITY QUANTIFICATION.

3.1 Introduction.

The aim of this section of the research project was to quantify tumour insert activity distribution using ^{99m}Tc to achieve the objectives mentioned in Chapter 1 (Section 1.5). ^{99m}Tc is widely used in nuclear medicine for diagnostic procedures due to its favourable imaging characteristics. These include: favourable γ-ray energy for imaging with a gamma camera, its affinity for labelling a wide range of pharmaceuticals and a relatively short half life of 6.02 hours, adequate for imaging while keeping patient radiation dose low. ^{99m}Tc emits a γ-ray with energy of 140 keV and a yield of 89 %. Its supply is dependent on its parent radionuclide molybdenum-99 (^{99}Mo). ^{99m}Tc is supplied through a ^{99}Mo-^{99m}Tc generator and is chemically extracted, from an alumina column containing ^{99}Mo, using sterile saline. ^{99}Mo-^{99m}Tc generators, in the Department of Nuclear Medicine at Universitas Hospital, are supplied by Nuclear Technology Products (NTP), a subsidiary of South Africa Nuclear Energy Corporation (NECSA). NTP is one of only a few ^{99}Mo processing facilities in the world. ^{99m}Tc, obtained from ^{99}Mo-^{99m}Tc generators, is readily available at relatively low cost in comparison to other radionuclides used in diagnostic imaging such as ^{123}I. Different ^{99m}Tc labelled pharmaceutical kits are widely used for clinical applications such as myocardial perfusion and whole body skeletal imaging.

The aim of accurate activity quantification is to ultimately obtain accurate dose calculations for dosimetry purposes (Sjögreen et al., 2005). In this research project tumour quantification was performed using an abdominal phantom equipped with tumour and liver inserts (discussed in Section 3.2.2.1). Tumour activity quantification was performed for a range of geometries, as depicted in Chapter 1 (Section 1.5). The tumours were filled with a known amount of radioactivity that was initially measured in the dose calibrator. The activity measured in the dose calibrator served as a reference for determining the accuracy of the tumour quantification. This was followed by phantom acquisitions using the gamma camera. Regions of interest (ROIs), defining the tumour activity distribution, were used to obtain image counts. Scatter correction was performed on the image counts, using the modified triple energy window (TEW_2) scatter correction technique, and the geometric mean (GM) of counts obtained, based on the theory mentioned in Chapter 2 (Section 2.3.1). Attenuation correction was performed using attenuation correction factors (ACFs). These were calculated from transmission images obtained using an uncollimated ^{99m}Tc printed transmission source. A system calibration factor (SCF), processed in the same manner as the tumour quantified

data, was used to convert the image counts, obtained from the tumour ROI, to units of radioactivity. Spill-out effects, due to partial volume effects (PVE) owing to the limited spatial resolution of the gamma camera, were accounted for by the manner in which ROIs for tumour activity distribution were defined. The influence of background activity on tumour activity quantification accuracy was investigated for two different tumour-background ratios. A summary of the data processing techniques for tumour activity quantification is shown in Figure 3-1 and discussed in detail in Section 3.2.4.

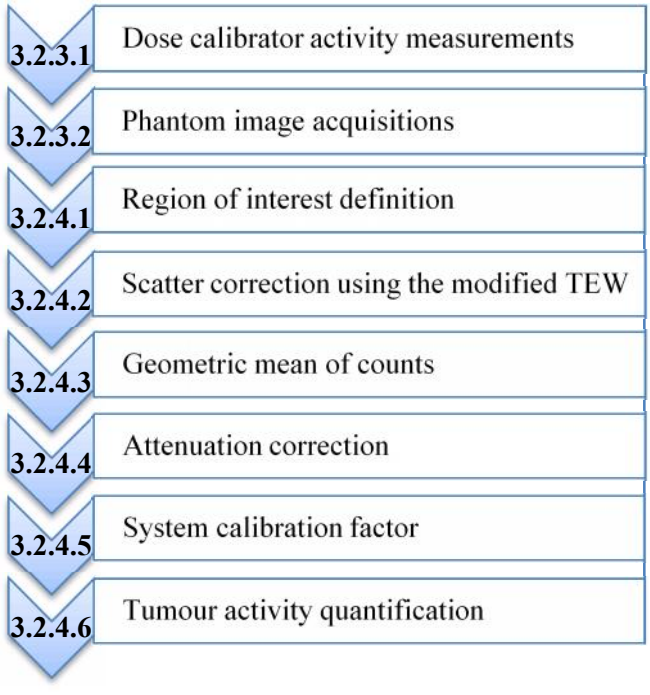

Figure 3-1: *Flow chart indicating data processing techniques used for ^{99m}Tc activity quantification of planar tumour images.*

3.2 Materials and Methods.

3.2.1 Equipment stability.

In order to obtain reliable quantitative results and minimize systematic errors due to faulty equipment, equipment stability should be considered. This is an important consideration as it will affect the reproducibility and integrity of the obtained results and ultimately the accuracy and precision achieved. A measure of equipment stability was obtained by measurement of some performance characteristics of the dose calibrator and gamma camera used in the quantification process of the research project.

3.2.1.1 Dose calibrator performance characteristics.

As mentioned in Chapter 2, Section 2.2.1, a calibrated source is used to determine the accuracy of the dose calibrator. The reproducibility of this accuracy is ascertained by performing daily checks using a long lived radioactive source. These two tests were performed to determine the accuracy and the reproducibility of the dose calibrator used in this research project.

a) Dose calibrator accuracy.

As mentioned above, image quantification accuracy was calculated with reference to activity measurements in the dose calibrator. The performance of the dose calibrator was evaluated as part of a research project entitled "Intercomparison of Nuclear Medicine isotope calibrators in the Bloemfontein Area". In this project the accuracy of seven dose calibrators in different nuclear medicine clinics in Bloemfontein was determined. This was done using standard solutions of four radionuclides routinely used in clinical practice namely; ^{99m}Tc, ^{123}I, ^{67}Ga and ^{131}I. These radionuclides were placed in flame sealed ampoules. The samples were measured in the dose calibrators and background corrections applied. The radionuclides were sent to National Metrology Institute of South Africa (NMISA) in Cape Town for traceability. The percentage difference between the measurement made by NMISA and that obtained using the Capintec CRC-15R dose calibrator in the Department of Nuclear Medicine at Universitas Hospital for ^{99m}Tc is reported.

b) Dose calibrator reproducibility.

The reproducibility of the dose calibrator was checked on the ^{99m}Tc radionuclide setting using a standard ^{137}Cs radioactive source. The background reading of the dose calibrator was set to zero before the measurements were performed. All readings were given time to stabilize, and the measured apparent activity was recorded. This procedure was repeated daily for a period of ten months (December 2012 – September 2013). The average apparent activity value and standard deviation are reported.

3.2.1.2 Gamma camera quality control.

All measurements for this research project were performed on the Symbia T SPECT/CT gamma camera (Siemens Medical Solutions USA, Inc) in the Department of Nuclear Medicine at Universitas Hospital shown in Figure 3-2. Image acquisitions for ^{99m}Tc were

performed using the low energy high resolution (LEHR) collimator. The Symbia T has a crystal thickness of 9.5 mm, an energy resolution of 9.9 % for ^{99m}Tc and a system spatial resolution of 7.7 mm full width half maximum (FWHM) for the LEHR collimator measured at 10 cm. The gamma camera was peaked daily using a ^{99m}Tc point source (count rate of < 40 k counts per second (kcps))

Figure 3-2: *All measurements were performed on the Symbia T SPECT/CT (Siemens Medical Solutions USA, Inc.).*

a) Intrinsic flood field uniformity.

The intrinsic flood field uniformity, acquired on a weekly basis for quality control purposes, was assessed to ensure the stability of the Symbia T during the time period that measurements were conducted for this research project. An intrinsic flood field uniformity image was acquired and processed according to the National Electrical Manufacturers Association (NEMA) recommendations (NEMA, 2007). The results of the average integral uniformity (IU) and differential uniformity (DU) for the useful field of view (UFOV) and central field of view (CFOV), measured over a period of nine months, for both detectors of the Symbia T are reported.

b) Intrinsic count rate performance.

The intrinsic count rate performance was evaluated according to NEMA as part of the yearly quality control tests on the Symbia T during the time period of measurements carried out for this research project (NEMA, 2007). Results from these measurements were used to ascertain the accuracy of the count rate performance for the Symbia T. This test was performed with the attenuation source method using copper plates (Geldenhuys et al., 1988). The Symbia T dead time model was expressed as a plot of the observed count rate versus the

true count rate from which a graph was created to determine the percentage count loss for a specified observed count rate. The maximum count rate and observed count rate at 20 % count loss, calculated according to the NEMA recommendations, are reported. The percentage count loss at count rates observed during acquisitions for the phantom studies was noted.

3.2.2 Phantom description.

3.2.2.1 Polyvinyl chloride abdominal phantom.

Measurements for tumour activity quantification were performed using an in-house manufactured abdominal phantom (Figure 3-3). This phantom was developed by the instrumentation workshop at the University of the Free State. Polyvinyl Chloride (PVC) was used to construct the outer shell of the phantom as well as a solid rod, at the base of the phantom, to simulate the spine. For this reason the phantom will be termed the PVC phantom. PVC was used due to its wide application, availability and low cost. PVC was cheaper and more manageable than the commonly used Perspex, and is used by the workshop to support various departments at the University of the Free State. The PVC phantom holds a volume of approximately 16 000 cm^3, with the inserts in place, and has a diameter and length of 31 cm. It has an inlet and outlet for filling and draining of the liver. The base of the phantom is supported by two base plates for sturdiness and rigid reproducible positioning of the phantom at marked positions on the gamma camera bed, during repeated acquisitions as shown in Figure 3-3(a). Linear attenuation maps, measured with the CT scanner (of the Symbia T) scaled to the energy of ^{99m}Tc, for the PVC phantom and a patient, were compared in the area of the spinal column.

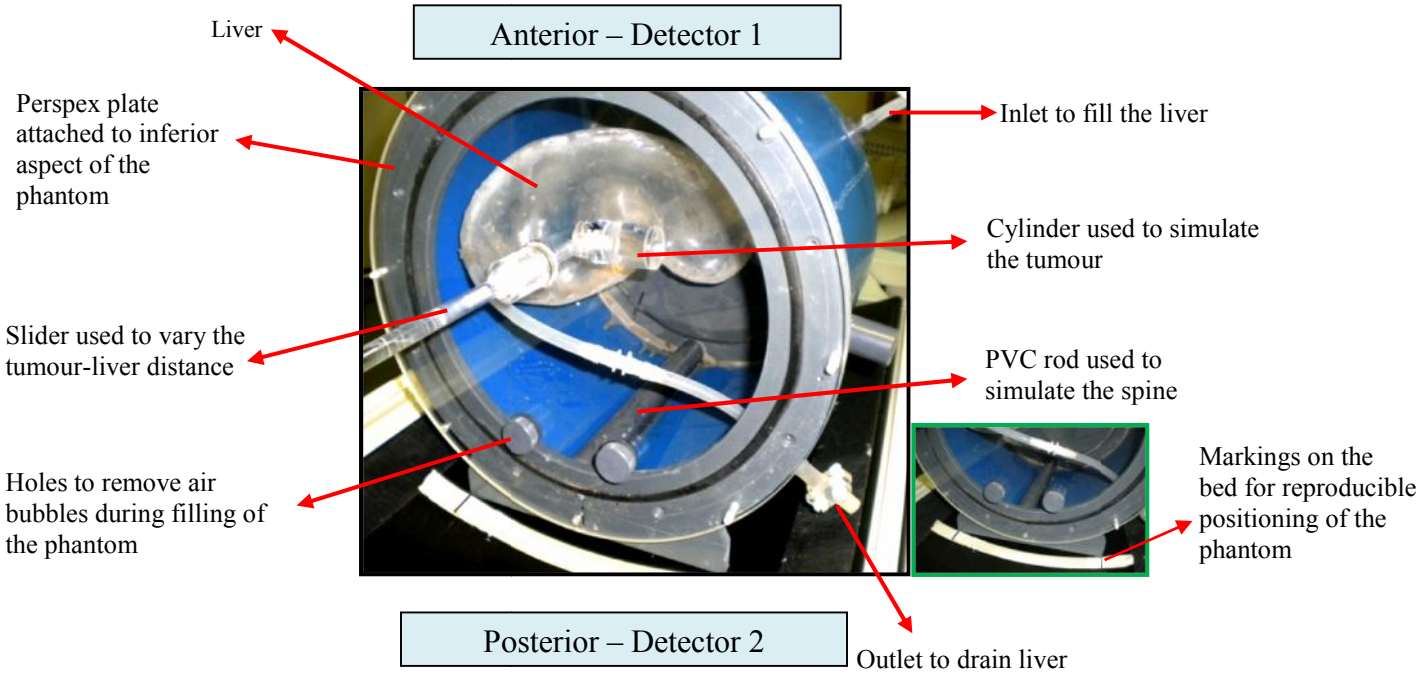

a)

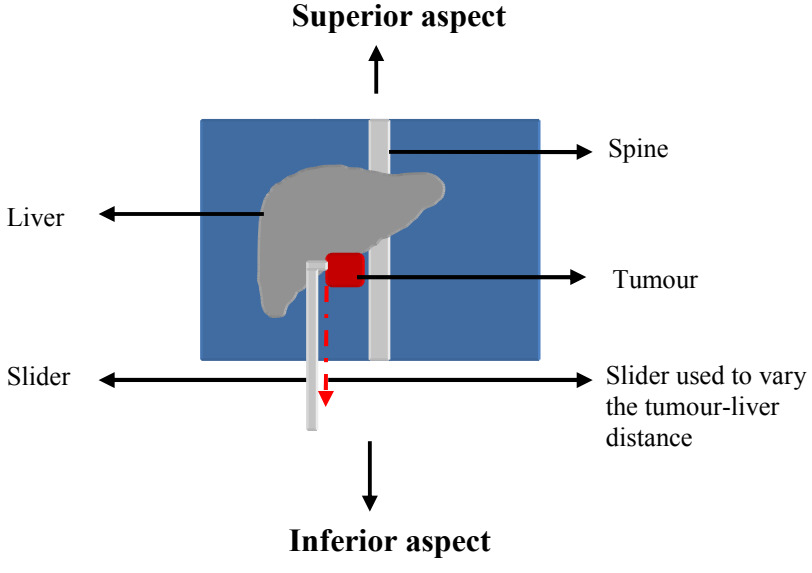

b)

Figure 3-3: *(a) A photograph of the PVC phantom placed in the head-in position for acquisitions (b) illustration of the anterior view of the PVC phantom as seen from detector 1.*

PVC constituted only the outer surface of the phantom, therefore most of the physical characteristics associated with emission imaging (scatter and attenuation) will be due to the water contained in the phantom. The different densities of PVC, water and Perspex simulated the heterogeneity obtained in clinical acquisitions of patient studies. The design of the phantom was based on the geometry encountered for clinical studies of [^{123}I]-MIBG diagnostic predictive scans, as shown in Chapter 1 (Section 1.5). The phantom was equipped with Perspex inserts for the liver and different sized cylinders to imitate tumours (Figure 3-4).

These tumours were attached on a slider to enable the user to vary the tumour-liver distance (Figure 3-3(b)).

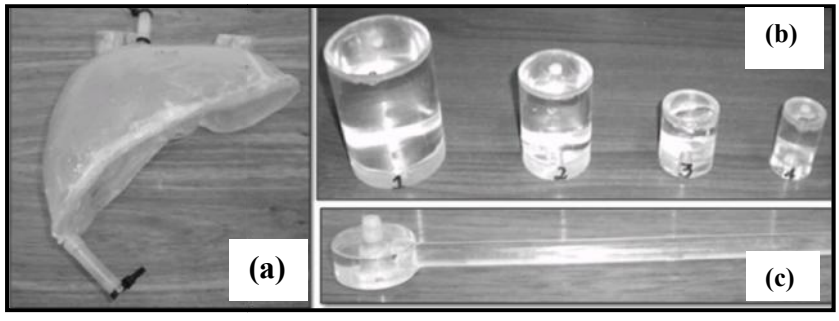

Figure 3-4: *(a) Perspex liver insert, (b) cylinders of different sizes to imitate tumours and (c) the slider used to vary the tumour-liver distance*.

The liver insert had a volume of approximately 1200 cm^3 including small volumes contained in the pipes for filling and drainage. A Perspex plate, attached by Perspex screws, to the inferior aspect of the phantom made it transparent for visual inspection and ease of water drainage and filling from the PVC shell. The slider was attached to the Perspex plate with an O-ring to prevent leakage during the sliding movement. Two holes were drilled into the Perspex plate for removal of air bubbles during filling of the phantom.

Although spheres are more commonly used to represent tumours in phantoms as they are thought to represent clinical situations of tumour images (Ng et al., 2009), cylindrical tumour inserts were manufactured as it was technically more simple to do so. The availability of Perspex tubes in various diameters made manufacturing of cylinders more economical and swift. Cylinders have been successfully used in nuclear medicine for construction of a low cost phantom for quality control of SPECT gamma cameras (Perkins et al., 2007). An advantage of the cylinders, from handling point of view, was the ease of filling due to their ability to stand on their flat base. The diameters of the four cylinders were 63 mm, 45 mm, 34 mm and 23 mm, based on the available rod diameter sizes, and will be termed Tumour I to IV respectively (Figure 3-5). The walls of the tumours had a thickness of 3 mm which was assumed to have negligible effects on attenuation.

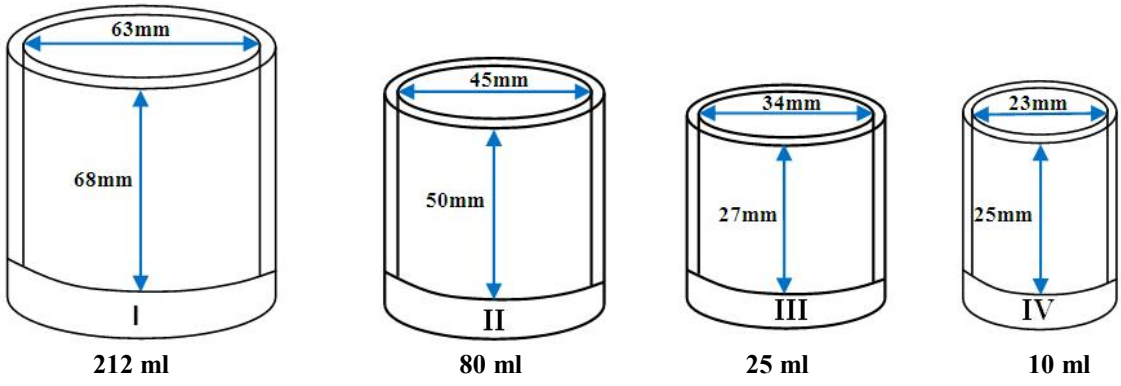

Figure 3-5: *Schematic representation of the four different size cylinders used to represent tumours, termed Tumour I to IV in order of decreasing size.*

3.2.2.2 Uniform water bath phantom.

A uniform water bath phantom was used to measure linear attenuation coefficients for ^{99m}Tc (discussed in Section 3.2.4.4.3). The rectangular water bath phantom had a width and height of 30 cm (Figure 3-6). Attenuation coefficients were determined from transmission images obtained with the water filled phantom, acquired under both broad beam and narrow beam conditions.

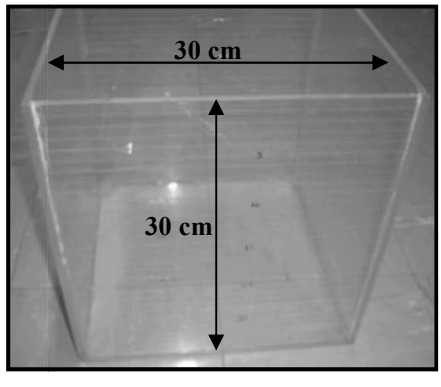

Figure 3-6: *Uniform water bath phantom used for measurements of linear attenuation coefficients.*

3.2.2.3 Perspex phantom.

Sixteen individual slabs of Perspex with a total thickness of 17.3 cm were used for measurements of the SCF, as well as the linear attenuation coefficient of ^{99m}Tc for Perspex (Figure 3-7). The SCF was measured by placing a printed radioactive disk between the slabs of Perspex, discussed in Section 3.2.4.5. Linear attenuation coefficients were determined

from transmission images of the Perspex slabs acquired under broad beam and narrow beam conditions, discussed in Section 3.2.4.4.3.

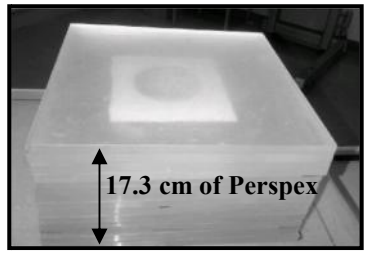

Figure 3-7: *Perspex slabs used to measure system calibration factors and linear attenuation coefficients.*

3.2.3 Data acquisition.

3.2.3.1 Phantom preparation.

All data acquisitions, for each day of measurement, commenced with radioactivity measurements in the dose calibrator mentioned in Section 3.2.1.1. Background measurements on the dose calibrator were set to zero. A syringe, containing radioactivity to be injected into the tumours, was measured and the time of measurement recorded. The radioactivity was injected into the water filled tumour and the residual radioactivity in the syringe was subtracted from the initial measurement, to obtain the actual amount of radioactivity contained in the water filled tumour. The removal of all air bubbles from the tumour and proper mixing of the radioactive water solution ensured a uniform distribution of radioactivity in the tumour. The radioactivity measured in the dose calibrator, as described above, was used as reference for the accuracy achieved from the quantified activity distribution of the tumour images and is termed measured activity.

The liver was filled from a large volume of known ^{99m}Tc concentration. ^{99m}Tc was measured with the dose calibrator and mixed with 2000 cm^3 of water. Radioactivity concentrations used for the tumours were based on clinical uptake assessed from clinical whole body images of [^{123}I]-MIBG for neuroendocrine tumour investigation (Chapter 1, Figure 1-1). A large variation, in [^{123}I]-MIBG uptake and tumour-liver ratios, was observed from these images between patients and for the different imaging time points. The radioactivity injected into the tumours was based on fractional percentage uptake of the tumours relative to whole body activity. These calculations were done by using the total activity injected which varied from 185 MBq to 370 MBq according to a clinical protocol established in the department based on

international guidelines and literature (Bombardieri et al., 2003; Fielding et al., 1991; Olivier et al., 2003). Commonly, tumour uptake of 10 % was observed from most of the clinical ^{123}I-[MIBG] images. For this reason, tumour activities of 37 MBq, 35 MBq, 18.5 MBq and 12 MBq for Tumours I to IV respectively were used. These radioactive concentrations represented clinical uptake. It must be noted that the concentrations amongst the tumours varied, which was representative of the large variation of the tumour-liver ratios observed in clinical situations. The tumour-liver ratios used were 2:1, 5:1, 10:1 and 15:1 for Tumour I to IV respectively. These ratios were in accordance with some reported ratios in literature used for sphere quantification in torso phantoms based on clinical protocols for ^{99m}Tc, ^{131}I and ^{111}In (Pereira et al., 2010). The different size tumours were placed one at a time into the PVC phantom. The liver was filled with its radioactive concentration using a pump and the rest of the PVC phantom was manually filled with water.

Two different tumour-background ratios were investigated in this study. Acquisitions were performed using these two different levels of background activity, utilizing only Tumour II. Background radioactivity placed into the PVC phantom was 0.5 % and 1.0 % of Tumour II radioactivity concentration.

3.2.3.2 Acquisition protocol.

All acquisitions commenced with room background acquisitions, acquired using the same protocol as that used for phantom measurements (described below). Room background images were acquired to asses any factors that may elevate the room background. These include: detector contamination, background from radiation sources that might be present in the gamma camera room and stray radiation from patients in hallways.

After preparation of the PVC phantom, as described in Section 3.2.3.1, the phantom was placed on the markings of the bed in a head-in position (shown in Figure 3-3(a)). The slider (with a tumour attached) was pushed into the phantom until the tumour was in contact with the liver. This was marked as the 0 cm tumour-liver distance for a specific tumour. This position was noted, and used for all repeat measurements. A 180° detector configuration, with detector one and two positioned anterior and posterior of the phantom respectively, was used for all the acquisitions. The detector phantom distance was 1 cm and 7 cm for detectors one and two respectively. The slider distance was later displaced in increments of 3 cm offsets by pulling the slider in an outward direction from the phantom to achieve tumour-liver

distances of 3 cm and 6 cm. It must be noted that the same radial level between the liver and the tumour in the y-direction was maintained, which was achieved by using a sliding movement in the z-direction (axial direction) (Figure 3-8).

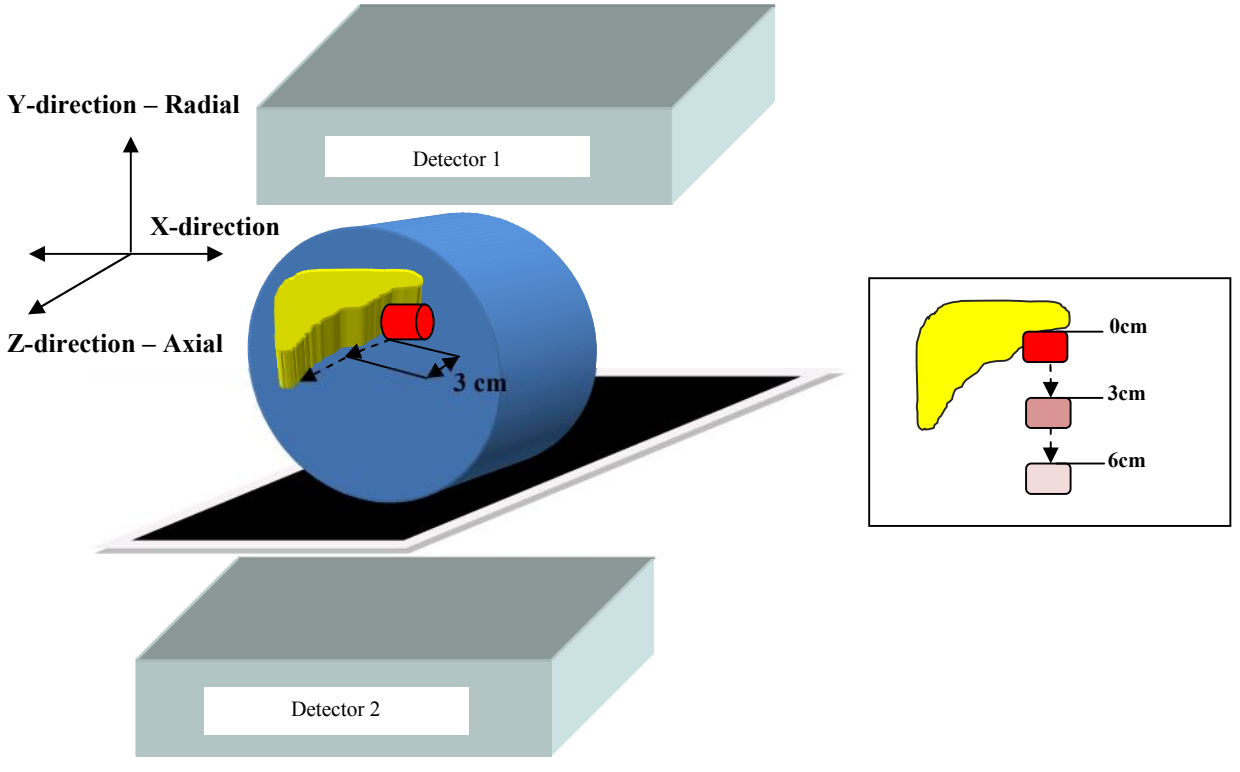

(a) *(b)*

Figure 3-8: *(a) Schematic representation of experimental setup used to evaluate the effect of varying tumour-liver distance in 3 cm offsets. (b) Anterior view as seen from detector 1 with tumour movement along Z-direction in 3cm increments, with 0cm being periphery (not the centre) of the tumour.*

Measurements for all four tumours were performed in the same manner on different days of measurements and all acquisitions were repeated three times on different days. Acquisitions with background activity, for various tumour-background ratios, were performed in the same manner. As mentioned in Section 3.2.3.1, this was only done for Tumour II, for tumour-liver distances of 0 cm and 6 cm. Similarly measurements were repeated three times on different days.

Since the objective of this project was to evaluate the effect of varying geometry on quantification accuracy using protocols as recommended by the manufacturer (Syngo MI Applications 2007A; Siemens Healthcare), standard clinical acquisition protocols were used

with no modifications or optimisation. Planar images of the PVC phantom were acquired for 15 minutes in a 256 × 256 word image matrix with a pixel size of 2.4 mm. The modified TEW scatter correction technique was used for the acquisitions with window widths set to 15 % of the photopeak energy. The selected lower scatter sub-window was 107.7 – 128.5 keV and the selected photopeak window was 128.5 – 149.3 keV with a scatter weighting factor of 0.5. Both the photopeak window and lower sub-window had widths of 21 keV. All PVC phantom emission acquisitions were acquired with an observed count rate of ≤ 5 kcps.

3.2.4 Data processing.

The steps shown in Figure 3-1 used to process the tumour planar images for activity quantification, acquired as described in the preceding section, were in accordance with the theoretical concept shown in Equation 3.1. The tumour activity measured in the dose calibrator was used as reference in the determination of activity quantification accuracy. Parameters for data processing according to Equation 3.1 will be discussed in the subsequent sections.

$$Quantified\ Activity\,(MBq) = \frac{\frac{\sqrt{C_A \times C_P}}{t} \times ACF_{BB\_^{99m}Tc\_water} \times Wk_1}{\frac{\sqrt{C_{AP} \times C_{PP}}}{A \times t} \times ACF_{BB\_^{99m}Tc\_Perspex} \times Pk_1} \qquad \textbf{3. 1}$$

where:

- C_A and C_P are the anterior and posterior primary counts obtained from the ROI defining the tumour radioactivity distributions. The primary counts were calculated using the counts recorded in the photopeak window corrected for decay, room background and scatter.
- t is the acquisition time which was kept constant at 15 minutes for all acquisitions.
- A is the radioactivity of the printed radioactive disk as measured in the dose calibrator.
- $ACF_{BB\_^{99m}Tc\_water}$ and $ACF_{BB\_^{99m}Tc\_Perspex}$ are the ACF measured under broad beam conditions (modified for minimal scatter inclusion) for water and Perspex measurements respectively, discussed in Section 3.2.4.4.

- $Wk_1 = \frac{\mu_{NB\_^{99m}Tc\_water}}{\mu_{BB\_^{99m}Tc\_water}}$ $\quad Pk_1 = \frac{\mu_{NB\_^{99m}Tc\_Perspex}}{\mu_{BB\_^{99m}Tc\_Perspex}}$

where: Wk_1 and Pk_1 are the scaling factors for water and Perspex measurements respectively, used to account for the fact that transmission measurements, for attenuation correction, were not acquired under ideal narrow beam conditions, discussed in Section 3.2.4.4.3.

- $\mu_{BB\_^{99m}Tc\_Perspex}$ and $\mu_{BB\_^{99m}Tc\_water}$ are the linear attenuation coefficients of ^{99m}Tc measured under broad beam conditions (modified for minimal scatter inclusion) for Perspex and water respectively.
- $\mu_{NB\_^{99m}Tc\_Perspex}$ and $\mu_{NB\_^{99m}Tc\_water}$ are the linear attenuation coefficients of ^{99m}Tc measured under narrow beam conditions for Perspex and water respectively.
- The denominator shown in Equation 3.1 represents the SCF, measured with a printed radioactive disk in-between Perspex (mentioned in Section 3.2.2.3), and used to convert counts to units of activity. C_{AP} and C_{PP} are the anterior and posterior primary counts of the SCF obtained, from the ROI defining the printed disk radioactivity distribution, discussed in Section 3.2.4.5. The primary counts were calculated using the counts recorded in the photopeak window corrected for decay, room background and scatter.

It can be seen from Equation 3.1 that the corrections applied for quantification are built into the SCF. This was owing to the imaging geometry (Perspex as attenuating material) used to obtain the SCF. It was important that the same processing techniques applied in the tumour quantification process were also applied to the SCF.

3.2.4.1 Region of interest definition.

ROIs were manually drawn according to the known dimensions of the inner diameters of each tumour, shown in Figure 3-5. This method offered a standard, reproducible criterion for ROI definition. Each tumour image was fitted with a rectangle, which represented the tumour regions in the anterior and posterior views. A conversion factor of 2.4 mm/pixel for the 256 × 256 image matrix was used to determine the number of pixels to be included in each ROI for the various tumour dimensions. ROIs used for Tumour I to IV included 744, 391, 160 and 99 pixels respectively (Figure 3-9). Defining the ROIs in this manner did not take into account PVE due to the limited spatial resolution and modulation of the gamma camera. This method of ROI definition was equivalent to using the CT-scout image to draw

ROIs on planar images for activity quantification (Minarik et al., 2005; Sjögreen et al., 2005). These ROIs were saved and used for repeated measurements.

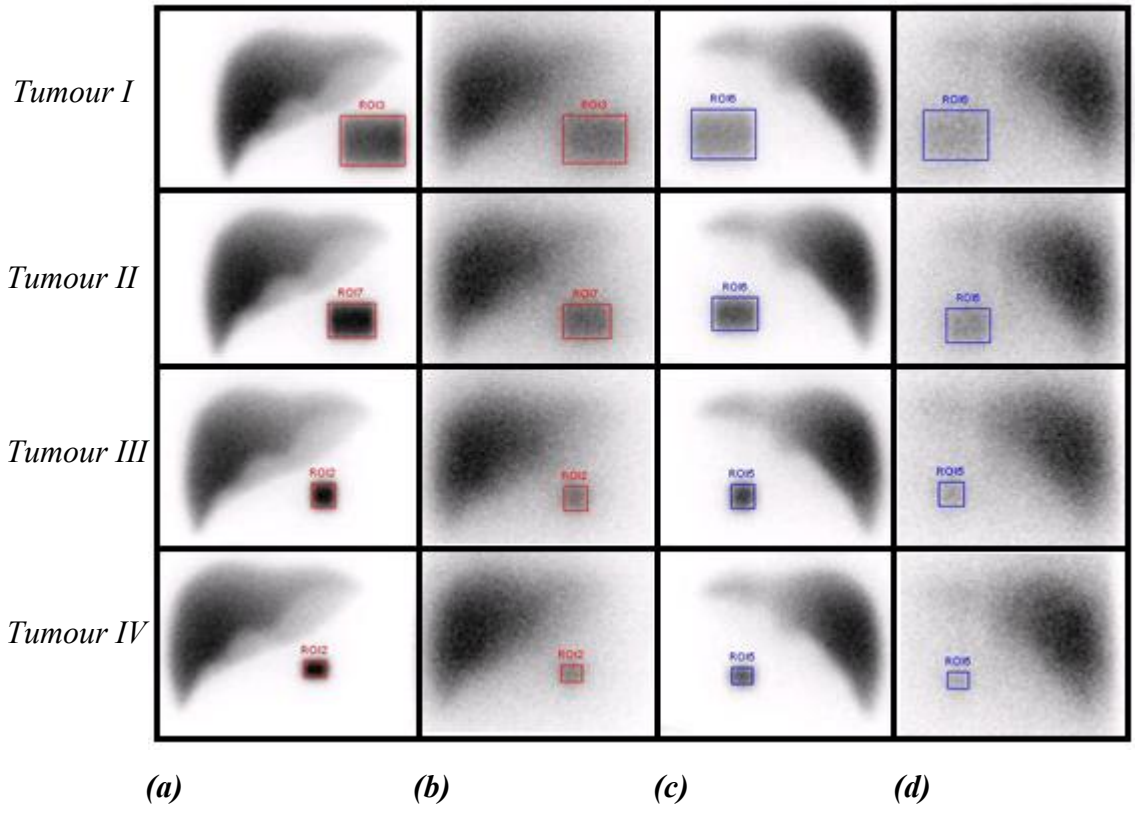

Figure 3-9: *Examples of regions of interest used for quantification of Tumour I to IV shown in top to bottom rows respectively, measured at a tumour-liver distances of 3 cm. Anterior images recorded in the (a) photopeak (b) scatter sub-window and posterior images recorded in the (c) photopeak (d) scatter sub-window.*

Acquisitions using the modified TEW scatter correction technique resulted in simultaneous acquisition of images in the scatter and photopeak windows. ROIs described above were used to obtain counts in images of both the scatter and photopeak windows. The total counts recorded in the photopeak window consisted of both the primary and scatter counts. The percentage uncertainty (standard error) for the total counts recorded in the photopeak window for anterior and posterior views, for all tumours is reported. All counts were corrected for decay (to a specific time reference) and room background.

As mentioned in Section 3.2.3.2 room background images were acquired. Saved ROIs of the tumours, were superimposed on the respective detector positions as was set in the PVC phantom during acquisitions. The contribution (percentage) of the room background counts to total counts recorded in the photopeak is reported.

3.2.4.2 Scatter correction using the modified triple energy window.

As mentioned in Chapter 2 (Section 2.3.2.1.2(e)) the employment of a single scatter window adjacent to the photopeak window was the modified method proposed by Ogawa et al., (1991) for scatter correction. The modified TEW scatter correction approach for ^{99m}Tc was similar to the DEW scatter correction technique, since there was no need for an upper window, as the energy spectrum approaches zero and was therefore less susceptible to noise (Ichihara et al., 1993; Ljungberg et al., 1994). This effect, of the energy spectrum approaching zero for ^{99m}Tc, was shown by acquiring the energy spectrum using Tumour I. Scatter correction was applied using the modified TEW scatter correction technique, as specified by the manufacturer (Syngo MI Applications 2007A; Siemens Healthcare) shown in Equation 3.2, prior to GM calculation.

$$C_{TEW\_2} = \left(\frac{C_{lower}}{W_{lower}} \right) \times \frac{W_{photopeak}}{2} \qquad \textbf{3. 2}$$

where: C_{TEW_2} is the scatter count estimate within the photopeak window calculated using the modified TEW scatter correction technique implemented for radionuclides with single energy emissions such as ^{99m}Tc, C_{lower} is the counts recorded in the scatter sub-window located below the photopeak window, W_{lower} and $W_{photopeak}$ are the widths of the scatter and photopeak windows respectively. As mentioned in Section 3.2.3.2 the photopeak and scatter energy windows widths were equivalent therefore Equation 3.2 simplifies to Equation 3.3. Equation 3.3 resembled the method proposed by Jaszczak et al., (1984) and was used to estimate the scatter counts recorded in the photopeak window.

$$C_{TEW\_2} = \frac{(C_{scatter})}{2} \qquad \textbf{3. 3}$$

The primary counts ($C_{primary}$) in the photopeak window were calculated using Equation 3.4.

$$C_{primary} = C_{photopeak} - C_{TEW\_2} \qquad \textbf{3. 4}$$

Equation 3.4 demonstrates how the modified TEW scatter correction technique numerically compensated for counts obtained from γ-rays that have been scattered into the ROI defining the tumours. The modified TEW correction technique results in a reduction of counts recorded in the photopeak window. To demonstrate the amount of scatter contribution for each tumour, an average scatter fraction (SF), expressed as the ratio of the scatter to primary

counts (Kojima et al., 1993), was calculated using Equation 3.5 from data of repeated measurements. The average scatter fraction (expressed as the GM of the anterior and posterior counts) was plotted for each tumour for the tumour-liver distances of 0 cm, 3 cm and 6 cm.

$$SF = \frac{C_{TEW\_2}}{C_{primary}} \qquad \textbf{3. 5}$$

3.2.4.3 Geometric mean.

The GM of the anterior and posterior primary counts, corrected for scatter, was calculated using Equation 3.6. The combination of the anterior and posterior counts in this manner was applied to decrease the variability in counts as detected from the anterior (detector one) and posterior detectors (detector two). The GM of the scatter corrected counts for one set of measurement for Tumour I to IV is reported.

$$GM = \sqrt{C_A \times C_P} \qquad \textbf{3. 6}$$

3.2.4.4 Attenuation correction.

Calculating the GM of counts reduces the depth dependent nature of counts detected from the opposing (anterior and posterior) views. As mentioned in Chapter 2, Section 2.3.1, the GM does not compensate for the effects of attenuation, and the reduction of counts due to attenuation still remains. In order to improve quantification accuracy, attenuation correction has to be performed. Attenuation correction was performed using an uncollimated ^{99m}Tc printed transmission source, as proposed by Van Staden et al., (2007), and for the purpose of this project will be termed an uncollimated printed transmission source. The source was printed using a Hewlett-Packard inkjet printer (HP 1220C) (Figure 3-10). The preparation and the printing of the transmission sources were performed in the hotlab under safe working conditions. Black ink (5ml) was mixed with ^{99m}Tc (1480 MBq) and injected into the cartridge. The concentration of activity and ink was such that ± 370 MBq of ^{99m}Tc was uniformly distributed on an A3 size paper, as illustrated in Figure 3.10. The integrity, including uniformity, of using a printed source produced in this manner was evaluated by Van Staden et al., (2007). The printed source was found to be comparable to the standard commercially available ^{57}Co transmission sheet sources. Acquisition parameters used were as described in Section 3.2.3.2.

Figure 3-10: *Hewlett-Packard inkjet printer (HP 1220C), cartridge and radioactive ink solution mixed with ^{99m}Tc used to print the uncollimated paper transmission source.*

The effect of attenuation on data quantification is more pronounced than that of scatter. Therefore it seemed imperative to evaluate the integrity of the attenuation correction parameters to be used in the tumour quantification process. Experimental investigations were made to evaluate factors such as; the scatter component included in the transmission images acquired with the transmission source (influenced by the detector source distance) and the integrity of the ratio used to calculate the ACF from the transmission images. These two factors influence the attenuation correction applied and may result in biased quantification results. Therefore, these parameters were investigated prior to the actual measurements for attenuation correction of the tumour quantified data. In order not to underestimate attenuation correction predicted by Equation 3.1 the scatter contribution in the calculation of the ACF should be kept minimal. This takes into consideration that the GM was calculated using scatter corrected counts. Attenuation correction is conventionally performed for planar quantification by obtaining an ACF. This factor is obtained by measuring blank and transmission images acquired with and without the object in the field of view (FOV) respectively. The ACF is used to numerically correct for the effects of attenuation in planar images.

The measurement geometry of the blank and transmission scans was evaluated. This was done following the findings by Van Staden et al (2011), that increased detector source distance ($\geq$ 60 cm) resulted in the scatter component of the printed uncollimated source to be comparable to that obtained using a collimated transmission source (Van Staden et al., 2011). This concept was applied to decrease the scatter component in the ACF measurements as discussed in the following section (Section 3.2.4.4.1).

3.2.4.4.1 Evaluation of the transmission source.

a) Investigation of scatter fraction as a function of detector transmission source distance.

The assumption of a decreased scatter component through an object using a printed transmission source, was validated by acquiring transmission images at various detector transmission source distances (DTSDs). The PVC phantom was filled with water similar to preparations for tumour emission acquisitions explained in Section 3.2.3.1. However, for these acquisitions the tumours were removed from the phantom, and the slider moved away from the positions where the tumours were normally positioned, and no activity injected in the liver. The printed transmission source was mounted to detector two, the water filled PVC phantom was placed on the patient bed in the FOV, and transmission images were acquired using detector one to maximize the DTSD (Figure 3-11). Acquisitions were performed using the modified TEW, as described in Section 3.2.3.2. The DTSD was varied from 43 cm to 73 cm (maximum distance attained by the gamma camera gantry constraints), in increments of 5 cm, by moving detector two fitted with the transmission source away from the phantom.

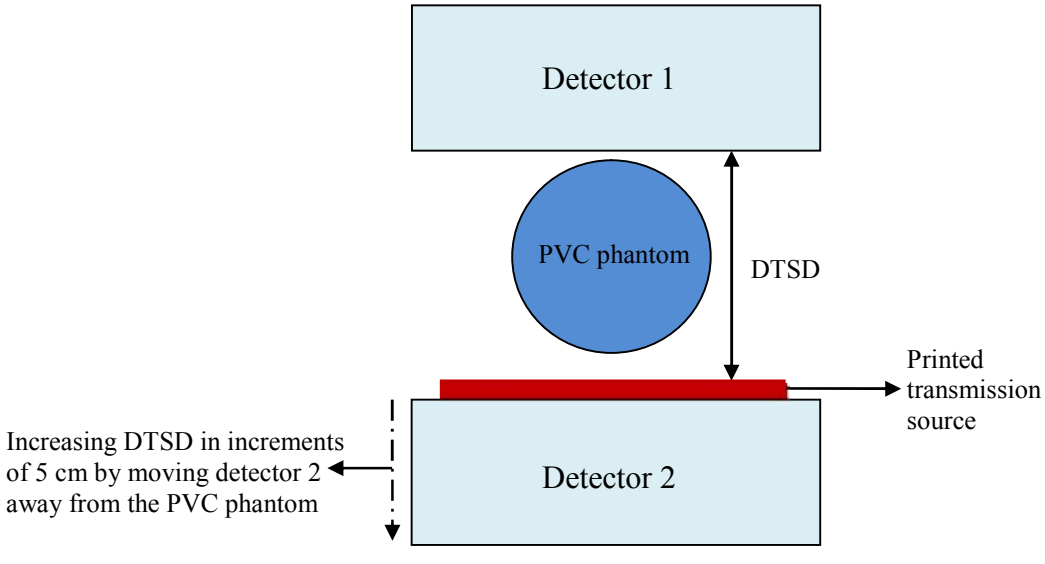

Figure 3-11: *Setup used to acquire transmission and blank images for various detector transmission source distances (DTSDs).*

The counts in the transmission images obtained in the photopeak and scatter windows were analyzed by superimposing the saved ROI's for positions of Tumour I and Tumour IV, for the 3 cm tumour-liver distance. The exact attenuation position of the tumours was achievable due to the rigid reproducible positioning of the phantom on the markings of the bed, as shown in Figure 3-3(a), thus eliminating the need for fiducial markers. The scatter fraction for the

printed transmission source, over position of Tumour I and IV in the phantom, was calculated using Equation 3.5 and the results plotted as a function of DTSD.

b) Investigation of the attenuation correction factor calculation.

Calculations were also made from the above mentioned measurements to investigate the influence of the scatter component at various DTSDs on the ratio used to calculate the ACF for tumour attenuation correction. This was based on the fact that the ratio of counts used to calculate the ACF was in accordance with the theoretical concept of γ-ray attenuation through a thickness of material, as shown in Equation 3.7.

$$C_{transmissi\ on} = C_{blank}\, e^{-\mu x} \qquad \textbf{3. 7}$$

where: $C_{transmission}$ and C_{blank} are the counts obtained from transmission and blank images acquired with and without the phantom in the FOV, x is the phantom thickness (cm) and μ is the linear attenuation coefficient (cm^{-1}). In addition to the above mentioned transmission acquisitions (3.2.4.4.1(a)), a blank image was acquired at a DTSD of 73 cm. Similarly, counts from the blank image were obtained by superimposing ROIs for Tumour I and IV positions, as was done for the abovementioned transmission images. However, this time the ROIs for Tumour I and IV positions, at the tumour-liver distances of 0 cm, 3 cm and 6 cm, were superimposed at their respective positions for the various DTSDs. The average ratio (of the three distances) of the blank and transmission counts was plotted as a function of DTSD.

The blank image was acquired at the maximum DTSD of 73 cm. This is owing to the fact that the difference in the relative scatter contribution between the counts in the transmission images, for varying DTSD, was attributed to object scatter from the PVC phantom, which was not present in the blank image. Thus any other scatter contribution beside the object scatter would be similar for the blank and transmission images for the various DTSDs.

From the above results, the average thickness (x) of the phantom, through which the γ-rays from the printed transmission source traversed, was calculated using Equation 3.7. The average linear attenuation coefficients (for three sets of independent measurements) measured for water under broad beam geometry with minimal scatter conditions were used in these calculations (described in Section 3.2.4.4.3). The effective thickness was calculated for

DTSD of 43 cm and 73 cm for positions of Tumour I and IV. The calculated thickness was compared to the average measured thickness for the positions of Tumour I and IV. An average thickness was measured, at the peripheries (t_1 and t_3) and centre (t_2) of the tumours, as they extend over different thicknesses of the phantom over the length of the tumour (Figure 3-12). The percentage difference, between the measured and calculated thickness, was calculated using Equation 3.8.

$$Difference\ (\%) = \frac{Measured - Calculated}{Measured} \times 100 \qquad \textbf{3. 8}$$

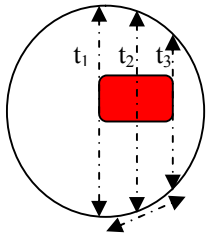

Average thickness traversed by the tumour where $t_1 > t_2 > t_3$.

Figure 3-12: *Changing phantom thicknesses over the length of the cylindrical tumours.*

3.2.4.4.2 Attenuation correction factor for tumour quantification.

From the above measurements, it was found that a DTSD of 73 cm approximates narrow beam conditions best. Therefore blank and transmission images for tumour quantification were acquired at this DTSD, as described in the preceding section with the tumours removed from the PVC phantom and the liver containing no radioactivity (Section 3.2.4.4.1). ACF measurements were performed on a weekly basis, in accordance with tumour emission data acquisitions. The counts used to calculate the ACF were obtained by superimposing saved ROI's, on the blank and transmission images obtained in the photopeak window, at tumour-liver distances of 0 cm, 3 cm and 6 cm. The ACF was calculated using Equation 3.9 (Macey et al., 1999). The results for the average ACF at the above tumour-liver distances, for Tumour I to IV, measured over a period of ten weeks are reported.

$$ACF = \sqrt{\frac{C_{Blank}}{C_{transmission}}} \qquad \textbf{3. 9}$$

Simultaneous emission and transmission acquisitions were not acquired for this project due to the same radionuclide (^{99m}Tc), being used for the emission and transmission studies. Subtraction of emission counts from simultaneous emission-transmission counts was complicated by the fact that the count density from the transmission source area underlying the tumour area was lower than the contribution from the emission data. The results obtained in this manner would be susceptible to noise due to error propagation, and thus erroneous and inconsistent results would be obtained.

3.2.4.4.3 Linear attenuation coefficients.

Although the ACF was measured under minimal scatter conditions, at DTSD of 73 cm, a scaling factor had to be introduced to account for the effect of the remaining scatter. Taking into consideration that the GM of counts were scatter corrected, it was necessary to apply a narrow beam ACF for the attenuation correction. Thus, linear attenuation coefficients were measured for narrow beam and broad beam conditions (under minimal scatter condition at 73 cm), for water and Perspex, to introduce the scaling factors shown in Equation 3.1. The average linear attenuation coefficients of water for ^{99m}Tc for three sets of measurements, measured under narrow beam and broad beam conditions, were determined.

a) Linear attenuation coefficient for water.

Linear attenuation coefficients of water for ^{99m}Tc were measured using the uniformly filled water bath phantom described in Section 3.2.2.2 (Figure 3-6). The phantom was filled with water to different depths in increments of 1 cm up to 4 cm, and then increased increments of 2 cm up to 20 cm. Appropriate volumes of water for the described increments were determined prior to measurements. Room background images were acquired for 5 minutes and normalized to 60 second acquisition, followed by 60 seconds transmission acquisitions at various water depths. A saved ROI, large enough to include most counts with percentage error of $\leq 1\%$ for all depths, was used to obtain counts from images acquired in the photopeak energy window. Linear attenuation coefficients were determined from the slope of the exponential plot of the decay corrected counts as a function of attenuation medium thickness.

Linear attenuation coefficients were first measured under narrow beam conditions, as shown in Figure 3-13. This was achieved by placing a vial containing 1110 MBq of ^{99m}Tc inside a lead shield with a 5 mm opening, a design which was based on narrow beam geometry

concepts (Brindha et al., 2004; Brown et al., 2008; Trapp et al., 2002). The detector source distance (indicated in Figure 3-13) was set at 1.4 m and images were acquired as described above. Narrow beam linear attenuation coefficients were calculated using transmission images obtained from the collimated ^{99m}Tc source. The average linear attenuation coefficient, was compared to linear attenuation coefficients obtained from the National Institute of Standards and Technology (NIST), USA published data (Hubbell and Seltzer, 2004). Linear interpolation was performed to determine linear attenuation coefficients from the X-ray mass attenuation coefficients tabulated by NIST.

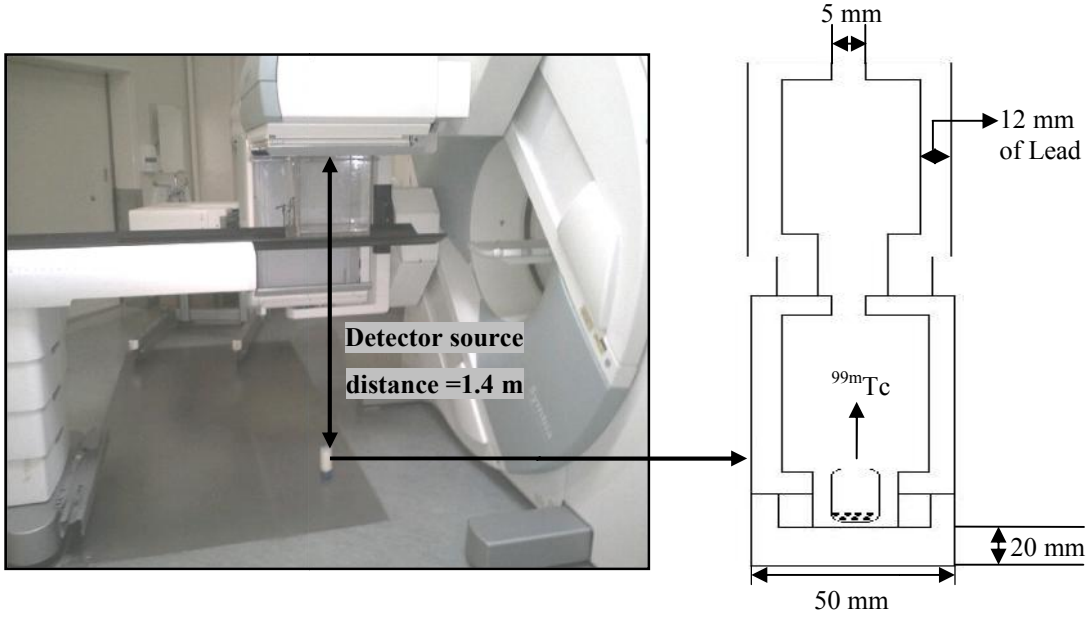

Figure 3-13: *Narrow beam geometry used to measure ^{99m}Tc linear attenuation coefficients for water using a modified lead pot.*

Linear attenuation coefficients were also measured under broad beam conditions with minimal scatter contribution. This was performed using a ^{99m}Tc printed transmission source of ±111 MBq to achieve a count rate of ≤ 10 kcps, similar to that obtained above for narrow beam geometry. The DTSD was set at 73 cm resembling the setup for transmission and blank data of the PVC phantom for tumour attenuation correction (mentioned in Section 3.2.4.4.2). Linear attenuation coefficients for broad beam were calculated as described above.

To illustrate the difference between narrow beam and broad beam transmission data, for various water depths, a blank scan was acquired for 60 seconds in addition to the above mentioned narrow beam and broad beam transmission images. Counts were obtained from the blank images using the saved ROIs used for the transmission data. The ACFs for narrow beam and broad beam geometries at various water thicknesses were calculated using Equation 3.9 and are reported. The scaling factor (Wk_1) (to account for the fact that the ACF was not measured under ideal narrow beam conditions) for water measurements shown in Equation 3.1 was calculated and reported.

b) Linear attenuation coefficient for Perspex.

The geometry used to measure the SCF (described in Section 3.2.4.5) incorporated Perspex as the attenuating medium. Therefore, linear attenuation coefficients for ^{99m}Tc were also measured using Perspex to account for scaling factors used for attenuation corrections of the SCF. Scaling factors were calculated to account for the differences between narrow beam and broad beam geometries for Perspex. Linear attenuation coefficients were measured using 16 slabs of Perspex, with a total thickness of 17.3 cm (Figure 3-7). Measurements were first made in one slab thickness increments to a total thickness of approximately 4.4 cm of Perspex. The increment was then increased to two slabs until a total thickness of 17.3 cm was measured. Acquisition and processing of the data were the same as that described for the water measurements for broad beam and narrow beam conditions, only this time with Perspex slabs in the field of view. Average linear attenuation coefficients for broad beam and narrow beam conditions were reported for Perspex. The average linear attenuation coefficients measured under narrow beam condition were compared to linear attenuation coefficients obtained from NIST published data. Similar to the water measurements, a scaling factor (Pk_1), as shown in Equation 3.1, for the Perspex measurements (used to account for the fact that the ACF for the SCF was not measured under ideal narrow beam conditions) was calculated and reported.

3.2.4.5 System calibration factor.

The gamma camera sensitivity factor is used to convert image counts to units of radioactivity. The standard method to obtain the sensitivity factor is prescribed by NEMA (NEMA, 2007) (Chapter 2, Section 2.7). Due to the dependence of the sensitivity factor on factors mentioned in Chapter 2, it was therefore necessary, for quantification purposes, to determine

the sensitivity factor under a similar acquisition geometry as that used for the tumour activity quantification. This entailed introducing an attenuating material in the measurement geometry of the sensitivity factor. In so doing, similar degradation factors, as those encountered in activity quantification measurements, would also be experienced and therefore the same processing techniques (as for the tumour quantification data) could be applied (Equation 3.1). Thus the effects of quantification corrections and processing parameters are built into the sensitivity factor. The sensitivity factor for this project was determined under conditions that differed from standard methods and it is for this reason that it is called the SCF.

The SCF was measured using a simple and practical method that would include effects of attenuation and scatter which incorporated the use of a flat printed radioactive disk produced in the same manner as described in Section 3.2.4.4. The concentration of ink and ^{99m}Tc was such that ± 20 MBq of ^{99m}Tc was uniformly distributed on a 85 cm diameter disk equivalent to the in-house Petri dish available for sensitivity measurements.

Production of the radioactive source in this manner is advantageous to the Petri dish method for the following reasons: chances of spills during acquisitions were eliminated, contamination was minimal, activity was uniformly distributed and the radioactivity of the disk was directly measured in the dose calibrator. Thus no attenuation from water was experienced and no self absorption occurs from the printed radioactive disk when acquired with the gamma camera. This would affect the sensitivity results. Ideally the SCF would be measured with water as the attenuator however; the application of the printed disc for that purpose would be impracticable. The use of Perspex slabs was a robust and efficient way of introducing attenuating material for calibration factor measurements and could easily be implemented for routine measurements during quantification studies.

The radioactive disk was placed within a thickness of 17.3 cm of Perspex. A total of 10.7 cm was used as backscatter for the radioactive disk and 6.6 cm was placed on top as shown in Figure 3-14. The gamma camera detectors were moved to the setup resulting in detector source distances of 7.6 cm and 15.7 cm for detector one and two respectively with the Perspex in place. Anterior and posterior images of the disk were acquired.

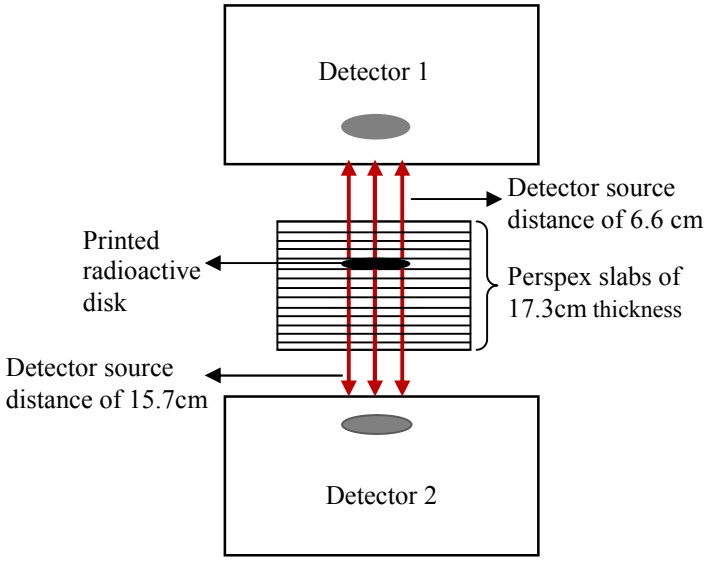

Figure 3-14: *Experimental setup used to measure the system calibration factor for tumour quantification data.*

The SCF was calculated from the GM of the anterior and posterior counts of the printed radioactive disk images. Anterior and posterior counts were obtained using a saved ROI determined from the physical size of the printed radioactive disk. The same processing techniques used for tumour quantification data (Section 3.2.4) were applied to the SCF data calculated using Equation 3.10.

$$SCF\left(cps/MBq\right)=\frac{\sqrt{C_{AP}\times C_{PP}}\times ACF_{BB\_^{99m}Tc\_Perepex}\times Pk_1}{A\left(MBq\right)\times t\left(s\right)} \qquad \textbf{3. 10}$$

where: C_{AP} and CP_P are the anterior and posterior primary counts obtained from the ROI defining the SCF radioactivity distributions. The primary counts were calculated using the counts recorded in the photopeak window corrected for decay, room background and scatter. $ACF_{BB\_^{99m}Tc\_Perspex}$ is the attenuation correction factor measured for Perspex at DTSD of 73cm. The $ACF_{BB\_^{99m}Tc\_Perspex}$ shown in Equation 3.10 was calculated using Equation 3.9 obtained in the same manner as described in Section 3.2.4.4.2, using the Perspex slabs. A plot of the SCF, for the different days of measurement of tumour quantification data, measured over a period of four months is reported.

The SCF was reanalyzed, to compensate for spill-out due to PVE, using the same criteria for ROI definition as that used for the tumour quantification data (Discussed in Section

3.2.4.6.1). A plot of the SCF using 30 % and 10 % window level for inclusion of the majority of counts is reported. The average SCF obtained from ROIs defined by the two window levels was compared to the results obtained for sensitivity, measured according to the NEMA guidelines, during acceptance tests of the Symbia T (NEMA, 2007).

3.2.4.6 Tumour activity quantification.

Tumour activity quantification accuracy was determined with reference to activity measurements in the dose calibrator as mentioned in Section 3.2.3.1. Tumour activity was calculated using Equation 3.1 and the same data processing techniques were applied to both tumour quantification data and SCF data as discussed in Sections 3.2.4.1 to 3.2.4.5. Data processing, in accordance with Equation 3.1 began with ROI definitions, according to the physical dimensions of both the tumours and the SCF. Therefore PVE resulting in spill-out of counts was not taken into consideration in the ROI definition. Scatter and room background corrections were applied and the GM of counts obtained. Attenuation correction was applied using the ACFs obtained from measurements of blank and transmission images. These images were acquired using an uncollimated ^{99m}Tc printed transmission source measured at DTSD of 73 cm to exclude scatter in the transmission source to a large extent. Scaling factors were applied to scale the measured ACFs to narrow beam conditions. Activity quantification was obtained by dividing the counts, corrected for room background, scatter and attenuation, by SCF. Tumour activity quantification accuracy was calculated using Equation 3.11.

$$Accuracy\,(\%) = \frac{Measured\ \ Activity - Quantified\ \ Activity}{Measured\ \ Activity} \times 100 \qquad \textbf{3. 11}$$

where: the *measured* and *quantified activity* is the tumour activity measured in the dose calibrator and the quantified image activity distribution respectively.

Data were reanalysed to take PVE into account, as discussed below (Section 3.2.4.6.1 (b)). The effect of geometry on quantification accuracy was evaluated for three variables namely: (I) varying tumour-liver distance (II) varying tumour sizes as a function of tumour-liver distance and (III) influence of two tumour-background ratios. These investigations, repeated three times on different days, are discussed below.

3.2.4.6.1 Quantification without background activity.

Tumour quantification without background activity in the PVC phantom investigated the first two variables of this research project i.e. varying tumour size and distance from the liver. The influence of these variables on tumour activity quantification accuracy was investigated with and without compensation for PVE.

a) Quantification without compensation for partial volume effects.

The quantification data were first analysed using counts obtained from ROIs defined by the physical dimensions of both the tumours (Section 3.2.4.1) and the printed radioactive disk used for measurements of the SCF (Section 3.2.4.5). A plot of the accuracy (%) for Tumour I to IV for repeated measurements addressing two of the above mentioned variables is shown.

b) Quantification with compensation for partial volume effects.

As discussed in Chapter 2, Section 2.3.5, tumour information i.e. counts, is not only contained in corresponding pixels, but also in neighbouring pixels. This is due to spill-out of information encountered due to the PVE experienced from the limited spatial resolution of the gamma camera. Therefore definition of the ROIs, from physical dimensions as described above, resulted in exclusion of counts from neighbouring pixels containing counts from the tumours. For that reason the data were reanalyzed by drawing ROIs that included most of the counts. This is a criteria that has been suggested as there is no universal method for ROI definition in nuclear medicine (Zaidi and Koral, 2005).

The criterion for ROI definition was to include the majority of counts without overlap between the tumour, liver and pipes for liver filling and drainage. This was achieved by adjusting the window level to 30 % of maximum count for Tumour I and 10 % of maximum counts for Tumour II to IV. A 10 % window level for Tumour I resulted in spill-in of liver counts into the tumour and spill-out of the tumour counts into the liver, to the extent that the tumour and liver were visually one image. Good separation between the liver and the tumour was observed at the 30 % window level.

The same processing criteria were used for the SCF data which were reanalyzed using the 30 % window (applied to Tumour I) and 10 % window (applied to Tumour II and IV data). A plot of the accuracy (%) for Tumour I to IV, for repeated measurements, using larger ROIs to compensate for PVE is reported.

3.2.4.6.2 Quantification with background activity.

The third variable to be investigated was the influence of background activity on tumour quantification accuracy. This was done for tumour-background ratios of 0.5 % and 1 % as mentioned in Section 3.2.3.1. Tumour II was used for this investigation and the same processing techniques as those mentioned in Section 3.2.4.6 were applied. Similarly, data were analysed with and without compensation for PVE. The average accuracies, for repeated measurements, for the two tumour-background ratios with and without PVE compensation are tabulated. These average results were compared to the accuracy achieved for Tumour II without background activity. The objective was to calculate the contribution of the added background activity on the tumour quantification accuracy. For that reason background correction was not applied

3.3 Results and Discussions.

3.3.1 Equipment stability.

3.3.1.1 Dose calibrator.

a) Dose calibrator accuracy.

The accuracy of the Capintec CRC-15R dose calibrator used for this study was good; it underestimated the ^{99m}Tc activity measured by NMISA with -0.4 %. Several causes for inaccuracy in dose calibrators can include: change in voltage signal amplification for the specific radionuclide setting, electronic drift with time or changes in the gas pressure. This rather small inaccuracy may be attributed to random errors. The accuracy obtained with the dose calibrator was acceptable for quantification purposes. The small underestimation of the ^{99m}Tc activity would not affect the accuracy with which the quantified data would be obtained as this underestimation is built into the quantification process (Equation 3.1) by the SCF.

b) Dose calibrator reproducibility.

Figure 3-15 shows the reproducibility of the dose calibrator for the different days of measurement using a Cs-137 source. It can be seen from Figure 3-15 that the dose calibrator was consistent during the period of measurements. The average radioactivity value

calculated for the different days of measurements was 49.4 ± 0.18 MBq, indicating a good precision and stability between measurement days.

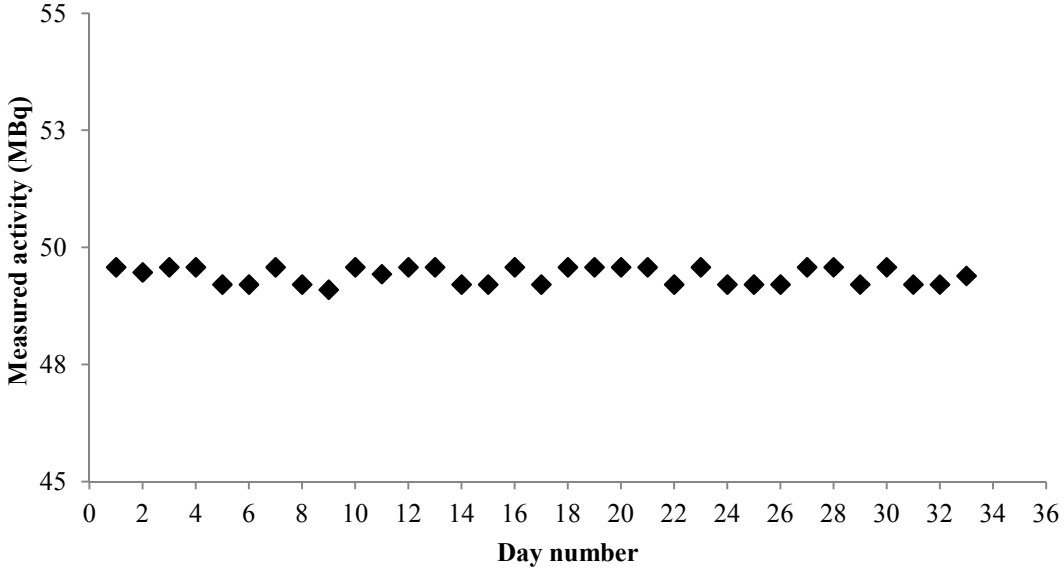

Figure 3-15: *The Capintec CRC-15R dose calibrator reproducibility for the different days of measurements using the ^{137}Cs radionuclide.*

3.3.1.2 Gamma camera quality control.

a) Intrinsic flood field uniformity.

The average intrinsic uniformity values obtained from weekly ^{99m}Tc flood field images of the Symbia T over a period of nine months are shown in Table 3-1. The standard deviation indicated small variations of intrinsic uniformity measurements for the different weeks of measurements. The maximum average uniformity value was 1.94 ± 0.21 %, for detector two, indicating the Symbia T was stable and performing optimally over this time period.

Table 3-1: *Symbia T intrinsic flood field uniformity values for ^{99m}Tc.*

	Detector 1 (%)	Detector 2 (%)
IU:		
UFOV	1.93 ± 0.19	1.94 ± 0.21
CFOV	1.57 ± 0.13	1.59 ± 0.16
DU:		
UFOV	1.24 ± 0.10	1.25 ± 0.14
CFOV	1.03 ± 0.09	1.07 ± 0.12

b) Intrinsic count rate performance.

The maximum count rates for detector one and two were 328 kcps and 332 kcps respectively. The 20 % count rate loss was obtained at 314 kcps and 326 kcps for detector one and two respectively. These values were comparable to the values obtained during acceptance tests for the Symbia T in August 2008. Therefore significant count losses were only observed at high count rates not routinely used for clinical acquisitions. The maximum count rate used during acquisitions of this research project was < 10 kcps (observed count rate was < 10 kcps and < 5 kcps for transmission and emission images respectively), where count loss was < 1% for both detector one and two. Therefore count losses had negligible effects on the quantification accuracy.

3.3.2 Phantom description.

3.3.2.1 Polyvinyl chloride abdominal phantom.

Single slices of linear attenuation maps, measured with the CT scan scaled to the energy of ^{99m}Tc, for the PVC phantom and a patient are shown in Figure 3-16. Comparison of linear attenuation coefficients of the spinal regions for the PVC phantom and patient (indicated by arrows) were found to be comparable ($0.205cm^{-1}$ vs. $0.213cm^{-1}$) with a percentage difference of 3.756 %. It can be assumed that the PVC can represent the bony anatomy found in clinical images.

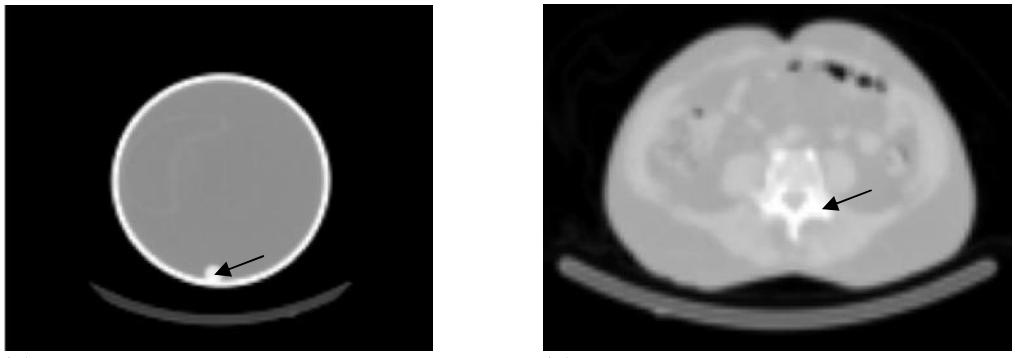

(a) *(b)*

Figure 3-16: *Attenuation maps obtained from CT scans of the Symbia T SPECT/CT scaled to the energy of ^{99m}Tc (a) PVC phantom (b) Bone scan of a patient.*

3.3.3 Data processing.

3.3.3.1 Region of interest definition.

The percentage uncertainty for the total counts recorded in the photopeak window for anterior and posterior views, for all tumours, was ≤ 0.5% (See Appendix A, Table A1-A4). Although smaller ROI's were selected for Tumour III and IV, the total counts recorded in their photopeak windows resulted in percentage uncertainties of 0.4 % and 0.5 % respectively. This small percentage uncertainty can be attributed to the increased concentration used in these smaller tumours. Similar results were observed for repeated measurements. The use of smaller pixel sizes or a larger matrix size (256 × 256 as opposed to 128 × 128) resulted in small variations of the tumour ROI (saved for repeated use) reproducibility for the images acquired on different days.

The counts for room background were found to contribute < 0.2 % of the total counts recorded in the photopeak window and had a negligible effect on the final quantification result. It is not surprising as all measurements were performed after all the clinical acquisitions were completed for the day. No detector contamination or stray radiation from patients in the hallways was encountered before or during phantom acquisitions.

3.3.3.2 Scatter correction using the modified triple energy window.

Figure 3-17 shows the energy spectrum of ^{99m}Tc acquired using Tumour I. It can be seen that the energy spectrum approaches zero above 150 keV and thus renders the use of an upper energy sub-window unnecessary. There is a fair amount of primary photons included in the

scatter sub-window. This is observed when using multiple energy window scatter correction techniques where scatter sub-windows are placed directly adjacent to the photopeak energy window. Although the trapezoid shape scatter estimate used in the TEW is not the true shape of the scatter distribution it is a reasonable approximation.

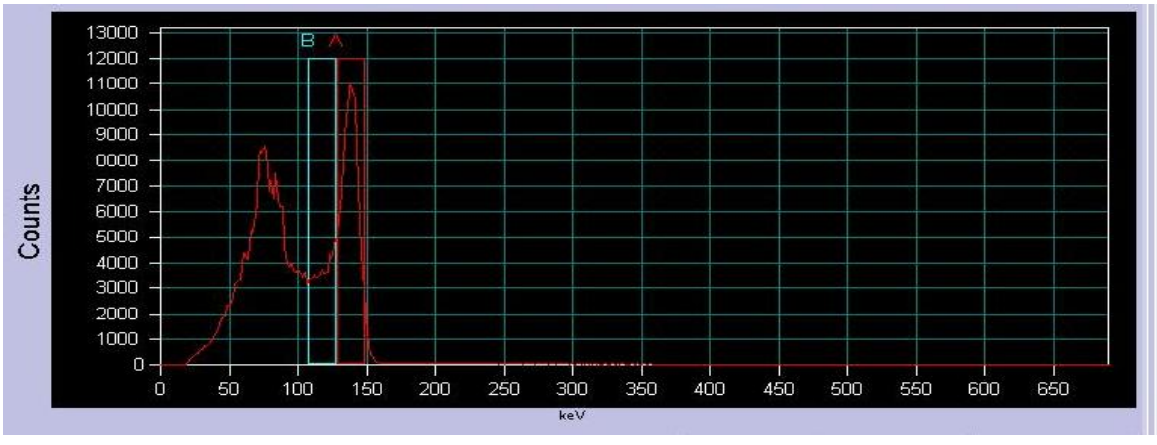

Figure 3-17: *An acquired energy spectrum for ^{99m}Tc with a primary energy window (A) and lower energy sub-window (B).*

A plot of the GM of the scatter ratio counts is shown in Figure 3-18. It can be seen from Figure 3-18 that the average scatter ratios for Tumour I to IV were 0.19 ± 0.02, 0.15 ± 0.01, 0.12 ± 0.01 and 0.11 ± 0.01 respectively, for tumour-liver distances of 0 cm, 3 cm and 6 cm. The highest scatter contribution was seen for the largest (Tumour I) and the least for the smallest tumour (Tumour IV). This may be attributed to the increased probability of scattered γ-rays due to the large tumour size. This was in accordance with literature findings that scatter fraction increased with an increased amount of scatter medium (Kojima et al., 1991). The scatter fraction decreased with increased distance from the liver. This can be attributed to the exclusion of scatter from the liver at increased distances.

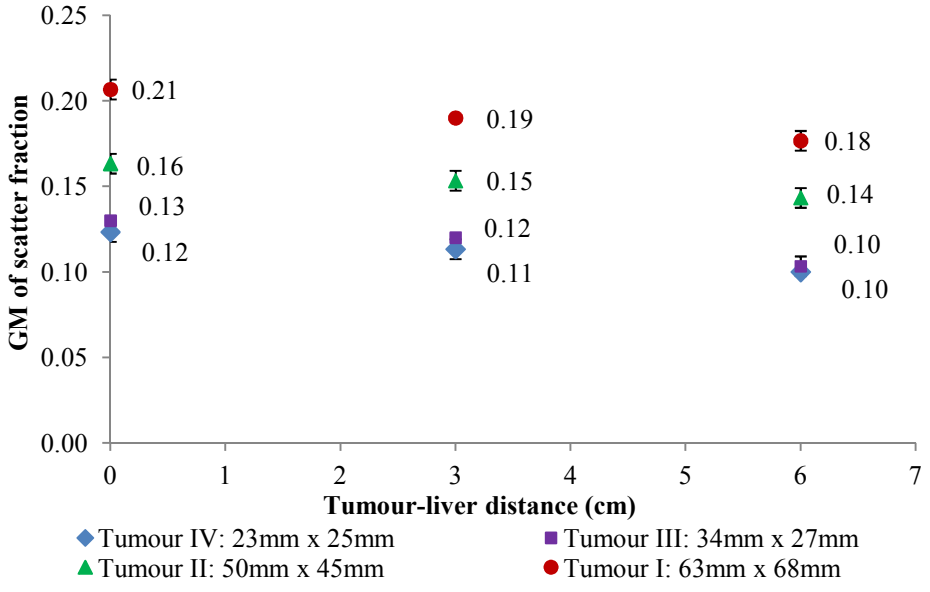

Figure 3-18: *The geometric mean of the average scatter fraction values obtained during different days of measurement for Tumour I to IV as a function of tumour-liver distance.*

3.3.3.3 Geometric mean

Table 3-2 shows the GM of the scatter corrected counts for one set of measurement for Tumour I to IV.

Table 3-2: *The geometric mean of counts corrected for room background and scatter for Tumour I to IV at different tumour- liver distances.*

Tumour-liver distance (cm)	Tumour I	Tumour II	Tumour III	Tumour IV
0	280475 (100 %)	210972 (100 %)	103719 (100 %)	53426 (100 %)
3	269890 (96.2 %)	205612 (97.5 %)	100550 (96.9 %)	52413 (98.1 %)
6	265452 (94.6 %)	205005 (97.2 %)	98960 (95.4 %)	51531 (96.5 %)

There was a decrease in the number of counts calculated with the GM (with scatter correction applied) method with increased tumour-liver distance. The number of counts obtained with

the GM method for the distances 3 cm and 6 cm were found to be comparable for all tumour sizes. The GM of counts was expressed as a percentage of the counts obtained at 0 cm. The percentage count difference for tumour liver distances of 3 cm and 6 cm, was ≤ 1.6 %. This percentage count difference increased to ≤ 3.8 % between tumour liver distances of 0 cm and 3 cm. The geometry at 0 cm resulted in the liver partially overlaying the tumours (Figure 3-19). The increased counts at 0 cm can therefore be attributed to the fact that some counts from the liver, which were included in the photopeak window, were also included in the ROI definition for all tumours. The contribution at 0 cm may be attributed to small angle scatter and primary events from the liver that may be included in the ROI definition. The effect of increased counts at 0 cm was more pronounced for Tumour I as the liver overlay a larger area of this tumour.

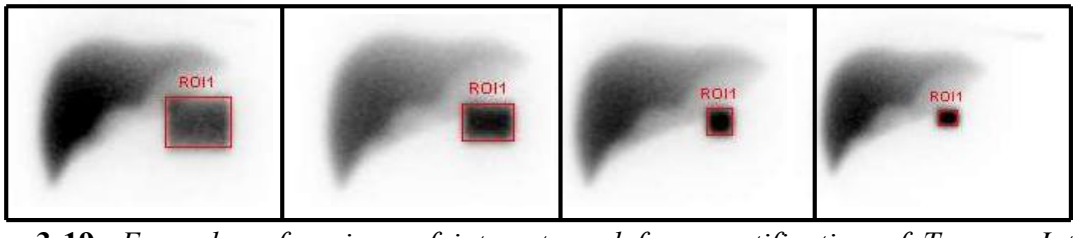

Figure 3-19: *Examples of regions of interest used for quantification of Tumour I to IV respectively, at tumour-liver distance of 0 cm.*

The effect of scatter from the liver is expected to have minimal influence on the GM results as it was compensated for using the modified TEW scatter correction technique. This was evident from the comparable counts obtained at tumour-liver distances of 3 cm and 6 cm, observed for all tumour sizes. The GM of counts decreased with increased tumour-liver distance, for all tumour sizes, however to a lesser extent for 3 cm and the 6 cm. The same trend was seen for the three sets of acquisitions.

3.3.3.4 Attenuation correction.

3.3.3.4.1 Evaluation of the transmission source.

a) Investigation of scatter fraction as a function of detector transmission source distance

Results for the scatter fraction, due to the PVC phantom in the FOV, measured using the uncollimated ^{99m}Tc printed transmission source at various DTSDs for positions of Tumour I and IV are shown in Figure 3-20 (a) and (b). It can be seen, that the scatter fraction decreased with increasing DTSD due to the increased distance between the transmission

source and the PVC phantom. The counts recorded in the photopeak for Tumour I and IV had a percentage error of ≤ 1% and ≤ 3% respectively, where the latter was susceptible to statistical fluctuations for measurements at the various DTSDs. Although the scatter component decreased with increasing DTSD, further calculations (See subsequent Section 3.3.3.4.1(b)) were made on these acquisitions to validate the influence of the decreased scatter component on the ratio used to calculate the ACF, for attenuation correction of the tumour data. Thereby, the optimum distance for ACF measurements could be determined.

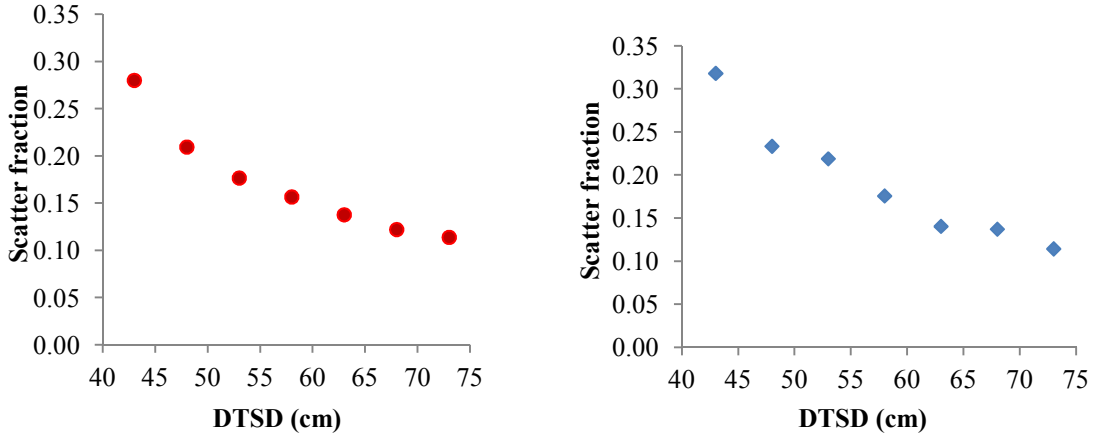

(a) *(b)*

Figure 3-20: *Scatter fractions of transmission images acquired using an uncollimated ^{99m}Tc printed transmission source for positions of (a) Tumour I and (b) Tumour IV acquired at various detector transmission source distances (DTSDs).*

b) Investigation of the attenuation correction factor calculation

The average ratios of the blank and transmission image counts, obtained from position of Tumour I and IV in the phantom, for distances 0 cm, 3 cm, 6 cm from the liver measured at various DTSDs are shown in Figure 3-21. It can be seen from Figure 3-21 that the average ratio of the blank and transmission counts increased with increased DTSD. This was attributed to the decreased scatter component with increased DTSD shown in Figure 3-20, indicating that there would be an underestimation of the ACF at decreased DTSD. There was a small variation of this ratio for the various distances from the liver for both Tumours I and IV with absolute standard deviations of ≤ 1 and 2 respectively. This can be expected since the thickness of the phantom traversed by the γ-rays stayed constant over these positions (Figure 3-8(b)).

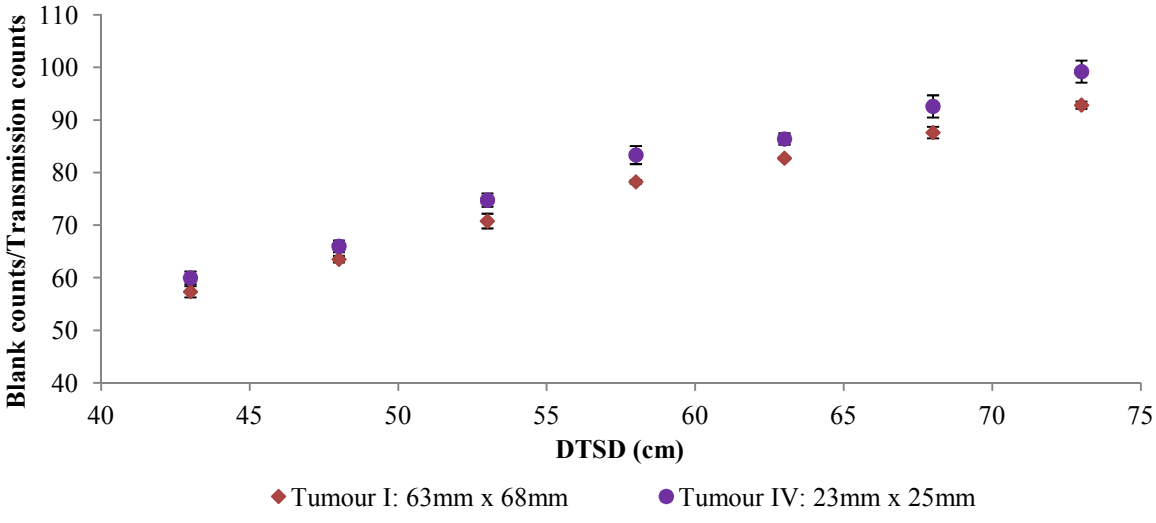

Figure 3-21: *Ratio of blank and transmission counts for various detector transmission source distances (DTSDs) used to calculate the traversed thickness.*

The average thickness was calculated at the DTSD of 43 cm and 73 cm for Tumour I and IV. The calculated thicknesses were compared to the average measured thicknesses at the positions of Tumours I and IV. The average phantom thickness, calculated using Equation 3.7, for Tumour I at DTSD of 73 cm and 43 cm was 30.03 cm and 26.73 cm respectively. The average measured thickness at the position of Tumour I was 29.75 cm, approximating the thickness calculated using the ratio of the counts measured at a DTSD of 73 cm with a percentage difference of -0.94 %. Similarly, the average thickness calculated for Tumour IV was 30.25 cm and 26.93 cm at DTSDs of 73 cm and 43 cm respectively, while the average measured thickness was 30.52 cm. The thickness calculated at DTSD of 73 cm, for Tumour IV, approximated the measured thickness with a percentage difference of 0.88 %.

The thickness calculated using ratio measured at DTSD of 43 cm had a percentage difference of 10.15 % and 11.76 % for Tumour I and IV respectively. This indicated that there would be on average a 10.95 % underestimation of the thickness measurements performed at a DTSD of 43 cm. This thickness underestimation would result in an underestimation of the ACF calculation for attenuation correction of the quantified tumour data. The ratio of blank and transmission counts underestimated the measured average thickness for Tumour I and IV when using counts measured at DTSD of 43 cm. This projected an underestimation of the attenuation correction factor to be used for tumour quantification. These results indicated that the optimum distance for ACF measurements was at 73cm, and validated the integrity of the ratio to be used for the ACF calculations at this distance.

3.3.3.4.2 Attenuation correction factor for tumour quantification.

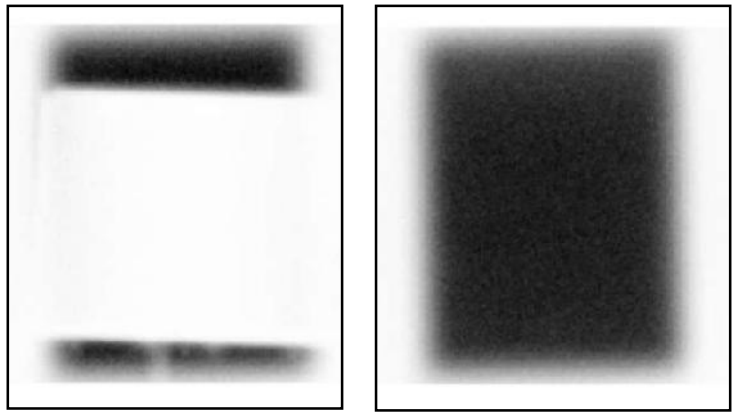

(a) ***(b)***

Figure 3-22: *Examples of images used to calculate the attenuation correction factor; (a) transmission (b) blank images.*

Example images used to calculate the ACF for quantification of Tumour I to IV, for tumour-liver distances of 0 cm 3 cm and 6 cm, are shown in Figure 3-22. The non-uniformity observed at the bottom of the transmission images was due to the screws on the Perspex plate emerging from the phantom for removal of air bubbles as well as the slider (See Figure 3-3(a)). The average ACF results for the four tumours acquired over a period of ten weeks are shown in Table 3-3 (See Appendix A Table A5).

Table 3-3: *Average attenuation correction factors (ACFs) for different tumour sizes measured at the various tumour-liver distances.*

	$ACF_{Tumour\ I}$	$ACF_{Tumour\ II}$	$ACF_{Tumour\ III}$	$ACF_{Tumour\ IV}$
Average	9.82 ± 0.11	10.13 ± 0.05	10.40 ± 0.11	10.36 ± 0.12

It can be seen, from Table 3-3, that the ACF was comparable for the different size tumours. This can be attributed to the similar thicknesses traversed by each tumour (30 cm ± 2 cm). As shown in Section 3.2.4.4.1, calculating an ACF from total counts for each tumour was equivalent to averaging the thickness at each tumour. This results in a decreased difference of thicknesses between the tumours and thus comparable ACF results. Attenuation correction was applied by multiplying the GM of counts, as indicated in Equation 3.1, by the ACF.

Numerically compensating for attenuation using the ACF resulted in an average 10-fold increase in the tumour GM counts emphasizing the importance of attenuation correction.

3.3.3.4.3 Linear attenuation coefficients.

Linear attenuation coefficients for Perspex and water, measured under narrow and broad beam conditions, as well as the NIST values used for reference, are shown in Table 3-4.

Table 3-4: *Linear attenuation coefficients of ^{99m}Tc measured for narrow beam (NB) and broad beam (BB) geometry for Perspex and water.*

Measurement medium	Narrow Beam μ_{NB} (cm^{-1})	Reference μ_{NIST} (cm^{-1})	Broad Beam μ_{BB} (cm^{-1})	Scaling Factors μ_{NB}/μ_{BB}
Water	0.152 ± 0.001	0.155	0.146 ± 0.002	1.041
Perspex	0.175 ± 0.001	0.176	0.170 ± 0.002	1.029

The mean value for the measured linear attenuation coefficients under narrow beam (*NB*) conditions, for water and Perspex, showed underestimation of the NIST (μ_{NIST}) values by 1.9 % and 0.6 % respectively. These findings were comparable to literature findings (Brown et al., 2008). These underestimations are likely due to the difference in the measurement setup by NIST and the experimental setup used on Symbia T (Figure 3-13), which may include the type of collimation used, as well as the difference in characteristics of detectors used. It can also be seen that the linear attenuation coefficients for broad beam (*BB*) geometry were less than that of narrow beam geometry for both Perspex and water indicating the inclusion of some scattered photons under broad beam geometry. Under ideal conditions for broad beam, where measurements with the uncollimated printed source excluded scatter by increasing DTSD to the extent that linear attenuation coefficients approximated that of narrow beam, the scaling factor would be equivalent to 1. Under these conditions the broad beam linear attenuation coefficients would exclude scatter to the same extent as the narrow beam geometry. The scaling factors were > 1 for both water and Perspex with percentage differences of 3.9 % and 2.9 % respectively. This scaling factor indicated the extent of

scatter inclusion in the transmission measurements under broad beam conditions. As indicated by Equation 3.1, the ratio of the scaling factors of the ACFs for attenuation correction of tumours and SCFs will be used for tumour activity quantification to account for the fact that the ACFs were not measured under strictly narrow beam conditions. Thus the quantified tumour activity would be multiplied by a factor of 1.012 which would have minimal effect (≤ 1 %) on quantification accuracy. This is expected as the ACF was measured under minimal scatter conditions by increasing the DTSD to 73 cm.

Comparison of the average ACF for broad and narrow beam conditions is shown in Figure 3-23. It can be seen from Figure 3-23, that the broad beam ACF approximated that of narrow beam at shallow depths of water. At deeper depths the broad beam linear attenuation coefficient was lower. This lower attenuation coefficient at deeper depths can be attributed to the inclusion of more scattered photons in the photopeak window. This demonstrated how scatter inclusion changed the transmission of the γ-rays, and thus the ACF, in comparison to narrow beam geometry.

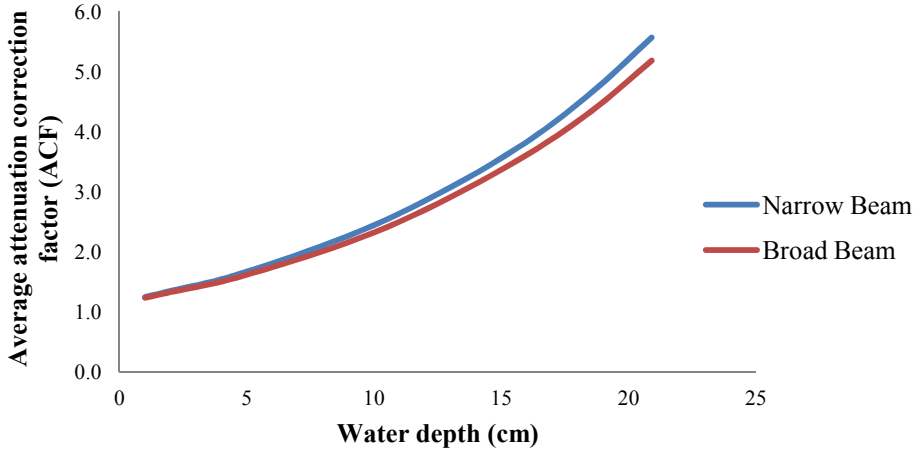

Figure 3-23: *Average attenuation correction factor for ^{99m}Tc and water measured under broad and narrow beam geometries.*

3.3.3.5 System calibration factor.

The images used in the calculation of the SCF are shown in Figure 3-24. The SCF was stable for the different days of measurements with average value of 73.95 ± 1.04 cps/MBq (Figure 3-25).

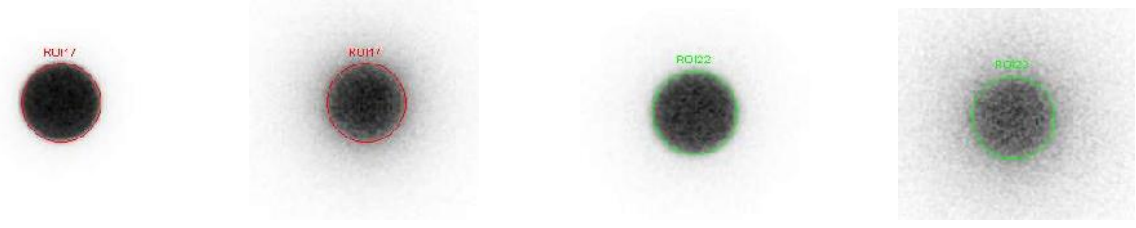

(a) *(b)* *(c)* *(d)*

Figure 3-24: *Example of images, with superimposed regions of interest drawn according to physical dimensions of the printed radioactive disk, acquired for the Perspex system calibration factor measurements. Anterior images recorded in the; (a) photopeak and (b) scatter windows, posterior images recorded in the; (c) photopeak and (d) scatter windows.*

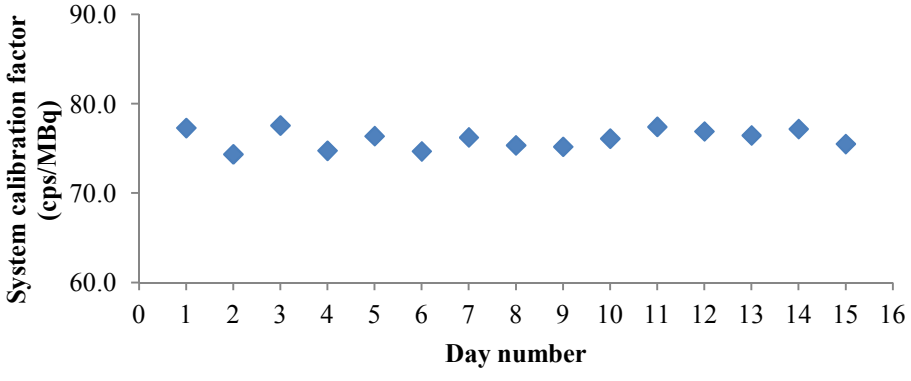

Figure 3-25: *System calibration factors measured in Perspex obtained using a region of interest size drawn according to the physical dimensions of the printed radioactive disk.*

Results for the SCF using larger ROIs to compensate for PVE are shown in Figure 3-26. The ROI was defined manually by adjusting the window levels to 30 % of the maximum counts for Tumour I and 10 % of the maximum counts for Tumour II to IV (See Section 3.2.4.6.1(b)). This resulted in larger ROI definitions and therefore inclusion of more counts of the radioactive disk in comparison to ROI defined by the physical dimensions of the radioactive disk. The average SCFs obtained from ROIs drawn using the 30 % and 10 % window levels were 80.12 ± 0.90 cps/MBq and 83.83 ± 1.04 cps/MBq respectively. The SCFs obtained with the 10 % window level were comparable to the acceptance test sensitivity measurements of 82.7cps/MBq and 82.8cps/MBq for detector one and two respectively. Acceptance testing of the Symbia T was performed in 2008 according to NEMA guidelines (NEMA, 2007). The SCF was applied to the quantification data of the tumours.

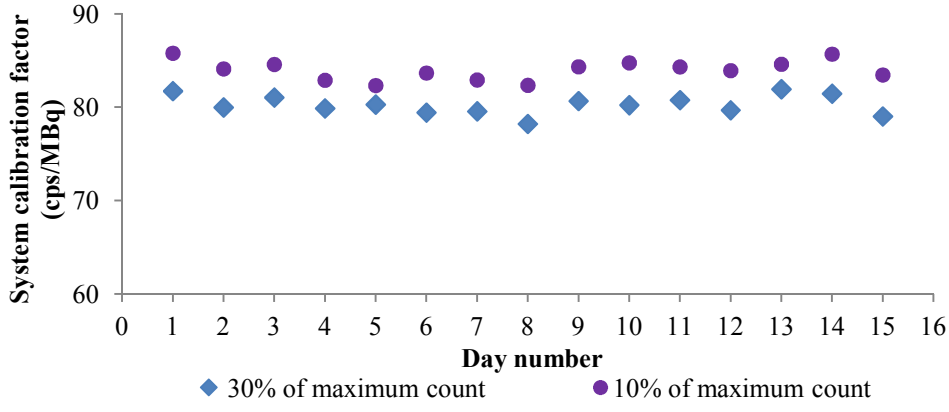

Figure 3-26: *System calibration factors obtained using larger regions of interest obtained by adjusting the window level to a percentage of maximum counts to compensate for partial volume effects.*

3.3.3.6 Tumour activity quantification.

3.3.3.6.1 Quantification without background activity.

a) Quantification without compensation for partial volume effects.

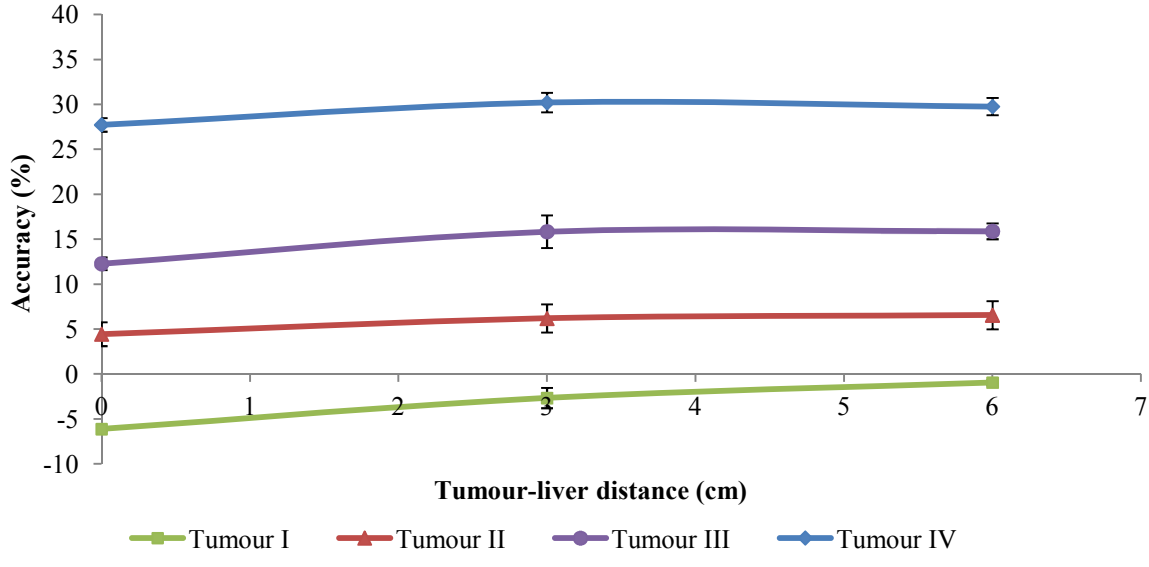

Figure 3-27: *^{99m}Tc activity quantification accuracy for Tumour I to IV without compensation for partial volume effects.*

Figure 3-27 shows the results obtained for tumour quantification accuracy, of the different tumour sizes, as a function of tumour-liver distance without compensation for PVE (See Appendix A, Table A6). As mentioned in preceding sections, all data were acquired at a

count rate < 10 kcps which had negligible count loss of < 1 %, therefore the tumour trends seen in Figure 3-27 were not influenced by count losses. Also, the counts were obtained with a percentage error of < 0.5 % and thus results were not susceptible to noise.

❖ **Varying tumour sizes.**

It can be seen from Figure 3-27 that the largest error (tumour accuracy) was observed for Tumour IV underestimating the tumour activity by 29.2 ± 1.3 %. As mentioned in Chapter 2, the PVE has a higher impact on objects that are near the resolution limit of the gamma camera i.e. three times the FWHM of the gamma camera (Hoffman et al., 1979). This was equivalent to 23.1 mm for the Symbia T with the LEHR collimator. Tumour IV had a diameter and length of 23 mm and 25 mm respectively and was susceptible to the PVE, resulting in spill-out of tumour counts to a large extent. Although Tumour III (diameter and length of 34 mm and 27 mm respectively) was also susceptible to spill-out effects it was to a lesser extent underestimating the tumour activity with an average accuracy of 14.7 ± 2.1 %. These results were in accordance with the PVE which results in an underestimation of the total activity contained within the tumours (Soret et al., 2007).

Better quantification accuracy was observed for Tumours II and I with average accuracies of 5.72 ± 1.1 % and -3.3 ± 2.6 % respectively. The quantification accuracies achieved for Tumours I and II are in accordance with literature findings for planar activity quantification accuracy (≤ 10 %). These planar activity quantification accuracies were obtained when corrections for attenuation and scatter were performed, using ACFs and the TEW scatter correction technique respectively (King and Farncombe, 2003; Macey et al., 1999; Sjögreen et al., 2005).

The quantified activity for Tumours II to IV underestimated the actual tumour activity. This was in accordance to the literature findings for quantification of the torso phantom with tumour inserts using the TEW scatter correction technique and an attenuation correction (Pereira et al., 2010). From the results it is evident that Tumour I slightly overestimated the quantified activity. This overestimation can be attributed to the large size of Tumour I in comparison to other inserts used to represent tumours in standard phantoms such as the Data Spectrum Anthropomorphic torso phantom (Data Spectrum Corporation, Hillsburg, NC, USA) and the RSD anthropomorphic torso phantom (Radiology Support Devices, Pittsburgh, USA). These inserts used in the standard phantoms have been modified to maximum diameter sizes of up to 3.4 cm (He et al., 2005; Pereira et al., 2010) which was small in

comparison to the physical dimension of Tumour I used in this project. Therefore Tumour I was less susceptible to PVE.

❖ **Varying tumour-liver distances.**

It can be seen from Figure 3-27, that there is a slight overestimation of activity when the tumour is in contact with the liver (tumour-liver distance of 0 cm). This can be attributed to overlying liver activity in the projection of the tumours, especially in the anterior view. Counts originating from primary photons and small angle scattered photons of the liver may be included in the tumour ROIs. The average underestimation, calculated as the difference between the accuracy obtained at tumour-liver distances of 0 cm and 6 cm, for Tumour I to IV was 5.2 %, 2.1 %, 3.6 % and 2.0 % respectively. The increased underestimation seen for Tumour I was due to the fact that a larger liver area was overlaying the tumour area. It could be seen from the results that Tumours II and IV underestimated the measured tumour activity comparably by 2.1 % and 2.0 % respectively. The underestimation of the measured tumour activity by Tumour III was slightly higher in comparison to Tumours II and IV. This slight increase was attributed to the different shape for Tumour III, which resembled a square rather than a rectangle (Figure 3-9). It was observed that Tumour III overlay a larger region of the liver in comparison to Tumours II and IV which resulted in a larger contribution of liver counts. It can also be seen from Figure 3-27 that the tumour accuracy trend stabilized at tumour-liver distances of 3 cm and 6 cm for all tumours. The difference in accuracy between the two distances for Tumour I to IV was less than 1.7 %.

b) Quantification with compensation for partial volume effects.

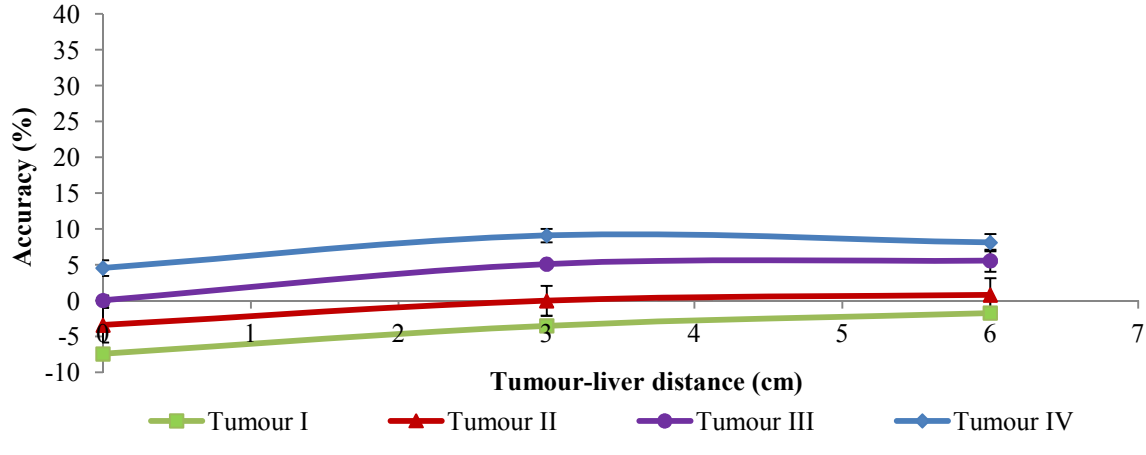

Figure 3-28: *^{99m}Tc activity quantification accuracy for Tumour I to IV with compensation for partial volume effects.*

Results obtained from processing the preceding data (Section 3.3.3.6.1(a)) using larger ROIs to compensate for PVE, as described in Section 3.2.4.6.1(a), are shown in Figure 3-28 (See Appendix A, Table A7).

❖ **Varying tumour sizes.**

It can be seen from Figure 3-28 that the accuracy of all tumours was better than 10 %, with the largest percentage deviation, for quantification accuracy, observed at -8.2 % and 10.0 % for Tumour I and IV respectively. Tumour I overestimated the measured activity with 8.2 % at a distance of 0 cm from the liver. This is expected, as the larger ROI drawn to define the largest tumour included more counts originating from the liver than the ROIs for the three smaller tumours. From Figure 3-5 it is evident that Tumour I's dimensions were not near the resolution limit of the gamma camera for PVE as mentioned in Section 3.3.3.6.1 (a). From the results shown in Figure 3-27 it was evident that Tumour I did not need PVE compensation. PVE compensation in this manner resulted in further overestimation of tumour activity by Tumour I.

❖ **Varying tumour-liver distance.**

The average underestimations, calculated as the difference between the accuracy obtained at tumour-liver distances of 0 cm and 6 cm, for Tumours I to IV were 5.7 %, 4.2 %, 5.5 % and 3.6 % respectively. The tumour trend stabilized (i.e. showed comparable accuracies) at 3 cm and 6 cm for all tumours where the difference between the two distances was less than 1.8 %. The difference was found to be comparable (1.8 % vs. 1.7 %) to the results obtained without PVE compensation, discussed in Section 3.3.3.6.1(a).

3.3.3.6.2 Quantification with background activity

Table 3-5 represents the results, without PVE compensation, obtained using Tumour II for the tumour-background ratios of 0.5 % and 1 % of the tumour activity concentration added to the background water.

Table 3-5: *Tumour II quantification accuracy for two tumour-background ratios without compensation for partial volume effects.*

Tumour-liver distance	No background activity	Background activity: 0.5 % of tumour activity concentration	Background activity: 1 % of tumour activity concentration
cm	**Accuracy (%)**	**Accuracy (%)**	**Accuracy (%)**
0	4.4 ± 1.3	0.3 ± 3.6	-12.1 ± 2.9
6	6.5 ± 1.6	2.6 ± 4.4	-9.8 ± 3.4

The addition of 0.5 % of background activity resulted in a 4.1 % and 4.0 % differences in the tumour accuracy, in comparison to the accuracy obtained without background activity present, for tumour-liver distances of 0 cm and 6 cm respectively. Addition of background activity resulted in an underestimation, to a lesser extent in comparison to the accuracy obtained without background activity, due to superimposed background activity included in the ROI counts of the tumours. The 1 % addition of tumour background activity resulted in 16.6 % and 16.4 % differences in the tumour accuracy in comparison to the accuracies obtained without background activity present, for distances 0 cm and 6 cm respectively. Contribution of background activity at tumour-liver distances of 0 cm and 6 cm was comparable for both tumour-background ratios.

Table 3-6 represents the results obtained from processing the data for the tumour-background ratios of 0.5 % and 1 % for Tumour II with larger ROIs for PVE compensation.

Table 3-6: *Tumour II quantification accuracy for two tumour-background ratios with compensation for partial volume effect*.

Tumour-liver distance	No background activity	Background activity: 0.5 % of tumour activity concentration	Background activity: 1% of tumour activity concentration
cm	**Accuracy (%)**	**Accuracy (%)**	**Accuracy (%)**
0	-3.4 ± 2.4	-15.2 ± 4.3	-29.7 ± 4.6
6	0.8 ± 2.3	-10.1 ± 4.4	25.1 ± 4.5

PVE compensation was made by including the majority of counts by adjusting the window level to 10 % of the maximum counts, as explained in Section 3.2.4.6.1(b). A background level of 0.5 % resulted in a contribution (difference) of 11.8 % and 10.9 % at 0 cm and 6 cm respectively in comparison to results without background activity. The overestimation observed was due to the inclusion of superimposed activity to a large extent due to the larger ROI used to define counts in the tumour. A background level of 1 % resulted in comparable contributions of 26.3 % and 25.9 % at 0 cm and 6 cm respectively in comparison to results without background. These contributions were in accordance with literature findings where background activity was found to be an important factor in determining activity quantification accuracy with variations of up to ± 20 % (Norrgren et al., 2003). It can be seen that the background contribution was comparable for distances of 0 cm and 6 cm for both 0.5 % and 1.0 % background ratios.

As mentioned above, background corrections were not performed as the influence of only background activity on tumour quantification accuracy was investigated. It was seen from the above results that background contribution to quantification accuracy may be up to 26.3% in comparison to results without background activity.

Background corrections are mainly made using background counts obtained from ROIs drawn near (next to) the organ of interest at the discretion of the user. Background correction for tumour data of the PVC phantom was complicated due to the following reasons: The

cylindrical shape of the PVC phantom made the choice of location for background correction ROI susceptible to variations in attenuation. Background corrections would have to be made in the same axial direction (z-axis) of the tumour to ensure the same attenuation. Drawing the ROI in this path would result in count contribution (spill-out) from the tumour due to its increased concentration resulting in overestimation of the background contribution. Drawing the ROI further away would require a pixel-to-pixel ACF which would be susceptible to noise. Drawing the ROI further away would result in inclusion of activity from the filling pipes in the posterior view. Thickness variation along a certain axis, experienced with quantification in a cylindrical phantom, requires the incorporation of an effective thickness in the correction of background activity for tumour quantification (Buijs et al., 1998).

3.4 Conclusion.

The performance characteristics used to measure the integrity of the dose calibrator and gamma camera, used during this research project, provided reliable results which indicated this equipment could be used confidently for quantification purposes. The dose calibrator had an accuracy of -0.4% in comparison to measurements made by NMISA. Reproducibility of results showed the dose calibrator to be stable for the ^{99m}Tc setting at 49.4 ± 0.18 MBq during the period of measurements. The small standard deviation in the flood field uniformity measurements indicated that the Symbia T was stable to conduct measurements for this research project. The Symbia T had a high tolerance for count rate performance with count loss of < 1 % for count rates ($\leq$ 10 kcps) used during imaging in this project. Therefore no significant count losses were encountered during investigations.

The PVC phantom resembled the heterogeneous nature of tissues found in clinical studies and represented the tumour geometry found in abdominal [^{123}I]-MIBG clinical studies. This phantom proved to be suitable for ^{99m}Tc planar quantification investigations for the varying geometry with focus on varying: tumour size, tumour-liver distance and the influence of two tumour-background ratios, on quantification accuracy. The quantification accuracy was validated using measurements from the dose calibrator. Acquisitions were performed using default clinical settings as specified by the manufacturer for ^{99m}Tc. The objective of this study did not include optimization of the default settings.

The total counts recorded in the photopeak windows for all the tumour inserts had a percentage error of ≤ 0.5 %; therefore there was minimal affect from noise during

quantification calculations. Room background correction had no influence on the final accuracy of the tumour quantification results. The scatter counts from the tumours obtained from acquisitions using the modified TEW; decreased with decreasing tumour size and increased distance from the liver. It was concluded that the increased GM of counts found for the tumours positioned at 0 cm from the liver was attributed to primary photons and small angle photons originating from the liver. The GM of counts for the tumour-liver distances of 3 cm and 6 cm from the liver were comparable. This demonstrated that scatter from the liver, had minimal effects on tumour quantification accuracy at distances of 3 cm and 6 cm from the liver when the modified TEW scatter correction technique is applied. The method used to perform attenuation correction employed an uncollimated ^{99m}Tc printed transmission source to measure the ACFs. Experimental findings showed that acquisitions for attenuation correction performed at a DTSD of 73 cm resulted in the exclusion of most of the scattered photons from the transmission source. These findings were validated by comparing the measured and expected attenuation results. The measured ACFs for attenuation correction were comparable for repeated measurements. The use of linear attenuation coefficients, measured under broad and narrow beam conditions, as scaling factors used to approximate narrow beam geometry for attenuation correction, for both the tumour quantification data and SCF resulted in minimal effects on quantification accuracy ($\leq$ 1%). This is attributed to the fact that scaling factors were incorporated in the calculation of the tumour data as well as the SCF, measured under the same geometry (for example at DTSD of 73 cm). Measured linear attenuation coefficients measured for water and Perspex underestimated NIST values by 1.9 % and 0.6 % and thus could be reliably used in the quantification process.

Planar quantification accuracies resulted in the least percentage deviation in quantification accuracy for Tumours I and II. This was attributed to the larger tumour sizes that were not near the resolution limit of the gamma camera. The average quantification accuracies for Tumour I and II were -3.3 ± 2.6 % and 5.72 ± 1.1 % respectively. The quantification accuracy was poorer for the smaller tumours near the resolution limit of the gamma camera. The quantified activity for the smaller tumours resulted in average underestimations of 14.7 ± 2.1 % and 29.2 ± 1.3 % for Tumours III and IV respectively. The ROI definition using the physical size of the tumours and the SCF resulted in the smaller tumours being susceptible to spill-out effects due to the PVE, resulting in poor quantification accuracy. PVE compensation, using a larger ROI definition for the SCF and tumours, resulted in quantification accuracies of better than 10 %. The largest percentage difference between the

measured and the quantified activity was observed for Tumour I and IV at -8.2 % and 10.0 % respectively. Additional background activity for tumour-background ratios of 0.5 % and 1.0 %, of tumour activity concentration, resulted in a 4.1 % and 16.6 % contribution in activity overestimation respectively, for calculations without PVE compensation. This overestimation was further increased when PVE was compensated for using larger ROI definitions with contributions of 11.8 % and 26.3 % for the 0.5 % and 1 % ratios respectively.

Differences obtained for quantification accuracies between 3 cm and 6 cm was ≤ 1.8 % for Tumours I to IV, calculated with and without PVE compensation. It can be concluded that scatter from the liver had a minimal effect on tumour quantification accuracy at tumour-liver distances of 3 cm and 6 cm for this geometry.

The results from this study suggest that quantification accuracies of ≤ 10 % for planar images could be obtained using ^{99m}Tc. These results for planar quantification were obtained using standard acquisitions and processing techniques for varying geometry when effects of PVE were compensated for, without significant background activity. These results were in accordance with literature findings (King and Farncombe, 2003; Pereira et al., 2010). From the results of this study it is evident that the effects of scatter from a large radioactive organ, such as the liver, had minimal effects on the quantification accuracy at distances larger than 3 cm from the liver. The planar quantification technique established using ^{99m}Tc was applied to quantification of ^{123}I tumour data, as discussed in Chapter 4.

References

Bombardieri, E., Aktolun, C., Baum, R.P., Bishof-Delaloye, A., Buscombe, J., Chatal, J.F., Maffioli, L., Moncayo, R., Mortelmans, L., Reske, S.N., 2003. $^{131}I/^{123}I$-Metaiodobenzylguanidine (MIBG) scintigraphy: procedure guidelines for tumour imaging. Eur. J. Nucl. Med. Mol. Imaging 30, B132–B139.

Brindha, S., Venning, A.J., Hill, B., Baldock, C., 2004. Experimental study of attenuation properties of normoxic polymer gel dosimeters. Phys. Med. Biol. 49, N353–361.

Brown, S., Bailey, D.L., Willowson, K., Baldock, C., 2008. Investigation of the relationship between linear attenuation coefficients and CT Hounsfield units using radionuclides for SPECT. Appl. Radiat. Isot. 66, 1206–1212.

Buijs, W.C., Siegel, J.A., Boerman, O.C., Corstens, F.H., 1998. Absolute organ activity estimated by five different methods of background correction. J. Nucl. Med. 39, 2167–2172.

Fielding, S.L., Flower, M.A., Ackery, D., Kemshead, J.T., Lashford, L.S., Lewis, I., 1991. Dosimetry of iodine 131 metaiodobenzylguanidine for treatment of resistant neuroblastoma: results of a UK study. Eur. J. Nucl. Med. 18, 308–316.

Geldenhuys, E.M., Lötter, M.G., Minnaar, P.C., 1988. A New Approach to NEMA Scintillation Camera Count Rate Curve Determination. J. Nucl. Med. 29, 538–541.

He, B., Du, Y., Song, X., Segars, W.P., Frey, E.C., 2005. A Monte Carlo and physical phantom evaluation of quantitative In-111 SPECT. Phys. Med. Biol. 50, 4169–4185.

Hoffman, E.J., Huang, S.C., Phelps, M.E., 1979. Quantitation in positron emission computed tomography: 1. Effect of object size. J. Comput. Assist. Tomogr. 3, 299–308.

Hubbell, J. H., Seltzer S. M., 2004. Tables of X-ray Mass Attenuation Coefficients and Mass Energy-Absorption Coefficients from 1 keV to 20 MeV for elements Z = 1 to 92 and 48 Additional substances of Dosimetric Interest. National Institute of Standards and Technology, Gaithersburg, MD (Available at <: http://www.nist.gov/pml/data/xraycoef/ > (accessed 17.09.13).

Ichihara, T., Ogawa, K., Motomura, N., Kubo, A., Hashimoto, S., 1993. Compton scatter compensation using the triple-energy window method for single- and dual-isotope SPECT. J. Nucl. Med. 34, 2216–2221.

Jaszczak, R.J., Greer, K.L., Floyd, C.E., Jr, Harris, C.C., Coleman, R.E., 1984. Improved SPECT quantification using compensation for scattered photons. J. Nucl. Med. 25, 893–900.

King, M., Farncombe, T., 2003. An overview of attenuation and scatter correction of planar and SPECT data for dosimetry studies. Cancer Biother. Radiopharm. 18, 181–190.

Kojima, A., Matsumoto, M., Takahashi, M., 1991. Experimental analysis of scattered photons in Tc-99m imaging with a gamma camera. Ann. Nucl. Med. 5, 139–144.

Kojima, A., Matsumoto, M., Takahashi, M., Uehara, S., 1993. Effect of energy resolution on scatter fraction in scintigraphic imaging: Monte Carlo study. Med. Phys. 20, 1107–1113.

Ljungberg, M., King, M.A., Hademenos, G.J., Strand, S.E., 1994. Comparison of four scatter correction methods using Monte Carlo simulated source distributions. J. Nucl. Med. 35, 143–151.

Macey, D.J., DeNardo, G.L., DeNardo, S.J., 1999. Planar gamma camera quantitation of ^{123}I, ^{99m}Tc or ^{111}In in the liver and spleen of an abdominal phantom. Cancer Biother. Radiopharm. 14, 299–306.

Minarik, D., Sjögreen, K., Ljungberg, M., 2005. A new method to obtain transmission images for planar whole-body activity quantification. Cancer Biother. Radiopharm. 20, 72–76.

National Electrical Manufacturers Association, 2007. NEMA NU 1 Perfomance Measurements of Gamma Cameras.

Ng, A.H., Ng, K.H., Dharmendra, H., Perkins, A.C., 2009. A low-cost phantom for simple routine testing of single photon emission computed tomography (SPECT) cameras. Appl. Radiat. Isot. Data Instrum. Methods Use Agric. Ind. Med. 67, 1864–1868.

Norrgren, K., Svegborn, S.L., Areberg, J., Mattsson, S., 2003. Accuracy of the quantification of organ activity from planar gamma camera images. Cancer Biother. Radiopharm. 18, 125–131.

Ogawa, K., Harata, Y., Ichihara, T., Kubo, A., Hashimoto, S., 1991. A practical method for position-dependent Compton-scatter correction in single photon emission CT. IEEE Trans. Med. Imaging 10, 408–412.

Olivier, P., Colarinha, P., Fettich, J., Fischer, S., Frökier, J., Giammarile, F., Gordon, I., Hahn, K., Kabasakal, L., Mann, M., Mitjavila, M., Piepsz, A., Porn, U., Sixt, R., van Velzen, J., 2003. Guidelines for radioiodinated MIBG scintigraphy in children. Eur. J. Nucl. Med. Mol. Imaging 30, B45–50.

Pereira, J.M., Stabin, M.G., Lima, F.R.A., Guimarães, M.I.C.C., Forrester, J.W., 2010. Image quantification for radiation dose calculations--limitations and uncertainties. Health Phys. 99, 688–701.

Perkins, A.C., Clay, D., Lawers, S.C., 2007. A simple low cost phantom for the quality control of SPECT cameras. World J. Nucl. Med. 6, 35.

Sjögreen, K., Ljungberg, M., Wingårdh, K., Minarik, D., Strand, S.-E., 2005. The LundADose method for planar image activity quantification and absorbed-dose assessment in radionuclide therapy. Cancer Biother. Radiopharm. 20, 92–97.

Soret, M., Bacharach, S.L., Buvat, I., 2007. Partial-volume effect in PET tumor imaging. J. Nucl. Med. Off. Publ. Soc. Nucl. Med. 48, 932–945.

Trapp, J.V., Michael, G., de Deene, Y., Baldock, C., 2002. Attenuation of diagnostic energy photons by polymer gel dosimeters. Phys. Med. Biol. 47, 4247–4258.

Van Staden, J.A., du Raan, H., Lötter, M.G., Herbst, C.P., van Aswegen, A., Rae, W.I.D., 2011. Evaluation of an uncollimated printed paper transmission source used under scatter limiting conditions. Phys. Medica PM Int. J. Devoted Appl. Phys. Med. Biol. 27, 11–20.

Van Staden, J.A., du Raan, H., Lötter, M.G., van Aswegen, A., Herbst, C.P., 2007. Production of radioactive quality assurance phantoms using a standard inkjet printer. Phys. Med. Biol. 52, N329–337.

Zaidi, H., Koral, KF., 2005. METHODS FOR PLANAR IMAGE QUANTIFICATION. In: "*Quantitative analysis in nuclear medicine imaging"*. New York: Kluwer Academic/Plenum Publishers, USA. pp 414–431.

4. IODINE-123 ACTIVITY QUANTIFICATION.

4.1 Introduction.

[^{131}I]-MIBG is used for therapeutic treatment of neuroendocrine tumours such as phaeochromocytomas and neuroblastomas. MIBG is used to target adrenal tumours, relying on the fact that these tumours are functioning tumours following a medullary pathway (Rubello et al., 2002). However, prior to therapeutic treatment with [^{131}I]-MIBG, [^{123}I]-MIBG is used as a diagnostic scan to locate these tumours. ^{123}I is used as a diagnostic predictive scan due to its better imaging properties, which include high specificity and sensitivity for these tumours in comparison to ^{131}I (Vik et al., 2009). The ability of iodine to covalently bind to diverse molecules makes it an ideal candidate for the radio-labelling of many substances such as antibodies and neurotransmitters (Darcourt et al., 2010; Sgouros et al., 2003). ^{123}I has favourable imaging characteristics which include; the emission of its main γ-ray with a mean energy of 159 keV and a yield of 83 % and a relatively short half life of 13.2 hours. However, ^{123}I also has γ-rays of higher energy emissions with low yield, with an average energy of 507 keV. Although ^{123}I has favourable imaging characteristics, it is produced in a cyclotron and is less readily available and more expensive in comparison to ^{99m}Tc. ^{123}I used in this study, was supplied by iThemba Labs in Cape Town, South Africa.

4.2 Materials and Methods.

The quantification technique established in Chapter 3, for planar quantification of ^{99m}Tc tumour data, was applied in this Chapter for planar quantification of the ^{123}I tumour data. Some modifications were made to the acquisition and processing protocols to take into account physical differences between ^{99m}Tc and ^{123}I.

4.2.1 Dose calibrator performance characteristics.

The importance of equipment stability for quantification purposes was discussed in Chapter 2, Section 3.2.1. Tumour quantification accuracy was made with reference to activity measurements in the dose calibrator. Therefore, dose calibrator performance characteristics were determined for the ^{123}I setting, with regard to accuracy and reproducibility.

a) Dose calibrator accuracy.

The dose calibrator accuracy was also established in the research project “Intercomparison of Nuclear Medicine isotopes calibrators in the Bloemfontein Area”. The percentage difference

between the measurement for ^{123}I made by NMISA and that obtained using the Capintec CRC-15R dose calibrator in our clinic was obtained.

b) Dose calibrator reproducibility.

The stability of the accuracy established above was ensured through measurements using the long lived radionuclide ^{137}Cs, for the ^{123}I radionuclide setting of the dose calibrator. This procedure was repeated daily in accordance with phantom acquisitions over a period from May 2013 until June 2013. Periodicity was determined by the availability of ^{123}I for phantom measurements. The average apparent activity value and standard deviations were calculated from these measurements.

4.2.2 Data acquisition.

Phantoms described in Chapter 3, Section 3.2.2 were used for acquisitions of ^{123}I quantification data and prepared accordingly. The same acquisition protocol was followed (Chapter 3, Section 3.2.3.2) with modifications for ^{123}I data quantification. The TEW scatter correction method was used for the acquisitions with energy windows set to 15 % of the photopeak energy, as specified by the manufacturer of the Symbia T software package (Syngo MI Applications 2007A; Siemens Healthcare). The selected energy windows settings were set to 121.0 – 144.4 keV, 144.4 – 167.8 keV and 167.8 – 191.3 keV for the lower scatter sub-window (placed below the photopeak window), photopeak window and the upper scatter sub-windows (placed above the photopeak window) respectively, with a scatter weighting factor of 0.5. All three energy window settings had equivalent widths of 23.4 keV. All data were acquired with a percentage uncertainty of < 1 %.

As discussed in Chapter 2, Section 2.6, both the low energy high resolution (LEHR) and medium energy (ME) collimators have been used for imaging with ^{123}I. The LEHR collimators are optimised for the γ-ray energy of ^{99m}Tc (140 keV), and have been used for imaging with ^{123}I (159 keV) energy with the notion that the main γ-ray energy of the two radionuclides is not too far apart. However, ^{123}I has higher energy emissions which must be taken into consideration for appropriate collimator choice. These higher energy emissions have been found to result in increased septal penetration when imaging with [^{123}I]-MIBG using a LEHR (Snay et al., 2011). It was reported in this study that the choice of the ME collimator for imaging with [^{123}I]-MIBG resulted in improved image quality for both SPECT

and planar images. Downscatter into the photopeak, experienced from higher energy emissions of ^{123}I, has been found to contribute to 39 % of the γ-rays detected in the photopeak window when imaging with a LEHR collimator (Du et al., 2006). The use of the ME collimator with thicker septa reduces the fraction of the higher energy γ-rays, which result in septal penetration and thus are scattered into the photopeak. The use of the ME collimator for ^{123}I has been reported to improve image contrast due to decreased septal penetration.

There has been debate in the literature regarding collimator choice (ME vs. LEHR) for imaging with ^{123}I depending on the end use of the images i.e. whether it is for quantification purposes or improved image quality. For that reason, collimator choice for ^{123}I imaging, for the purpose of this project, was validated visually in a qualitative comparison of [^{123}I]-MIBG static images of a patient acquired using a LEHR and ME collimator on the Symbia T in our clinic.

4.2.3 Data processing.

Parameters for tumour activity quantification were calculated as shown in Chapter 3, Section 3.2.4 and modified for the ^{123}I data as shown in Equation 4.1. The individual parameters shown in Equation 4.1 are the same as those described for Equation 3.1, in Chapter 3 with introduction of additional scaling factors described below.

$$Quantified\ Activity(MBq) = \frac{\frac{\sqrt{C_A \times C_P}}{t} \times ACF_{BB\_^{99m}Tc\_water} \times Wk_1 \times Wk_2 \times Wk_3}{\frac{\sqrt{C_{AP} \times C_{PP}}}{A \times t} \times ACF_{BB\_^{99m}Tc\_Perspex} \times Pk_1 \times Pk_2 \times Pk_3} \qquad \textbf{4. 1}$$

where:

- C_A and C_P are the anterior and posterior primary counts obtained from the ROI defining the tumour radioactivity distributions. The primary counts were calculated using the counts recorded in the photopeak window corrected for decay, room background and scatter.
- t is the acquisition time which was kept constant at 15 minutes for all acquisitions.
- A is the radioactivity of the printed radioactive disk as measured in the dose calibrator.

- $ACF_{BB\_}{}^{99m}{}_{Tc\_water}$ and $ACF_{BB\_}{}^{99m}{}_{Tc\_Perspex}$ are the attenuation correction factors (ACF) measured under broad beam conditions modified for minimal scatter inclusion for water and Perspex measurements respectively.
- $Wk_{1\text{-}3,}$ where $i = 1...3$ are the scaling factors for water measurements introduced in the ACF for attenuation correction of the PVC phantom tumour data, discussed in detail in Section 4.2.3.4.2 (a).
- $Pk_{1\text{-}3,}$ where $i = 1...3$ are the scaling factors for Perspex measurements introduced in the ACF for attenuation correction of the Perspex data for the system calibration factor (SCF), discussed in Section 4.2.3.4.2(b).
- The denominator shown in Equation 4.1 represents the SCF measured in Perspex. C_{AP} and C_{PP} are the anterior and posterior primary counts of the SCF obtained, from the ROI defining the printed disk radioactivity distribution, discussed in Section 4.2.3.5. The primary counts were calculated using the counts recorded in the photopeak window corrected for decay, room background and scatter.

All data were acquired at count rates with negligible count losses (< 1 %) for both detector one and two.

4.2.3.1 Region of interest definition.

Acquisitions using the TEW scatter correction technique resulted in simultaneous acquisition of images in the lower scatter sub-window, photopeak and higher scatter sub-windows respectively as shown in Figure 4-1. Saved ROIs, drawn according to the physical dimensions of the four tumours, were used to obtain image counts (Figure 4-1). These ROIs did not take partial volume effects (PVE) into consideration. All counts were corrected for decay (to specific time reference) and room background, as discussed in Chapter 3 (Section 3.2.4.1). The contribution (percentage) of the room background counts on the total counts recorded in the photopeak is reported.

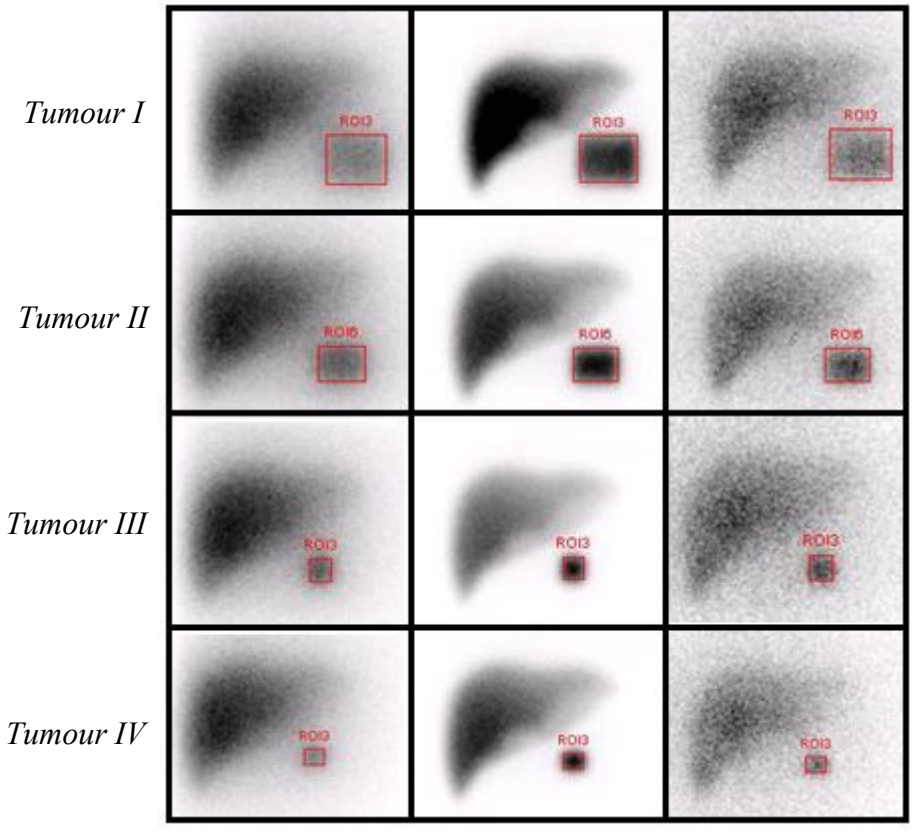

Figure 4-1: *Examples of regions of interest used for quantification of Tumour I to IV shown in top to bottom rows respectively, measured at a tumour-liver distance of 3 cm. Anterior images recorded in the; (a) lower scatter sub-window (b) photopeak window (c) higher scatter sub-window.*

4.2.3.2 Scatter correction using the triple energy window.

The total counts recorded in the photopeak window consisted of both the primary and scatter counts. Scatter correction was applied, prior to the GM calculation, using the TEW scatter correction technique, as shown in Equation 4. 2.

$$C_{TEW} = \left(\frac{C_{lower}}{W_{lower}} + \frac{C_{higher}}{W_{higher}} \right) \times \frac{W_{photooeak}}{2} \qquad \textbf{4. 2}$$

where: C_{TEW} is the scatter count estimate within the photopeak window calculated using the TEW scatter correction technique, C_{lower} and C_{higher} are the counts in the lower and higher sub-windows respectively, W_{lower} and W_{higher} are the heights of the lower and higher sub-windows respectively in counts per keV and $W_{photopeak}$ is the width of the photopeak window. The primary counts ($C_{primary}$) in the photopeak window were calculated using Equation 4.3.

$$C_{primary} = C_{photopeak} - C_{TEW} \quad \textbf{4. 3}$$

The average scatter fraction (expressed as the GM of the anterior and posterior counts) was calculated using Equation 4.4 and plotted for each tumour, for the tumour-liver distances of 0 cm, 3 cm and 6 cm.

$$SF = \frac{C_{TEW}}{C_{primary}} \quad \textbf{4. 4}$$

4.2.3.3 Geometric mean.

The GM of the scatter corrected anterior and posterior primary counts was calculated using Equation 4.5. The GM of the scatter corrected counts for one set of measurement for Tumour I to IV is reported.

$$GM = \sqrt{C_A \times C_P} \quad \textbf{4. 5}$$

4.2.3.4 Attenuation correction.

Due to the high cost, unavailability and supply problems experienced with ^{123}I, measurements of transmission images, for attenuation correction factors (ACFs) were performed using ^{99m}Tc. Linear attenuation coefficients could not be measured with ^{123}I and thus were obtained from the National Institute of Standards and Technology (NIST), USA published data (Hubbell and Seltzer, 2004). The necessary scaling factors were introduced to account for these discrepancies.

4.2.3.4.1 Attenuation correction factor for tumour quantification.

As established in Chapter 3, Section 3.2.4.4, an ACF (Equation 4.6) calculated from blank and transmission images was used for attenuation correction. These images were acquired using an uncollimated ^{99m}Tc printed transmission source measured at a detector transmission source distance (DTSD) of 73 cm. The results for the average ACF, for Tumour I to IV, measured over a period of three weeks are reported.

$$ACF = \sqrt{\frac{C_{Blank}}{C_{transmission}}} \quad \textbf{4. 6}$$

4.2.3.4.2 Scaling factors.

Linear attenuation coefficients were used for three reasons, each of which is explained by the three scaling factors shown in Equation 4.1. Scaling factors denoted by $Wk_{1\text{-}3}$ and $Pk_{1\text{-}3}$ refer to scaling factors obtained from water and Perspex measurements respectively. Wk_1 was the scaling factor used to account for the difference between linear attenuation coefficients tabulated by NIST and those measured during this project. As established in Chapter 3, Section 3.2.4.4.3 there are differences in linear attenuation coefficients between the published theoretical values, those published by NIST, and those measured in the clinical environment (Brown et al., 2008; Cherry et al, 2003). Wk_2 accounted for the difference found between the linear attenuation coefficients measured under broad beam and those measured under narrow beam conditions. This takes into account the fact that the GM was calculated using scatter corrected data. This entails that attenuation correction should be performed using narrow beam data. Wk_3 was used to account for the energy difference between ^{99m}Tc (used to measure the ACF) and ^{123}I (used for emission data) (Minarik et al., 2005). The values for these scaling factors were calculated as shown below.

a) Scaling factors for water.

$$Wk_1 = \frac{\mu_{NIST\_NB\_^{99m}Tc}}{\mu_{Measured\_NB\_^{99m}Tc}} \qquad Wk_2 = \frac{\mu_{Measured\_NB\_^{99m}Tc}}{\mu_{Measured\_BB\_^{99m}Tc}} \qquad Wk_3 = \frac{\mu_{NIST\_NB\_^{123}I}}{\mu_{NIST\_NB\_^{99m}Tc}}$$

where:

- $\mu_{NIST\_NB\_^{99m}Tc}$ and $\mu_{Measured\_NB\_^{99m}Tc}$ are the linear attenuation coefficients of ^{99m}Tc measured under narrow beam geometry for NIST and measurements on the Symbia T respectively.
- $\mu_{Measured\_BB\_^{99m}Tc}$ is the linear attenuation coefficient for ^{99m}Tc measured under broad beam conditions, modified for minimal scatter inclusion (measurement done at DTSD of 73 cm).
- $\mu_{NIST\_NB\_^{123}I}$ is the linear attenuation coefficient for ^{123}I obtained from NIST published data.

b) Scaling factors for Perspex.

The above mentioned scaling factors were also applied to the SCF as shown in the denominator of Equation 4.1. Therefore, equivalent scaling factors were also introduced for Perspex.

$$Pk_1 = \frac{\mu_{NIST\_NB\_^{99m}Tc}}{\mu_{Measured\_NB\_^{99m}Tc}} \qquad Pk_2 = \frac{\mu_{Measured\_NB\_^{99m}Tc}}{\mu_{Measured\_BB\_^{99m}Tc}} \qquad Pk_3 = \frac{\mu_{NIST\_NB\_^{123}I}}{\mu_{NIST\_NB\_^{99m}I}}$$

4.2.3.5 System calibration factor.

The SCF was measured using a flat printed radioactive disk of ±18 MBq of ^{123}I similar to that described for ^{99m}Tc in Chapter 3, Section 3.2.4.5. The radioactive disk was placed within 17.3 cm of Perspex. The SCF was calculated using Equation 4.7.

$$SCF\ (cps/MBq) = \frac{\sqrt{C_{AP} \times C_{PP}} \times ACF_{BB\_^{99m}Tc\_Perspex} \times Pk_1 \times Pk_2 \times Pk_3}{A(MBq) \times t(s)} \qquad \textbf{4. 7}$$

where: C_{AP} and C_{PP} are the anterior and posterior counts measured in Perspex corrected for room background and scatter and decay to the time of the printed disk radioactivity measurement in the dose calibrator, $ACF_{BB\_^{99m}Tc\_Perspex}$ is the ACF measured for Perspex at DTSD of 73cm. The $ACF_{BB\_^{99m}Tc\_Perspex}$ was calculated using Equation 4.6 and scaled as described above (Section 4.2.3.4.2(b)). The SCF was analyzed, with (using 10 % and 30 % window level) and without (from physical dimensions of the printed disk) PVE compensations as described in Chapter 3 (Section 3.2.4.5). A plot of the average results of the SCF, for three different days of measurements, is reported.

4.2.3.6 Tumour activity quantification.

Tumour activity was calculated using Equation 4.1 and the same data processing techniques were applied to both tumour quantification data and SCF data as discussed in Sections 4.2.3.1 to 4.2.3.5. Data processing, in accordance with Equation 4.1 was as described in Chapter 3, Section 3.2.4.6 with the introduction of the above mentioned scaling factors. Tumour activity quantification accuracy was calculated with and without PVE compensation.

Tumour activity quantification using ^{123}I investigated two variables of this research project namely; varying tumour sizes (i.e. Tumour I to IV) and the tumour-liver distances of 0 cm, 3 cm and 6 cm. The average results of three sets of data, measured on different days, are reported.

4.2.3.6.1 Quantification without compensation for partial volume effects.

Tumour quantification was first analysed according to physical dimensions of the tumours and SCF (as described in Chapter 3, Section 3.2.4.6.1(a)), and thereby excluding PVE. This method was initially established as a standard method for ROI definition for this research project.

4.2.3.6.2 Quantification with compensation for partial volume effects.

PVE was compensated for by the ROI definition applicable to both tumour and SCF data. The criterion for ROI definition was to include the majority of primary counts with good separation between the liver and tumour, as described in Chapter 3, section 3.2.4.6.1(b) (Zaidi and Koral, 2005). This was achieved by adjusting the window level to 30 % of maximum count for Tumour I and 10 % of maximum counts for Tumour II to IV.

4.3 Results and Discussions.

4.3.1 Dose calibrator performance characteristics.

a) Dose calibrator accuracy

The Capintec CRC-15R dose calibrator used in this study underestimated the ^{123}I activity measured by NMISA, with a percentage difference of 5.2 %. Several possible causes for this difference have been mentioned in Chapter 3, Section 3.3.1.1. However differences in ionization chambers and measurement geometry used by the NMISA and our clinic are also a possible cause. This underestimation was incorporated into the quantification process using the SCF (i.e. the SCF will have a bias value due to the inaccuracy of the dose calibrator) and therefore did not affect the quantification accuracy. This underestimation of ^{123}I measurements with the dose calibrator in our clinic should be considered in the case of patient administration.

b) Dose calibrator reproducibility.

Figure 4-2 shows the radioactivity measurements obtained with the ^{137}Cs source measured for the ^{123}I radionuclide setting of the dose calibrator. The average radioactivity value calculated for the different days of measurements was 22.4 ± 0.19 MBq, indicating a small variation for the different days of measurement. This served as an indication that the dose calibrator was stable during the period of measurements and could reliably be used for quantification purposes.

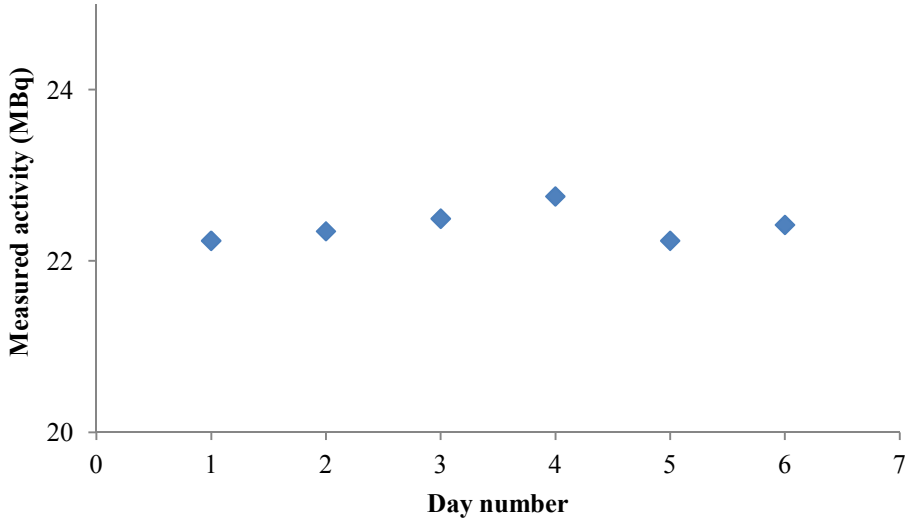

Figure 4-2: *The Capintec CRC-15R dose calibrator reproducibility for the different days of measurements using ^{137}Cs.*

4.3.2 Data acquisition.

Qualitative comparison between the static images of a [^{123}I]-MIBG patient acquired using the LEHR and ME collimators is shown in Figure 4-3. The quality of the image acquired with the ME collimator was observed to be enhanced as a result of less scatter due to less septal penetration. Less scatter in the patient image acquired with the ME collimator improved the image contrast and led to better separation between the liver and heart (Figure 4-3). There is also a clear distinction of increased background with the LEHR collimator which is attributed to septal penetration. The ME collimator presented improved contrast with low count statistics (48 k) in comparison to the counts statistics of the image acquired with the LEHR collimator (110 k). This is an indication that the ME collimator would result in better delineation of organs of interest for quantification purposes. This was in accordance with

literature findings that imaging with [^{123}I]-MIBG using ME collimator resulted in better image quality in comparison to the LEHR (Snay et al., 2011). These findings confirm the choice of the ME collimator for quantitative imaging with ^{123}I for this research project, attributed to improved image quality (Bolmsjö et al., 1977; DeNardo et al., 1985; Macey et al., 1986).

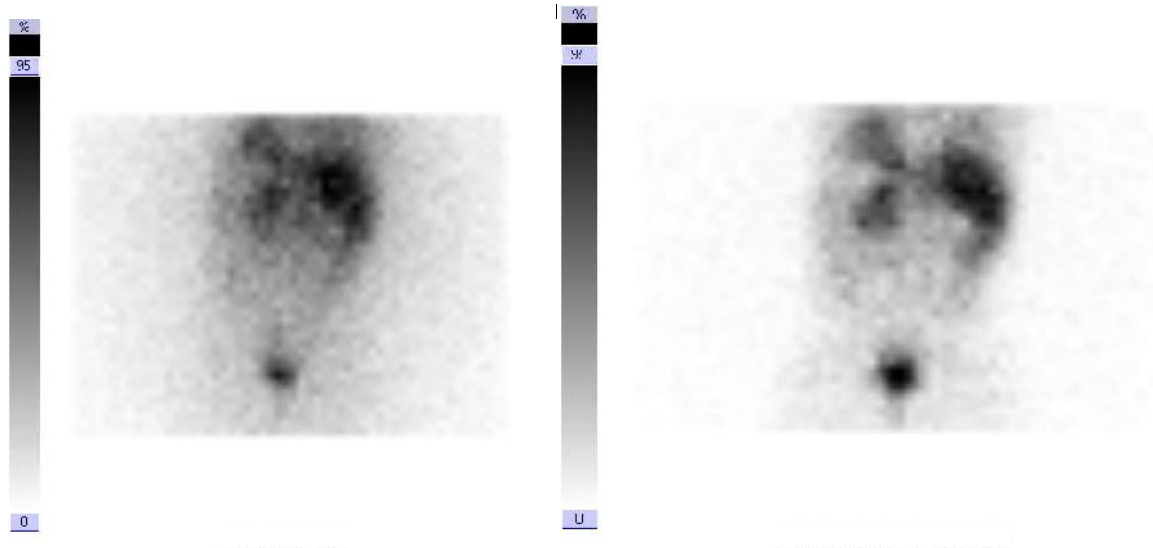

(a) ***(b)***

Figure 4-3: *Clinical example of qualitative comparison of [^{123}I]-MIBG static images acquired using the Symbia T SPECT/CT (Siemens Medical Solutions USA, Inc.) in the Department of Nuclear Medicine at Universitas Hospital using: (a) low energy high resolution collimator (110 k counts) (b) medium energy collimator (48 k counts).*

4.3.3 Data processing.

4.3.3.1 Region of interest definition.

The percentage uncertainty for the total counts recorded in the photopeak window for anterior and posterior views, for all tumours, was < 1 % (See Appendix B, Table B1-B4). This small statistical variation is also observed for the smallest tumour, defined by a small ROI, due to increased concentration. Room background counts were small (< 0.3 %) in comparison to counts recorded in three windows and had negligible effects on the final quantification.

4.3.3.2 Scatter correction using the triple energy window.

Figure 4-4 shows the three energy windows used to acquire the ^{123}I spectrum using Tumour I. This energy spectrum illustrates a considerable scatter component (indicated by the yellow

arrow) included in the higher scatter sub-window due to high energy γ-ray emission. This indicates the need for a lower as well as a higher scatter sub-window when using the TEW scatter correction technique for imaging with ^{123}I. Evident from the spectrum is also the high energy γ-rays that form a peak between 500 keV and 550 keV (indicated by the blue arrow), discussed in Chapter 2 (Section 2.6).

Figure 4-4: *An acquired energy spectrum for ^{123}I with a photopeak energy window (A) and lower scatter energy sub-window (B) and a higher scatter energy sub-window (C).*

A plot of the GM of the scatter fraction counts is shown in Figure 4-5. The average scatter ratio for Tumour I to IV was 0.26 ± 0.02, 0.20 ± 0.01, 0.18 ± 0.02 and 0.17 ± 0.02 respectively, for the tumour-liver distances of 0 cm, 3 cm and 6 cm. The scatter contribution, increased with increasing tumour size which was in accordance with literature findings (Kojima et al., 1991). Scatter to primary counts contribution was 26 % and 17 % for Tumour I and IV respectively. This indicated a 9 % difference in scatter contributions between the largest (Tumour I) and smallest tumour (Tumour IV). The scatter fraction decreased with increased tumour-liver distance and this is attributed to the exclusion of scatter contribution from the liver at increased distances.

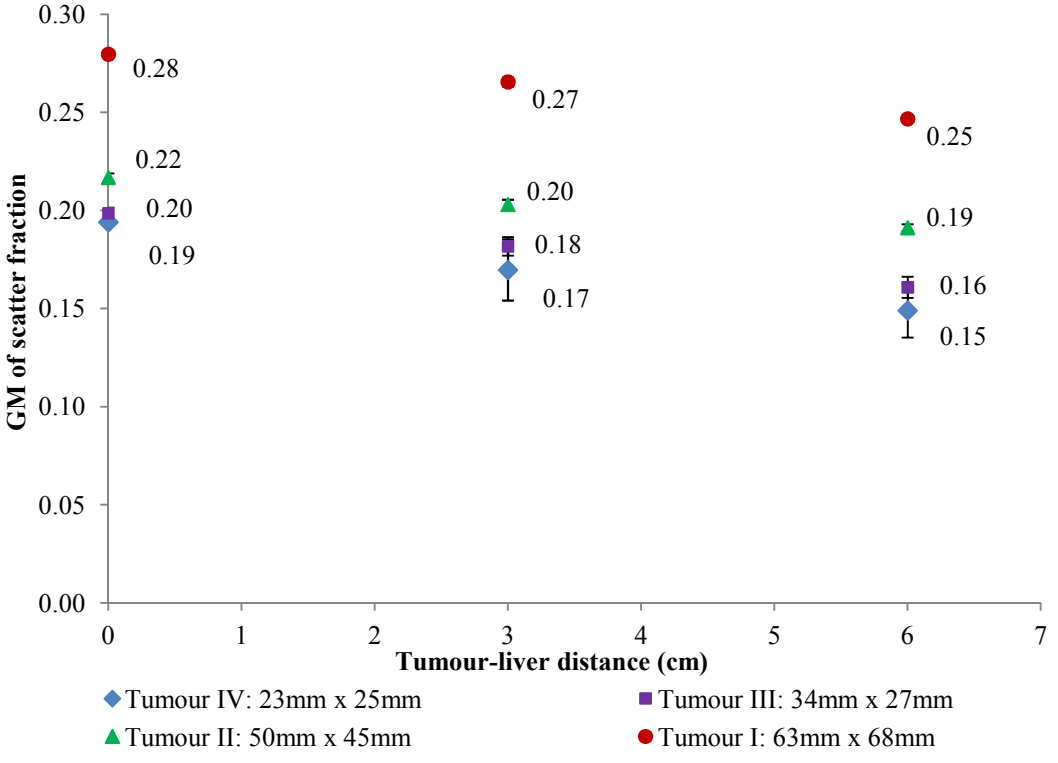

Figure 4-5: *The geometric mean of the average scatter fraction values obtained during different days of measurement for Tumour I to IV as a function of tumour-liver distance.*

4.3.3.3 Geometric mean.

Table 4-1 shows the GM of the scatter corrected counts for one set of measurements for Tumour I to IV. The counts obtained from the tumour at 0 cm distance from the liver were increased in comparison to the two greater distances. This marked increase in counts at 0 cm can be attributed to the fact that the liver slightly overlay all tumours at this distance. Thus primary counts and small angle scatter counts (counts included in the photopeak window) from the liver were included in the ROI definitions (Figure 4-6) of all tumours, as it was not possible to distinguish between primary counts from the tumour and those from the liver. This is due to the underlying liver activity in the projection of the tumour, present due to the nature of planar imaging. There was a comparable difference of 4.4 ± 0.24 % for all the tumours, where the difference in counts obtained at 0 cm and 6 cm was expressed as a percentage of the total counts obtained at 0 cm.

Table 4-1: *The geometric mean of counts corrected for room background and scatter for Tumour I to IV at different tumour-liver distances.*

Tumour-liver distance (cm)	Tumour I	Tumour II	Tumour III	Tumour IV
0	269158	226035	102456	53203
3	257620	218214	100762	51331
6	257164	216848	98027	50731

The effect of scatter was expected to have minimal influence on the GM of counts since the TEW scatter correction technique was applied to the acquired data. This correction for the scatter contribution at 3 cm and 6 cm distances was observed in the comparable counts obtained at 3 cm and 6 cm as shown in Table 4-1. The percentage difference between the number of counts obtained at distances of 3 cm and 6 cm from the liver was found to be 1.17 ± 1.11 %, where the difference in counts obtained at 3 cm and 6 cm was expressed as a percentage of the total counts obtained at 3 cm. Similar trends were seen for all three sets of data.

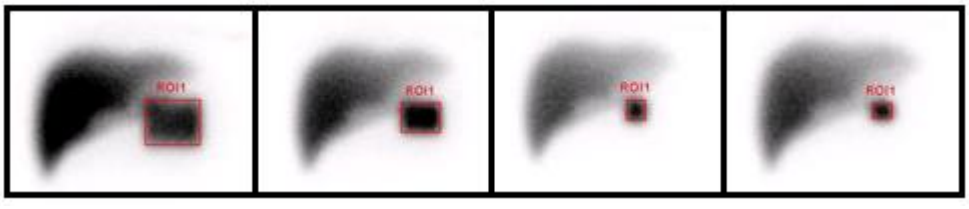

Figure 4-6: *Examples of regions of interest used for quantification of Tumour I to IV respectively, at tumour-liver distance of 0 cm.*

4.3.3.4 Attenuation correction.

4.3.3.4.1 Attenuation correction factor for tumour quantification.

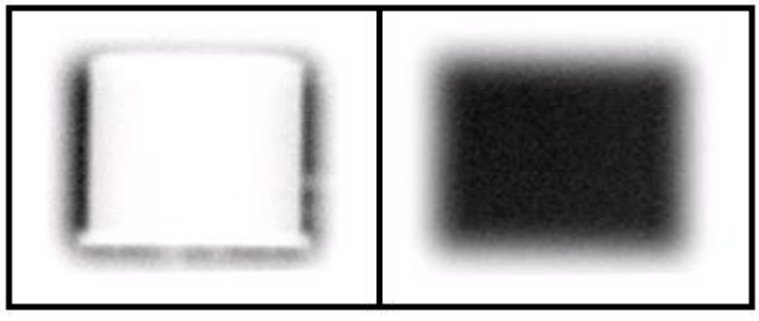

(a) ***(b)***

Figure 4-7: *Examples of images used to calculate the attenuation correction factor; (a) transmission (b) blank images.*

Examples of images used to calculate the ACF for quantification of Tumour I to IV, at various tumour-liver distances, are shown in Figure 4-7. The average ACF results for the four tumours are shown in Table 4-2 (See Appendix B, Table B5). The ACF was comparable for all the different size tumours for reasons discussed in Chapter 3 (Section 3.3.3.4.2). The small standard deviation indicated that there was a small difference for the ACF measured at the various tumour-liver distances. This was attributed to the fact that the attenuation for all the tumours at these distances was at the similar thickness. The ACF resulted in a 10-fold increase in the tumour GM of counts, emphasizing the importance of applying attenuation correction for quantification of the tumour data.

Table 4-2: *The average attenuation correction factors for different tumour sizes measured at the various tumour-liver distances.*

	$ACF_{Tumour\ I}$	$ACF_{Tumour\ II}$	$ACF_{Tumour\ III}$	$ACF_{Tumour\ IV}$
Average	9.51 ± 0.09	9.83 ± 0.05	10.03 ± 0.07	9.95 ± 0.10

4.3.3.4.2 Scaling factors.

Scaling factors mentioned in Section 4.2.3.4.2 are shown in Table 4-3. The first scaling factor (k_1) accounts for the fact that measurements on the Symbia T gamma camera were not measured under ideal narrow beam conditions. The value for k_1 is > 1 and indicates the extent to which scatter was included in the measurement geometry in comparison to measurements by NIST. The second scaling factor (k_2) accounts for the difference between values measured on the Symbia T under narrow beam and broad beam conditions. Similarly, $k_2 > 1$ accounting for the extent to which scatter has altered the transmission of γ-rays through the uniform water bath phantom. The third scaling factor (k_3) which accounts for energy differences between the emission (^{123}I) and transmission (^{99m}Tc) isotopes is < 1 indicating that the ^{123}I γ-rays were less attenuated in comparison to the ^{99m}Tc γ-rays which is attributed to the energy difference between ^{99m}Tc an ^{123}I. As indicated in Equation 4.1 scaling factors for both the tumour data (Wk_{1-3}), and that of the SCF (Pk_{1-3}), are used to obtain the tumour quantified data. This resulted in tumour activity being multiplied by a factor of 1.021 which had a minimal effect (< 2 %) on the final quantification accuracy. This is expected as the ACF and the SCF were measured under minimal scatter conditions, by increasing the DTSD to 73 cm.

Table 4-3: *Scaling factors used for attenuation correction of phantom and system calibration factor data.*

Measurement	**k_1**	**k_2**	**k_3**
Water (Wk_{1-3})	1.023	1.039	0.955
Perspex (Pk_{1-3})	1.006	1.029	0.960

4.3.3.5 System calibration factor.

(a) *(b)* *(c)*

Figure 4-8: *Examples of anterior images, with superimposed regions of interest drawn according to the physical dimensions of the printed radioactive disk, acquired for the system calibration factor. Images recorded in the; (a) lower scatter (b) photopeak and (c) higher scatter windows.*

Examples of anterior images, superimposed with a ROI drawn according to the physical size of the printed disk, used in quantification of the SCF are shown in Figure 4-8. The average SCF obtained from the ROI drawn according to the physical dimensions of the printed disk was 73.95 ± 1.04 cps/MBq. Results for the SCF obtained using the 30 % and 10 % window level adjustment was 79.43 ± 0.60 cps/MBq and 83.41 ± 0.30 cps/MBq respectively. Larger ROI definitions resulted in the inclusion of more counts in comparison to ROI defined by the physical dimensions of the radioactive disk, which is indicated by a higher SCF. The SCF factor was stable for the different days of measurement.

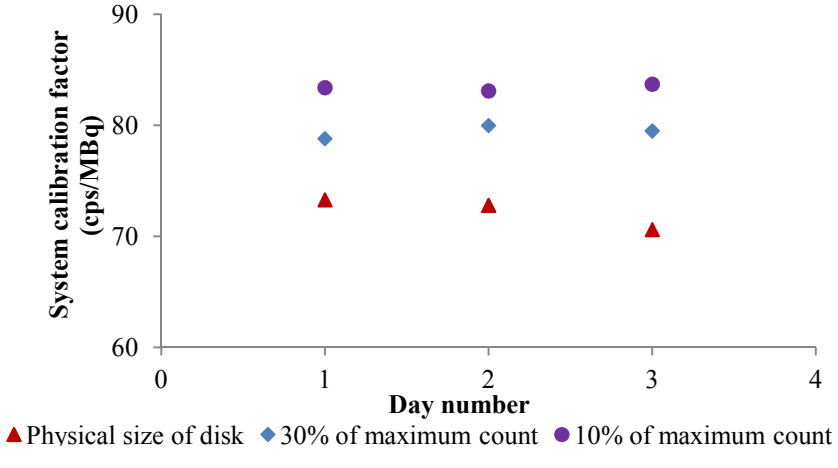

Figure 4-9: *System calibration factor measured in Perspex used in the calculation of tumour activity quantification data.*

4.3.3.6 Tumour activity quantification.

4.3.3.6.1 Quantification without compensation for partial volume effects.

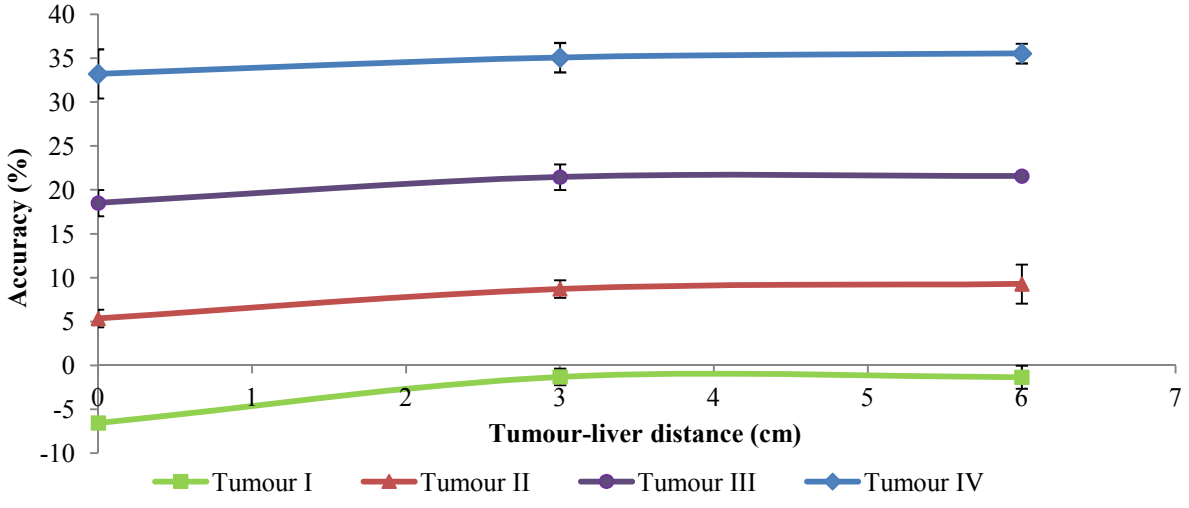

Figure 4-10: *^{123}I activity quantification accuracy for Tumour I to IV without compensation for partial volume effects.*

❖ **Varying tumour sizes.**

Figure 4-10 shows the results obtained for tumour quantification accuracy, of the different tumour sizes, as a function of tumour-liver distance without compensation for PVE (See Appendix B, Table B6). It can be seen from Figure 4-10 that Tumour III and IV had the largest percentage deviation of the four tumours underestimating the tumour activity by 34.6 ± 1.2 % and 20.5 ± 1.7 % respectively. This can be attributed to the PVE as the diameter of the two tumours was near the spatial resolution limit of the gamma camera.

More accurate quantification was observed for Tumour I and II with average accuracies of -3.1 ± 3.0 % and 7.8 ± 2.1 % respectively. These tumours were less susceptible to PVE in comparison to Tumour III and IV. Their accuracies was in accordance with literature findings obtained in an abdominal phantom study for planar activity quantification of ^{123}I images acquired using a ME collimator (Macey et al., 1999). Accuracies within 10 % were reported in this study for quantification of the liver and spleen with the use of the GM with an ACF for attenuation correction. From the results it is evident that Tumour II to IV underestimated the tumour activity. In contrast, Tumour I overestimated the quantified activity, more so at 0 cm from the liver, for reasons stated in Chapter 3, Section 3.3.3.6.1.

❖ **Varying tumour-liver distance.**

It can be seen from Figure 4-10, that there is a slight overestimation of activity at 0 cm for Tumour I to IV. This overestimation can be attributed to the liver overlying the tumours at 0 cm distance resulting in the inclusion of primary counts and small angle scatter counts from the liver in the tumour ROI definition (Figure 4-6). The average underestimation, calculated as the difference between the accuracy obtained at tumour-liver distances of 0 cm and 6 cm, for Tumour I to IV was 5.2 %, 3.9 %, 3.1 % and 2.3 % respectively. The underestimation seen for Tumour I was due to the fact that the ROI for Tumour I overlay a larger area of the liver and thus included more counts from the liver.

Contribution of large angle scatter from the liver and internal scatter from the tumours was expected to have a lesser influence as it was compensated for by using the TEW scatter correction technique. The tumour accuracy trend stabilized at distances 3 cm and 6 cm for Tumour I to IV with difference of ≤ 0.6 %.

4.3.3.6.2 Quantification with compensation for partial volume effects.

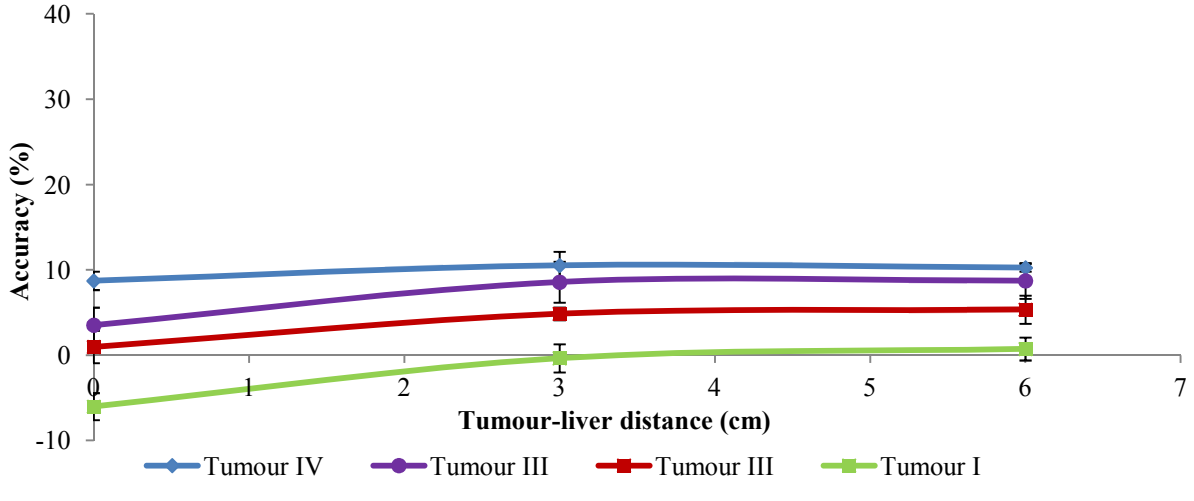

Figure 4-11: *^{123}I activity quantification accuracy for Tumour I to IV with compensation for partial volume effects.*

❖ **Varying tumour sizes.**

Results obtained using larger ROIs to compensate for PVE are shown in Figure 4-11 (See Appendix B, Table B7). The quantification accuracy for all the tumours was better than 12.4 %. The largest percentage deviation of tumour quantification accuracy was 12.4 % and 10.9 % for Tumour I and II respectively following trends observed in Figure 4-10.

❖ **Varying tumour-liver distance.**

The average underestimation, calculated as the difference between the accuracy obtained at tumour-liver distances of 0 cm and 6 cm, for Tumour I to IV was 6.8 %, 4.4 %, 5.2 % and 1.5 % respectively. The underestimation observed for Tumour I can be attributed to the larger ROI used to define Tumour I which included more counts from the liver. There was ≤ 1.1% difference between the accuracies obtained at tumour-liver distances of 3 cm and 6 cm for Tumour I to IV.

4.4 Conclusion.

Tumour activity quantification accuracy was made with reference to activity measurements using the dose calibrator. The accuracy of the dose calibrator for the radionuclide ^{123}I underestimated the activity measured from NMISA by 5.2 %. This underestimation of the accuracy of the dose calibrator for ^{123}I was incorporated into the quantification process, and thus did not affect the accuracy with which quantification could be achieved in this study. The stability of this accuracy was ascertained by the reproducibility test where on average activity measurements for ^{123}I were found to be 22.4 ± 0.19 MBq for different days of measurements. The small variations shown in these measurements indicated the dose calibrator used for this study could be used with confidence for quantification purposes.

Acquisitions were performed using default clinical settings as specified by the manufacturer for ^{123}I. However collimator choice was at the user's discretion. [^{123}I]-MIBG planar clinical images acquired with the Symbia T SPECT/CT with the ME collimator demonstrated improved contrast in comparison to those acquired with the LEHR collimator. This illustrated the potential for improved delineation of organs for quantification purposes. The ME collimator was found to be the better choice for imaging with ^{123}I, as is suggested by literature finding (Bolmsjö et al., 1977; DeNardo et al., 1985; Macey et al., 1986).

The effects of noise from acquired images, room background and count rate losses did not influence quantification accuracy due to their negligible contributions (< 1%). Scatter counts in the photopeak were estimated and corrected by using the TEW scatter correction technique. It was found, from scatter fraction calculations, that the scatter counts from the tumours increased with increasing tumour size and decreased distance from the liver.

There was an increase in the GM of scatter corrected counts found at the tumour-liver distance of 0 cm (where the tumour was in contact with the liver). This was attributed to the inclusion of primary counts as well as small angle scatter counts from the liver included in the ROI used to define the tumour counts. A small difference was observed at tumour-liver distances of 3 cm and 6 cm. This indicated that large angle scatter from the liver had minimal effect on the counts in the tumours at distances of 3 cm and 6 cm from the liver.

Planar attenuation correction was performed by applying an ACF measured using an uncollimated ^{99m}Tc printed transmission source, due to the unavailability of ^{123}I for this purpose. Several scaling factors were applied to account for the following: energy differences between the emission (^{123}I) and transmission (^{99m}Tc) isotopes, differences in linear attenuation coefficient values found between NIST and our clinic, as well as narrow beam and broad beam geometries. These scaling factors were also introduced for Perspex and applied to the SCF. The application of these scaling factors, for attenuation correction of the tumour and SCF data (as indicated in Equation 4.1), resulted in their contribution on the final result of the quantification accuracy being smaller than 2 %.

Planar quantification accuracies of -3.3 ± 3.0 % and 7.8 ± 2.1 % were found for Tumour I and II respectively. However, the quantified activity for the smaller tumours resulted in poorer accuracies, with average underestimations of 20.5 ± 1.7 % and 34.6 ± 1.2 %, for Tumour III and IV respectively. This was a result of the PVE for the smaller tumours whose sizes were near the resolution limit of the gamma camera, taking into consideration that ROIs were drawn according to the physical dimensions of the tumours. Comparable accuracies (difference ≤ 1.2 %) were found for distances of 3 cm and 6 cm from the liver for Tumours I to IV.

PVE compensation using larger ROI definition for the SCF and tumour data resulted in quantification accuracies smaller than 12.4 %. The results suggest that quantification accuracies of < 12.0 % for planar images obtained using ^{123}I quantification for various imaging geometries may be achieved using standard acquisitions and processing techniques when effects of PVE are compensated for. The effects of scatter contribution from the liver on quantification accuracy had minimal impact at distances ≥ 3 cm from the liver, where comparable accuracies (difference ≤ 1.8 %) were found for Tumours I to IV.

A summary of the effects of tumour size, tumour–liver distance, as well as the influence of background activity contribution on quantification accuracy, is presented for both ^{99m}Tc and ^{123}I, and is discussed in Chapter 5.

References

Bolmsjö, M.S., Persson, B.R., Strand, S.E., 1977. Imaging ^{123}I with a scintillation camera. A study of detection performance and quality factor concepts. Phys. Med. Biol. 22, 266–277.

Brown, S., Bailey, D.L., Willowson, K., Baldock, C., 2008. Investigation of the relationship between linear attenuation coefficients and CT Hounsfield units using radionuclides for SPECT. Appl. Radiat. Isot. 66, 1206–1212.

Cherry S.R., Sorenson J.A., Phelps M.E., 2003. SINGLE PHOTON EMISSION COMPUTED TOMOGRAPGY. In: "*Physics in Nuclear Medicine*". 3rd edition, Saunders, USA. pp299–324.

Darcourt, J., Booij, J., Tatsch, K., Varrone, A., Vander Borght, T., Kapucu, O.L., Någren, K., Nobili, F., Walker, Z., Van Laere, K., 2010. EANM procedure guidelines for brain neurotransmission SPECT using (123)I-labelled dopamine transporter ligands, version 2. Eur. J. Nucl. Med. Mol. Imaging 37, 443–450.

DeNardo, G.L., Raventos, A., Hines, H.H., Scheibe, P.O., Macey, D.J., Hays, M.T., DeNardo, S.J., 1985. Requirements for a treatment planning system for radioimmunotherapy. Int. J. Radiat. Oncol. Biol. Phys. 11, 335–348.

Du, Y., Tsui, B.M.W., Frey, E.C., 2006. Model-based compensation for quantitative ^{123}I brain SPECT imaging. Phys. Med. Biol. 51, 1269–1282.

Hubbell, J. H., Seltzer S. M., 2004. Tables of X-ray Mass Attenuation Coefficients and Mass Energy-Absorption Coefficients from 1 keV to 20 MeV for elements Z = 1 to 92 and 48 Additional substances of Dosimetric Interest. National Institute of Standards and Technology, Gaithersburg, MD (Available at <: http://www.nist.gov/pml/data/xraycoef/ > (accessed 17.09.13).

Kojima, A., Matsumoto, M., Takahashi, M., 1991. Experimental analysis of scattered photons in Tc-99m imaging with a gamma camera. Ann. Nucl. Med. 5, 139–144.

Macey, D.J., DeNardo, G.L., DeNardo, S.J., 1999. Planar gamma camera quantitation of ^{123}I, ^{99m}Tc or ^{111}In in the liver and spleen of an abdominal phantom. Cancer Biother. Radiopharm. 14, 299–306.

Macey, D.J., DeNardo, G.L., DeNardo, S.J., Hines, H.H., 1986. Comparison of low- and medium-energy collimators for SPECT imaging with iodine-123-labeled antibodies. J. Nucl. Med. 27, 1467–1474.

Minarik, D., Sjögreen, K., Ljungberg, M., 2005. A new method to obtain transmission images for planar whole-body activity quantification. Cancer Biother. Radiopharm. 20, 72–76.

Ogawa, K., Harata, Y., Ichihara, T., Kubo, A., Hashimoto, S., 1991. A practical method for position-dependent Compton-scatter correction in single photon emission CT. IEEE Trans. Med. Imaging 10, 408–412.

Rubello, D., Bui, C., Casara, D., Gross, M.D., Fig, L.M., Shapiro, B., 2002. Functional scintigraphy of the adrenal gland. Eur. J. Endocrinol. 147, 13–28.

Sgouros, G., Squeri, S., Ballangrud, A.M., Kolbert, K.S., Teitcher, J.B., Panageas, K.S., Finn, R.D., Divgi, C.R., Larson, S.M., Zelenetz, A.D., 2003. Patient-specific, 3-dimensional dosimetry in non-Hodgkin's lymphoma patients treated with 131I-anti-B1 antibody: assessment of tumor dose-response. J. Nucl. Med. 44, 260–268.

Snay, E.R., Treves, S.T., Fahey, F.H., 2011. Improved Quality of Pediatric ^{123}I-MIBG Images with Medium-Energy Collimators. J. Nucl. Med. Technol. 39, 100–104.

Vik, T.A., Pfluger, T., Kadota, R., Castel, V., Tulchinsky, M., Farto, J.C.A., Heiba, S., Serafini, A., Tumeh, S., Khutoryansky, N., Jacobson, A.F., 2009. (123)I-mIBG

scintigraphy in patients with known or suspected neuroblastoma: Results from a prospective multicenter trial. Pediatr. Blood Cancer 52, 784–790.

Zaidi, H., Koral, KF., 2005. METHODS FOR PLANAR IMAGE QUANTIFICATION. In: "*Quantitative analysis in nuclear medicine imaging"*. New York: Kluwer Academic/Plenum Publishers, USA. pp 414–431.

5. CONCLUSION

5.1 Planar image quantification of ^{99m}Tc and ^{123}I.

Planar quantification of nuclear medicine images offers advantages which include, improved image quality and quantitative accuracy. Quantification accuracy is important for its direct application in internal radionuclide dose calculations. Due to physical degradation factors inherent in nuclear medicine imaging, quantitative data is not readily available in routine clinical practice. This emphasizes the need to implement corrections for these degradation factors in an attempt to obtain accurate quantitative information.

Numerous factors affect the accuracy of quantification, and different methods with variable accuracies have been reported. Therefore, it was important to determine the accuracy of planar activity quantification in our clinic using routine clinical protocols. The need for planar activity quantification was motivated by the number of routine imaging studies of neuroendocrine tumours, in our clinic, using [^{123}I]-MIBG prior to therapeutic treatment with [^{131}I]-MIBG. These tumours generally present themselves in the abdomen in various locations in the vicinity of the liver. Therefore, the aim of this study was to evaluate the effect of tumour geometry on the quantification accuracy of ^{99m}Tc and ^{123}I in planar phantom images, by applying scatter and attenuation corrections, with the focus on neuroendocrine tumours. The tumour geometry investigated included: various tumour sizes, various tumour-liver distances and two tumour-background ratios (0.5 % and 1.0 %). This was achieved using an in-house manufactured abdominal phantom facilitated for the clinical geometries under investigation. The phantom was equipped with cylindrical inserts simulating tumours and a Perspex slider used to vary the tumour-liver distance.

The technique applied during the quantification process determined the accuracy with which activity quantification could be achieved. The practicality of the technique is important for routine clinical application. The effectiveness of the technique is determined by its robustness in its application in a range of clinical investigations with varying imaging geometry. For practical reasons, the technique for planar activity quantification was established using ^{99m}Tc. This technique was then applied to the ^{123}I tumour quantification data with the necessary modifications to account for differences between the two radionuclides.

The most prominent degradation factors inherent in nuclear medicine are scatter and attenuation. It seemed imperative that these corrections be included in the quantification

process. Unlike SPECT imaging, where most commercial systems offer the option to automatically correct for the effects of attenuation and scatter, this is not the case for planar imaging. Comparative assessment of the results obtained with the two radionuclides demonstrated the consistency of the planar processing technique. Acquisition protocols used were as specified by the manufacturer. The planar processing technique incorporated the use of the geometric mean method with corrections for scatter and attenuation that could be applied for quantification of [^{123}I]-MIBG studies. The activity measured in the dose calibrators served as a reference for determining the accuracy of the quantification.

The planar processing technique was performed on tumour images to obtain counts from the ROIs defined according to the physical dimensions of the tumours. This method offered a standard, reproducible criterion for the ROI definitions. ROI selection in this manner demonstrated an underestimation of the quantified tumour activity especially for tumour sizes near the gamma camera's resolution limit. This underestimation of the tumour activity can be attributed to spill-out of image counts resulting from the partial volume effect (PVE). PVE compensation, using ROI definition to include the majority of the tumour image counts avoiding overlap with the adjacent activity in the liver, proved to be a very practical method. ROI definition in this manner is commonly used clinically by physicians for organ delineation for relative quantification proposes.

5.2 Scatter correction.

In this study scatter correction was performed using the Siemens modified triple energy window scatter correction technique (higher scatter sub-window set to zero) for ^{99m}Tc and the triple energy window scatter correction technique (uses a lower and a higher scatter sub-window) for ^{123}I, in accordance with the manufacturer specifications (Syngo MI Applications 2007A; Siemens Healthcare). Scatter fractions were determined for the two radionuclides to demonstrate the scatter contribution in the photopeak as estimated by these two scatter corrections techniques. The scatter fractions, expressed as a percentage, obtained for the ^{123}I data were slightly higher than those for ^{99m}Tc. The difference (expressed in percentage), calculated from the average scatter fractions, obtained between the two radionuclides for the largest tumour (Tumour I) to the smallest tumour (Tumour IV) were 7.2 ± 0.3 %, 6.3 ± 0.6 %, 5.0 ± 0.3 % and 5.8 ± 1.1 % respectively. These results indicated that scatter contribution into the photopeak was of the order of 6.0 % higher for ^{123}I tumour data in comparison to the ^{99m}Tc tumour data. This can be attributed to the septal penetration from the higher energy

emissions of ^{123}I, resulting in more scattered events into the photopeak window, which is not encountered with ^{99m}Tc. This, smaller than expected difference between the datasets for ^{99m}Tc and ^{123}I in comparison to literature findings (Chapter 4, Section 4.2.2), can be attributed to the use, in this study, of a medium energy collimator, for imaging with ^{123}I. The use of a medium energy collimator, for imaging with ^{123}I, would reduce the number of detected scattered events, arising from septal penetration, into the photopeak. The scatter contribution in the photopeak was observed to increase with increasing tumour size for both radionuclides. Differences in the scatter contribution of 7.9 % and 9.3 % were observed between the smallest and largest tumours for ^{99m}Tc and ^{123}I respectively. These results illustrated that the two scatter correction techniques were comparable in their estimation of the scatter contribution from ^{99m}Tc and ^{123}I between the smallest and the largest tumour. The study showed that for both radionuclides, the scatter contribution from the liver decreased with increasing tumour-liver distance.

5.3 Attenuation correction.

The use of a ^{99m}Tc transmission source printed with a digital inkjet printer proved to be a practical and cost efficient method to obtain transmission data for planar attenuation correction. Attenuation correction was performed by applying an attenuation correction factor (ACF) to scatter corrected emission data. Scatter contribution from the transmission source was limited by setting the detector transmission source distance to 73 cm. The ACF was approximately equivalent to a factor ten for both isotopes, emphasizing the importance of applying attenuation correction. The ACF was comparable for all tumour sizes and stayed constant for varying tumour-liver distances. These comparable ACFs for all tumour sizes can be attributed to the similar average phantom thickness traversed by all the tumours. Scaling factors were introduced to scale the ACF data to narrow beam geometry taking into account the GM was obtained from scatter corrected data. In the case of quantification of ^{123}I tumour data, a scaling factor was introduced to scale the ACF to account for the energy difference between the emission (^{123}I) and transmission data (^{99m}Tc).

5.4 System calibration factor.

A system calibration factor, processed in the same manner as the tumour quantified data, was used to convert the image counts to units of radioactivity. It incorporated the use of a printed radioactive disk placed in between slabs of Perspex. The SCF obtained for ^{99m}Tc and ^{123}I

were found to be comparable. This can be attributed to a similar imaging geometry and the application of attenuation and scatter corrections in the calculation of the SCF. The processing of the SCF, similar to the tumour quantified data, may have incorporated some bias built into the final quantification accuracy. The SCF was quantified with a radioactive disk which had a large size, and this thus may have favoured better accuracy for the larger tumour sizes.

5.5 Effect of tumour geometry on activity quantification accuracy.

Poor quantification accuracy was observed for the smaller tumours which improved with increasing tumour size for both ^{99m}Tc and ^{123}I. The poorest (the largest percentage deviation in quantification accuracy) was obtained for the smallest tumours with average activity underestimations of 29.2 ± 1.3 % and 34.6 ±1.2 % for ^{99m}Tc and ^{123}I respectively. These large underestimations observed for the smallest tumours were attributed to PVE, which diminished with increasing tumour sizes. The best quantification accuracy was observed for the largest tumour with overestimations of -3.3 ± 2.6 % and -3.1 ± 3.0 % for ^{99m}Tc and ^{123}I respectively. The small overestimation of the activity in this tumour was attributed to its large size (212 ml) in comparison to tumour inserts used in the literature (Chapter 3, Section 3.3.3.6.1(a)). The average percentage differences (for the three tumour-liver distances) found between ^{99m}Tc and ^{123}I were 0.2 %, 2.1 %, 5.8 % and 5.4 % for the largest to the smallest tumours respectively. There was a slight overestimation of tumour activity at 0 cm from the liver, a trend that was observed for both radionuclides. Maximum overestimation, calculated as the difference between the accuracies obtained at 0 cm and 6 cm, was observed for the largest tumour with a difference of 5.2 % for both radionuclides. This was attributed to the fact that the largest tumour overlay a larger area of the liver at 0 cm and thus included more counts from the liver. Tumour-liver distances greater than 3 cm from the liver had minimal effect on the quantification accuracy. The difference between the average quantification accuracies, calculated at 3 cm and 6 cm from the liver, was ≤ 0.6 % for both radionuclides except, for Tumour I filled with ^{99m}Tc (1.7 % difference) and Tumour III filled with ^{123}I (-1.2 % difference).

Similar trends, as described above, were observed for compensation of PVE. PVE compensation resulted in improved quantification accuracy for all tumour sizes yielding accuracies between 9.1 % and -7.4 % for ^{99m}Tc, and 12.4 % and -6.0 % for ^{123}I. Overestimation of activity quantification for the tumours was still observed at a tumour-liver

distance of 0 cm. A maximum difference between the tumour quantification accuracy at distances of 0 cm and 6 cm was obtained for Tumour III (5.5 % and 5.2 % for ^{99m}Tc and ^{123}I respectively). This difference was attributed to the shape of Tumour III which overlay a large area of the liver at 0 cm. The tumour quantification accuracy stabilized at a distance of 3 cm from the liver. The maximum differences between the tumour quantification accuracies, calculated between the tumour-liver distance of 0 cm and 3 cm, were comparable for the two radionuclides 1.8 % vs. -1.1 % for ^{99m}Tc and ^{123}I respectively.

Background contribution to tumour quantification accuracy, investigated with ^{99m}Tc using Tumour II, resulted in a maximum of 16.6 % contribution for calculations without PVE compensation for the higher (1 %) tumour-background ratio. This contribution was increased to 26.3 % on compensation for PVE, using larger ROI definitions.

Literature studies have reported various planar quantification accuracies obtained with different quantification techniques. It is important for each clinic to establish its own quantification technique. This quantification technique must be optimised taking into consideration the vast range of tumour geometries observed in clinical studies. This study has demonstrated a method which can be used for accurate quantification of planar studies. The method incorporates corrections for scatter, attenuation as well as PVE compensation. These corrections have proven to be very important for quantification accuracy for both ^{99m}Tc and ^{123}I. Consistent trends were observed for both ^{99m}Tc and ^{123}I for varying tumour sizes and varying tumour-liver distances. Results from this study showed that attenuation would result in large underestimations of the tumour activity if not corrected for. The attenuation effect was aggravated by the large circular shape (diameter = 31 cm) of the PVC phantom used in this study. This is in contrast to the smaller circular and oval shape phantoms used in most studies to simulate the abdomen. The use of an uncollimated printed transmission source has proven to be an effective, practical and cost efficient manner by which to obtain transmission data. Increasing the transmission source distance has been shown to be an efficient method to limit the scatter in the transmission source image to the extent that it approximates a collimated source geometry. The influence of background contribution, on the accuracy of tumour quantification accuracy, increased with increasing tumour-background ratio.

It has been shown in this study that PVE has a large impact (36.7 %) on the quantification accuracy of smaller tumours, with physical size near the resolution limit of the gamma

camera, while improved accuracy (-7.0 %) was observed for the larger tumours. Planar activity quantification accuracies of better than 12.4 % and 9.1% were achieved for ^{123}I and ^{99m}Tc respectively when corrections for scatter, attenuation and PVE were incorporated into the quantification process, without significant background activity (1 %). Background activity had a maximum contribution of 26.3 % on tumour quantification accuracy. It was demonstrated in this study that the scatter contribution to the tumours from the liver had minimal effect on the quantification accuracy at tumour-liver distances larger than 3 cm.

5.6 Recommendations.

The results obtained from this study indicate that this technique can be successfully implemented in activity quantification of [^{123}I]-MIBG. However this study has also raised some questions for future considerations, and are discussed below.

The TEW scatter correction technique in this study may be further optimised by investigating the influence of the weighting factor and energy window widths on scatter estimates. Also, the accuracy of the scatter estimates may be verified by Monte Carlo simulations.

Simultaneous acquisitions of emission-transmission images can be successfully implemented for future work with ^{131}I quantification using a ^{99m}Tc printed transmission source. The emission-transmission studies can be acquired in separate energy windows with necessary corrections to account for the energy difference between them. Simultaneous ^{123}I emission and ^{99m}Tc transmission imaging may result in practical challenges. Simultaneous acquisition with these radionuclides may result in the contamination of the transmission data with down-scatter from the emission data, resulting in erroneous results for attenuation correction. Another important consideration in this study was the count density difference between the emission and transmission data. In this research project activity of 370 MBq was evenly distributed over an A3 size transmission source. The count density of the tumours was much higher in comparison to the count density of the printed transmission source, which may result in larger error propagation and inconsistent ACF results. Scatter from the uncollimated transmission source was limited by increasing the transmission source to detector distance to 73 cm. This transmission source to detector distance is limited by the gantry configuration of the gamma camera and may differ for other systems. It is recommended that an investigation should follow to evaluate the use of a smaller printed transmission source, large enough to cover only the area under investigation. The transmission source radioactivity is then

distributed only over the area of interest resulting in increased count density. Consideration can also be given to using a non-uniform transmission source to increase count density in the high attenuation regions. The required count ratio, between transmission and emission data, needed to obtain reliable results for attenuation correction when using simultaneous emission-transmission imaging, should also be investigated.

There is no standard method used for ROI definition for objects of interest for quantification purposes. Edge detection is a separate research topic influenced by factors such as counts statistics, organ overlap and background activity. These variables influence the effectiveness of most automatic edge detection methods, which seem to fall short in taking these factors into consideration. This study has demonstrated the importance of recovering the count distribution from the object of interest, especially for small objects susceptible to PVE. The use of a larger ROI to compensate for PVE was demonstrated to be a reliable and practical method. The use of recovery coefficients to correct for PVE, offers practical challenge as these cannot be generated for the vast range of tumour shapes. Background activity has been shown to have a large effect on the tumour quantification accuracy due to the superimposed activity in the tumour projection. Background correction should incorporate an effective thickness to take into account changing object thickness, and as a result, differences in attenuation. Background correction should take organ thickness into consideration and an efficient reliable method should be investigated and implemented.

This research project has demonstrated successful implementation of a practical technique to obtain planar quantitative information. This was important in the attempt to obtain improved quantification accuracy, in comparison to relative planar quantification techniques. SPECT quantification has overcome some of the problems encountered with planar image quantification. However, planar image quantification continues to play an important role in the quantification of whole body images which provide a full assessment of the bio-distribution and thus radiation dosimetry following radionuclide administrations.

Summary

Accurate activity quantification is important for its application in radiation dosimetry. Planar image quantification plays an important role in the quantification of whole body images which provide a full assessment of bio-distribution from radionuclide administrations. In the Department of Nuclear Medicine at Universitas Hospital, ^{123}I meta-iodobenzylguanidine [^{123}I]-MIBG quantification of neuroendocrine tumours is performed prior to therapeutic radionuclide treatment. The bio-distribution of activity in these studies is mostly in the abdominal region. Factors influencing quantification include scatter, attenuation, background activity and close proximity of organs with radioactivity uptake. The aim of this study was to evaluate the effect of tumour geometry on the quantification accuracy of ^{99m}Tc and ^{123}I in planar phantom images, by applying scatter and attenuation corrections, with the focus on neuroendocrine tumours. The tumour geometry investigated included: various tumour sizes, various tumour-liver distances and two tumour-background ratios (0.5 % and 1.0 %).

The quantification technique was first developed with the readily available ^{99m}Tc and subsequently applied to the more costly ^{123}I used for imaging neuroendocrine tumours. Adjustments were necessary due to the difference in physical properties between the two isotopes. An in-house manufactured abdominal phantom was developed to mimic the clinical geometries under investigation. The phantom was equipped with cylindrical inserts used to simulate tumours (diameters of the tumours were 63 mm, 45 mm, 34 mm and 23 mm) and a slider to vary the tumour-liver distance.

The processing technique incorporated the use of the geometric mean method with corrections for scatter and attenuation performed on image counts. Scatter correction was performed using a modified triple energy window scatter correction technique for ^{99m}Tc and ^{123}I, according to gamma camera manufacturer specifications. Attenuation correction was performed using transmission images obtained with an uncollimated ^{99m}Tc printed source. Scatter contribution from the abdominal phantom and transmission source combination was limited by setting the detector transmission source distance to 73 cm. A system calibration factor, processed in the same manner as the tumour quantified data was used to convert the image counts to units of radioactivity. Partial volume effect (PVE), was compensated for by the manner in which regions for tumour activity distribution were defined. The activity

measured in the dose calibrators served as a reference for determining the accuracy of the quantification.

The largest percentage deviation was obtained for the smallest tumours. The average activity underestimations were 29.2 ± 1.3 % and 34.6 ±1.2 % for ^{99m}Tc and ^{123}I respectively. These large underestimations observed for the smallest tumours were attributed to PVE, which diminished with increasing tumour sizes. Better quantification accuracy was observed for the largest tumour with overestimations of 3.3 ± 2.6 % and 3.1 ± 3.0 % for ^{99m}Tc and ^{123}I respectively. PVE compensation resulted in improved quantification accuracy for all tumour sizes yielding accuracies of better than 9.1 % and 12.4 % for ^{99m}Tc and ^{123}I respectively. Scatter contribution to the tumours from the liver had minimal effect on the quantification accuracy at tumour-liver distances larger than 3 cm. An increased tumour-background ratio resulted in an increase in the quantification results of up to 16.6 % for calculations without PVE compensation. This contribution was increased to 26.3 % when PVE were compensated for, using larger regions.

The literature often report accurate planar quantification results, however, this study shows that it is important to consider the specific tumour geometry for the study. It remains the responsibility of the user to evaluate the clinical available software and implement it in a responsible manner. When applying all relevant corrections for scatter, attenuation and PVE without significant background, quantification accuracy within 12 % was obtained. This study has demonstrated successful implementation of a practical technique to obtain planar quantitative information.

Key words

1. *Radioactivity quantification*
2. *Planar*
3. *Accuracy*
4. *Geometry*
5. *Attenuation*
6. *Scatter*
7. *Triple energy window*
8. *Tumour size*
9. *Tumour distance*

10. Background activity

Opsomming

Akkurate kwantifisering van aktiwiteit is belangrik vir gebruik in stralingsdosimetrie. Planare beeld kwantifisering speel 'n belangrike rol in die kwantifisering van heelliggaam beelde, wat 'n volledige beoordeling van die bio-verspreiding van die radionuklied verspreiding moontlik maak. In die Departement Kerngeneeskunde by Universitas Hospitaal, word ^{123}I meta-iodobenzylguanidine [^{123}I]-MIBG kwantifisering van neuro-endokriene tumors uitgevoer alvorens radioaktiewe terapeutiese dosisse toegedien word. Die bio-verspreiding van aktiwiteit in hierdie studies kom meestal in die abdominale gebied voor. Faktore wat die kwantifisering beïnvloed sluit onder andere verstrooiing, attenuasie, agtergrondaktiwiteit en naby geleë organe met radioaktiwiteit opname in. Die doel van die studie was om die effek van geometrie op die akkuraatheid van kwantifisering van ^{99m}Tc en ^{123}I planare fantoom beelde te evalueer, deur die toepassing van verstrooiing en attenuasie korreksies, met die geometrie soos aangetref by neuro-endokriene tumore. Die tumor geometrie wat ondersoek is, sluit verskeie tumor groottes, verskeie tumor-lewer afstande en twee verskillende tumor-agtergrond verhoudings (0.5 % en 1.0 %) in.

Die kwantifiseringstegniek was aanvanklik ontwikkel vir ^{99m}Tc wat geredelik beskikbaar is en is later aangepas vir die duurder ^{123}I wat gebruik word vir neuroendokriene tumor beelding. Aanpassings was nodig as gevolg van die verskillende fisiese eienskappe van die twee nukliedes. 'n Abdominale fantoom was in-huis ontwikkel en vervaardig om die kliniese tumor geometrie wat ondersoek is, na te boots. Die fantoom het silindriese insetsels gehad om tumors te simuleer (deursnee van die tumore was 63 mm, 45 mm, 34 mm en 23 mm) asook 'n skuifstaaf om die tumor-lewer afstand te varieer.

Die verwerkingstegniek maak gebruik van die geometriese gemiddelde metode met verstrooiings- en attenuasiekorreksies wat op die tellings in die beelde uitgevoer word. Die verstrooiingskorreksie was uitgevoer deur gebruik te maak van 'n aangepaste drievenster-verstrooiingskorreksie-tegniek vir ^{99m}Tc en ^{123}I, volgens die gamma kamera vervaardiger se spesifikasies. Attenuasie korreksie was uitgevoer deur gebruik te maak van transmissie beelde wat verkry is met 'n ongekollimeerde gedrukte ^{99m}Tc bron. Die verstrooiingsbydrae van die fantoom transmissiebron kombinasie was beperk deur 'n detektor transmissiebron afstand van 73cm te gebruik. 'n Stelsel kalibrasiefaktor, waarvan die data soortgelyk aan die tumor kwantifiseringsdata verwerk is, is gebruik om die beeldtellings om te skakel na

aktiwiteit. Die parsiele volume effek (PVE) is in ag geneem deur die manier waarop die gebiede van die tumor aktiwiteitverpreiding is. Tumor-aktiwiteit kwantifiseringsakkuraatheid (%) is bepaal met verwysing na aktiwiteitmetings in die bronkalinreerder.

Die grootste persentasie afwyking in aktiwiteitopname het voorgekom in die kleinste tumore. Die gemiddelde aktiwiteitsonderskattings was 29.2 ± 1.3 % en 34.6 ± 1.2 % vir ^{99m}Tc en ^{123}I respektiewelik. Hierdie groot onderskattings wat waargeneem is by die kleinste tumore word toegeskryf aan die PVE wat onbeduidend raak met toename in tumorgrootte. Die grootste tumor het 'n beter kwantifiseringsakkuraatheid getoon, met oorskattings van 3.3 ± 2.6 % en 3.1 ± 3.0 % vir ^{99m}Tc en ^{123}I onderskeidelik. Kompensasie vir PVE het gelei tot verbeterde kwantifiseringsakkuraatheid vir alle grootte tumore, met akkuraathede beter as 9.1% en 12.4 % vir ^{99m}Tc en ^{123}I respektiewelik. Die verstrooiingsbydrae wat die lewer-aktiwiteit op die kwantifisering van die tumor gehad het, was minimaal vir tumor-lewer afstande van 3cm en meer. 'n Toename in die tumor-agtergrond verhouding het gelei tot 'n toename in die kwantifiseringsresultate tot 16.6 % vir berekenings sonder PVE kompensasie. Hierdie bydrae het vergroot tot 26.3 % wanneer PVE kompensasie deur middel van groter gebiede van belang toegepas is.

In die literatuur word akkurate planare kwantifiseringsresultate dikwels vermeld, maar hierdie studie toon dat die spesifieke tumor geometrie altyd in ag geneem moet word. Dit bly verder die verantwoordelikheid van die gebruiker om die kliniese beskikbare sagteware te evalueer en op 'n verantwoordelike wyse te implementeer. Indien alle relevante korreksies vir verstrooiing, attenuasie en PVE aangebring word, sonder betekenisvolle agtergrondsbydrae, was 'n akkuraatheid van beter as 12 % verkry. Hierdie studie toon die suksesvolle implementering van 'n praktiese tegniek om planare kwantifiserings inligting te verky.

Kernwoorde

1. *Radioaktiwiteit kwantifisering*
2. *Planaar*
3. *Akkuraatheid*
4. *Geometrie*
5. *Attenuasie*
6. *Verstrooiing*

7. *Drie-energie-venster*
8. *Tumor grootte*
9. *Tumor afstand*
10. *Agtergrond aktiwiteit*

APPENDIX A

Activity quantification using technetium-99m for results obtained in Chapter 3.

Table A1-A4: Examples of total counts recorded in the photopeak and scatter sub-window for a single set of acquisition obtained for the different tumour sizes.

Table A5: The average attenuation correction factors for different tumour sizes measured at the various tumour-liver distances of 0 cm, 3 cm and 6 cm.

Table A6: Tumour activity quantification accuracy for Tumour I to IV without compensation for partial volume effects.

Table A7: Tumour activity quantification accuracy for Tumour I to IV with compensation for partial volume effects.

Table A1: *Total counts recorded in the photopeak window and scatter sub-windows for Tumour I (212 ml).*

	Anterior Counts		Posterior Counts	
Tumour-liver distance (cm)	$C_{photopeak}$	$C_{Scatter}$	$C_{photopeak}$	$C_{Scatter}$
0	517552	166301	219355	75235
3	480737	147621	214436	69582
6	468139	136605	209430	65137

Table A2: *Total counts recorded in the photopeak window and scatter sub-windows for Tumour II (80 ml).*

	Anterior Counts		Posterior Counts	
Tumour-liver distance (cm)	$C_{photopeak}$	$C_{Scatter}$	$C_{photopeak}$	$C_{Scatter}$
0	409865	117983	149747	45160
3	388508	105346	147341	42259
6	372086	97134	132659	40672

Table A3: *Total counts recorded in the photopeak window and scatter sub-windows for Tumour III (25 ml).*

	Anterior Counts		Posterior Counts	
Tumour-liver distance (cm)	$C_{photopeak}$	$C_{Scatter}$	$C_{photopeak}$	$C_{Scatter}$
0	203845	43610	67310	16156
3	195189	38632	64628	13992
6	190081	33658	63003	12643

Table A4: *Total counts recorded in the photopeak window and scatter sub-windows for Tumour IV (10 ml)*

	Anterior Counts		**Posterior Counts**	
Tumour-liver distance (cm)	$C_{photopeak}$	$C_{Scatter}$	$C_{photopeak}$	$C_{Scatter}$
0	106901	22750	34333	8798
3	101867	19536	33651	7512
6	97920	17168	33187	6782

Table A5: *Average attenuation correction factors (ACFs) measured at the various tumour-liver distances for the different tumour sizes.*

Week number	**$ACF_{Tumour\ I}$**	**$ACF_{Tumour\ II}$**	**$ACF_{Tumour\ III}$**	**$ACF_{Tumour\ IV}$**
1	9.80 ± 0.02	10.09 ± 0.03	10.43 ± 0.17	10.36 ± 0.14
2	9.93 ± 0.01	10.21 ± 0.02	10.30 ± 0.05	10.22 ± 0.08
3	9.75 ± 0.02	10.08 ± 0.04	10.42 ± 0.02	10.28 ± 0.18
4	9.85 ± 0.04	10.13 ± 0.02	10.47 ± 0.09	10.43 ± 0.07
5	9.99 ± 0.05	10.18 ± 0.06	10.34 ± 0.04	10.18 ± 0.06
6	9.74 ± 0.07	10.12 ± 0.04	10.58 ± 0.11	10.35 ± 0.23
7	9.88 ± 0.10	10.07 ± 0.05	10.32 ± 0.07	10.50 ± 0.19
8	9.61 ± 0.05	10.17 ± 0.09	10.55 ± 0.15	10.57 ± 0.07
9	9.79 ± 0.07	10.06 ± 0.04	10.40 ± 0.10	10.80 ± 0.15
10	9.83 ± 0.03	10.20 ± 0.02	10.22 ± 0.12	10.27 ± 0.10
Average	**9.82 ± 0.11**	**10.13 ± 0.05**	**10.40 ± 0.11**	**10.36 ± 0.12**

Table A6: *^{99m}Tc activity quantification accuracy for Tumour I to IV without compensation for partial volume effects*.

Tumour number	Tumour-liver distance (cm)	Tumour activity quantification accuracy (%)			
		Set 1	Set 2	Set 3	Average
Tumour I					
	0	-6.0	-6.3	-6.1	-6.1 ± 0.2
	3	-3.0	-3.6	-1.4	-2.7 ± 1.1
	6	-1.2	-1.0	-0.7	-1.0 ± 0.3
Tumour II					
	0	4.8	3.0	5.6	4.4 ± 1.3
	3	5.2	5.3	8.0	6.2 ± 1.6
	6	5.0	5.4	8.4	6.5 ± 1.6
Tumour III					
	0	13.0	12.2	11.6	12.3 ± 0.7
	3	17.6	15.9	14.0	15.8 ± 1.8
	6	16.9	15.3	15.4	15.9 ± 0.9
Tumour IV					
	0	28.3	26.9	28.0	27.7 ± 0.8
	3	31.4	30.0	29.3	30.2 ± 1.1
	6	30.6	30.0	28.7	29.8 ± 1.0

Table A7: *^{99m}Tc activity quantification accuracy for Tumour I to IV with compensation for partial volume effects.*

Tumour number	Tumour-liver distance (cm)	Tumour activity quantification accuracy (%)			
		Set 1	Set 2	Set 3	Average
Tumour I					
	0	-6.6	-8.2	-7.4	-7.4 ± 0.8
	3	-3.6	-4.2	-2.7	-3.5 ± 0.8
	6	-1.8	-1.5	-1.9	-1.7 ± 0.2
Tumour II					
	0	-4.1	-5.4	-0.7	-3.4 ± 2.4
	3	-0.4	-1.9	2.3	0.0 ± 2.1
	6	0.8	-1.5	3.2	0.8 ± 2.4
Tumour III					
	0	0.0	-0.6	0.8	0.0 ± 0.7
	3	5.6	5.0	4.7	5.1 ± 0.5
	6	6.1	3.9	6.8	5.6 ± 1.5
Tumour IV					
	0	5.8	4.2	3.7	4.6 ± 1.1
	3	9.2	10.0	8.1	9.1 ± 0.9
	6	8.5	9.1	6.8	8.1 ± 1.2

APPENDIX B

Activity quantification using iodine-123 for results obtained in Chapter 4.

Table B1-B4: Examples of total counts recorded in the photopeak and scatter sub-windows for a single set of acquisition obtained for the different tumour sizes.

Table B5: The average attenuation correction factors for different tumour sizes measured at the various tumour-liver distances of 0 cm, 3 cm and 6 cm.

Table B6: Tumour activity quantification accuracy for Tumour I to IV without compensation for partial volume effects.

Table B7: Tumour activity quantification accuracy for Tumour I to IV with compensation for partial volume effects.

Table B1: *Total counts recorded in the photopeak window as well as the lower and higher scatter sub-windows for Tumour I (212 ml).*

	Anterior Counts			Posterior Counts		
Tumour-liver distance (cm)	$C_{photopeak}$	C_{lower}	C_{higher}	$C_{photopeak}$	C_{lower}	C_{higher}
0	552000	204436	25379	215149	88037	9918
3	513562	179278	24130	206674	80606	9597
6	502992	167096	22001	204805	76023	8891

Table B2: *Total counts recorded in the photopeak window as well as the lower and higher scatter sub-windows for Tumour II (80 ml).*

	Anterior Counts			Posterior Counts		
Tumour-liver distance (cm)	$C_{photopeak}$	C_{lower}	C_{higher}	$C_{photopeak}$	C_{lower}	C_{higher}
0	446289	134520	19458	170483	55248	8537
3	425759	118684	20285	162931	49706	8362
6	414408	108864	18798	161808	46884	7981

Table B3: *Total counts recorded in the photopeak window as well as the lower and higher scatter sub-windows for Tumour III (25 ml).*

	Anterior Counts			Posterior Counts		
Tumour-liver distance (cm)	$C_{photopeak}$	C_{lower}	C_{higher}	$C_{photopeak}$	C_{lower}	C_{higher}
0	193639	54412	6876	78117	23627	2939
3	200819	49005	6752	70447	20084	2567
6	199418	45130	6095	65844	17929	2367

Table B4: *Total counts recorded in the photopeak window as well as the lower and higher scatter sub-windows for Tumour IV (10 ml).*

	Anterior Counts			**Posterior Counts**		
Tumour-liver distance (cm)	$C_{photopeak}$	C_{lower}	C_{higher}	$C_{photopeak}$	C_{lower}	C_{higher}
0	104331	27766	4035	38937	11528	1486
3	104755	24791	3516	35460	10497	1442
6	96718	20016	3144	36023	9481	1269

Table B5: *Average attenuation correction factors (ACFs) measured at the various tumour-liver distances for the different tumour sizes.*

Week number	**$ACF_{Tumour\ I}$**	**$ACF_{Tumour\ II}$**	**$ACF_{Tumour\ III}$**	**$ACF_{TumourIV}$**
1	9.42 ± 0.06	9.84 ± 0.07	10.07 ± 0.08	9.94 ± 0.01
2	9.49 ± 0.02	9.76 ± 0.05	10.01 ± 0.03	9.86 ± 0.06
3	9.61 ± 0.03	9.90 ± 0.05	10.01 ± 0.10	10.03 ± 0.11
Average	**9.51 ± 0.09**	**9.83 ± 0.05**	**10.03 ± 0.07**	**9.95 ± 0.10**

Table B6: *^{123}I activity quantification accuracy for Tumour I to IV without compensation for partial volume effects.*

Tumour number	Tumour-liver distance (cm)	Tumour activity quantification accuracy (%)			
		Set 1	Set 2	Set 3	Average
Tumour I					
	0	-5.8	-6.8	-7.0	-6.5 ± 0.6
	3	-0.3	-2.2	-1.4	-1.3 ± 0.9
	6	0.2	-2.2	-2.0	-1.3 ± 1.3
Tumour II					
	0	5.2	6.4	4.4	5.3 ± 1.0
	3	9.6	8.9	7.6	8.7 ± 1.0
	6	10.2	10.9	6.8	9.3 ± 2.2
Tumour III					
	0	17.8	17.5	20.2	18.5 ± 1.5
	3	19.8	22.3	22.3	21.5 ± 1.5
	6	21.3	21.6	21.1	21.6 ± 0.2
Tumour IV					
	0	30.5	33.0	36.1	33.2 ± 2.8
	3	33.6	34.7	36.9	35.1 ± 1.7
	6	34.4	35.5	36.7	35.5 ± 1.1

Table B7: *^{123}I activity quantification accuracy for Tumour I to IV with compensation for partial volume effects.*

Tumour number	Tumour-liver distance (cm)	Tumour activity quantification accuracy (%)			
		Set 1	Set 2	Set 3	Average
Tumour I					
	0	-7.6	-4.4	-6.0	-6.0 ± 1.6
	3	-2.4	1.1	0.0	-0.4 ± 1.6
	6	1.2	1.8	-0.8	0.7 ± 1.3
Tumour II					
	0	-1.1	2.5	1.6	1.0 ± 1.9
	3	4.0	5.4	5.1	4.9 ± 0.8
	6	4.7	7.2	4.2	5.4 ± 1.7
Tumour III					
	0	3.7	1.4	5.5	3.5 ± 2.1
	3	6.1	8.8	10.9	8.6 ± 2.4
	6	6.4	9.3	10.5	8.7 ± 2.1
Tumour IV					
	0	7.8	8.5	9.9	8.7 ± 1.1
	3	9.5	9.7	12.4	10.5 ± 1.6
	6	9.8	10.4	10.6	10.3 ± 0.5